HEINRICH HEINE
UNIVERSITÄT
DÜSSELDORF

Untersuchung zu Struktur-Funktionsbeziehungen von Membranproteinen mittels Kraftspektroskopie

Inaugural-Dissertation

zur Erlangung des Doktorgrades
der Mathematisch-Naturwissenschaftlichen Fakultät
der Heinrich-Heine-Universität Düsseldorf

vorgelegt von

Leoni Oberbarnscheidt
aus Düsseldorf

Düsseldorf, Mai 2010

aus dem Institut für physikalische Chemie II
der Heinrich-Heine Universität Düsseldorf

Gedruckt mit der Genehmigung der
Mathematisch-Naturwissenschaftlichen Fakultät der
Heinrich-Heine-Universität Düsseldorf

Referent: Dr. Filipp Oesterhelt
Koreferent: Prof. Dr. Lutz Schmitt

Tag der mündlichen Prüfung: 13.7.2010

Inhaltsverzeichnis

Publikationen

Diese Dissertation beruht auf folgenden Publikationen:

L. Oberbarnscheidt , A. Reichel, M. Bhagawati, R. Janissen, J. Piehler, F. Oesterhelt, 2010
Multivalent interactions in flexible interaction pairs increase their affinity but not the mechanical stability
Manuskript in Revision

L. Oberbarnscheidt, R. Janissen, F. Oesterhelt, 2009
Direct and model free calculation of force-dependent dissociation rates from force spectroscopic data
Biophys. J., 97(9), 19-21

L. Oberbarnscheidt, R. Janissen, S. Martell, M. Engelhard, F. Oesterhelt, 2009
Single-molecule force spectroscopy measures structural changes induced by light activation and transducer binding in sensory rhodopsin II
J. Mol. Biol., 394(3), 383-390

R. Janissen, L. Oberbarnscheidt, F. Oesterhelt, 2009
Optimized straight forward procedure for covalent surface immobilization of different biomolecules for single molecule applications
Colloids Surf B Biointerfaces,71(2), 200-207

D.A. Cisneros, L. Oberbarnscheidt, A. Pannier, J.P. Klare, J. Helenius, M. Engelhard, F. Oesterhelt, D.J. Muller, 2008
Transducer binding establishes localized interactions to tune sensory rhodopsin II
Structure, 16(8), 1206-1213

1 Einleitung

Die Nanotechnologie rückt heutzutage immer mehr in das Bewusstsein der Öffentlichkeit. Hierbei stehen sich Vorstellungen aus Science Fiction Romanen, in denen Nanotechnologie intelligente Roboter und implantierte Microchips ermöglicht, Diskussionen gegenüber, die vor der Gefahr von Nanopartikeln als Zusatzstoff in Lebensmitteln warnen. Bei genauerer Betrachtung zeigt sich, dass sich hinter dem relativ neuen, modischen Begriff „Nanotechnologie“ etablierte Forschungsfelder der Biologie, Chemie und Physik verbergen. Mit biochemischen und biophysikalischen Methoden werden mittlere bis große Biomoleküle untersucht, die mit ihrer Größenordnung im Nanometerbereich liegen. Biomoleküle, wie Proteine oder DNA, werden hierbei als biologische Nanomaschinen gesehen, und das Ziel der Nanotechnologie ist es, diese zu verstehen und dann zu instrumentalisieren. Hierbei kann generell zwischen dem bottom-up Ansatz und dem top-down Ansatz unterschieden werden. Bei ersterem werden komplexe Maschinen aus kleinsten Funktionseinheiten nach dem biologischen Prinzip der Selbstorganisation entwickelt, während beim letzteren kleinste nanoskalige Strukturen durch Miniaturisierung geschaffen werden, die ihren Einsatz zum Beispiel zur Effizienzsteigerung in der Mikroelektronik, als smarte Materialien oder als Sonden in der Biomedizin finden.

Die Rasterkraftmikroskopie ist ein wichtiges Werkzeug der Nanotechnologie, da sie sowohl die Untersuchung als auch die gezielte Manipulation einzelner Biomoleküle erlaubt. Sie wurde 1986 aus der Rastertunnelmikroskopie entwickelt (Binning et al., 1986) und ermöglicht es, nicht leitende Proben im Nanometer- und Pikonewtonbereich zu untersuchen. Sie besitzt somit eine Auflösung, die zweihundert- bis dreihundert mal kleiner ist als die Auflösung beugungslimitierter, optischer Methoden. In dieser Arbeit wurde diese physikalische Methode genutzt und weiterentwickelt um Struktur-Funktionsbeziehung und chemische Eigenschaften von biologischen Proben, nämlich den Membranproteinen Sensorhodopsin und dem ABC-Transporter NisT, zu untersuchen. Nachdem die Technik als solche und ihre Anwendung zur Untersuchung von Membranproteinen in Kapitel 1 vorgestellt wird, wird in den weiteren Kapiteln der Hintergrund zu den entsprechenden Publikationen und ihr Platz im Kontext erläutert.

2 Rasterkraftmikroskopie (Atomic Force Microscopy)

2.1 Aufbau eines Rasterkraftmikroskops

Das Prinzip des Rasterkraftmikroskops ist in Abbildung 1A schematisch dargestellt. Um einzelne Moleküle abzubilden wird die Probe mit einer Spitze, deren Ende aus nur wenigen Atomen besteht und die einen Radius von nur wenigen Nanometern besitzt (Abb. 1B, 1C), abgerastert.

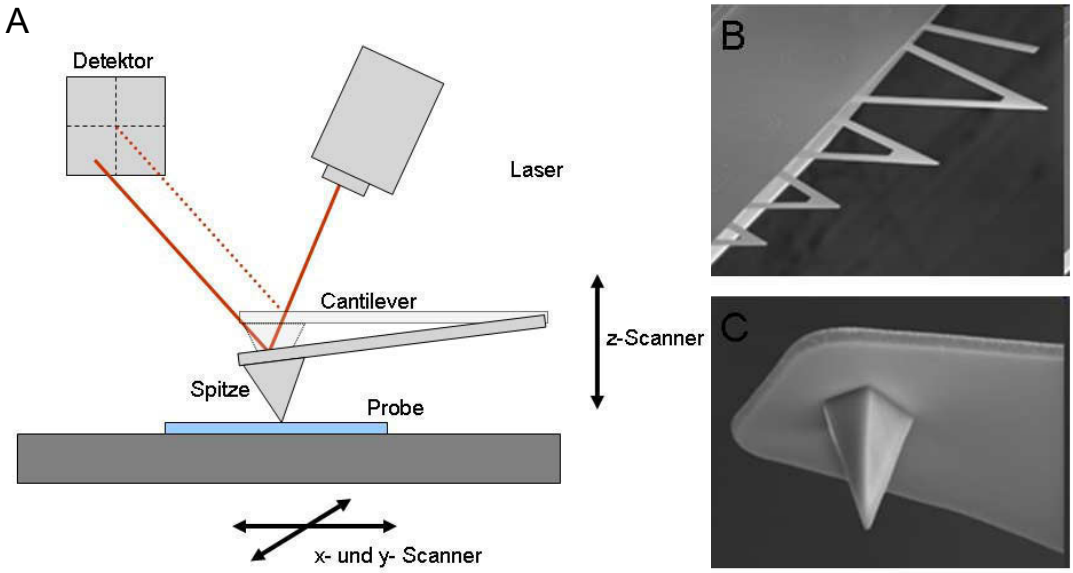

Abbildung 1: Schema des Prinzips eines Rasterkraftmikroskops und elektronenmikroskopische Aufnahme von Spitzen

A: Schema vom Aufbau eines Kraftmikroskops. Der Laserstrahl wird auf die Rückseite einer Blattfeder gelenkt, deren Auslenkung entsprechend den Eigenschaften der Probe ist. Die Auslenkung wird durch die Reflektion des Lasers auf die unterschiedlichen Segmente einer Photodiode bestimmt. **B:** Elektronenmikroskopische Aufnahme von Spitzen, die in dieser Arbeit verwendet wurden. (Bilder entnommen von https://www.veecoprobes.com.)

Mithilfe von Scannern in x- und y-Richtung wird hierzu entweder die Spitze über die Probe gerastert oder die Probe unter der Spitze bewegt, wie es der Fall in der hier vorliegenden Arbeit ist. Die Spitze befindet sich am Ende einer mit Gold beschichteten Blattfeder (Cantilever), deren Bewegung von einem Laser detektiert wird, indem er auf die Rückseite der Blattfeder gelenkt wird, von der er entsprechend des Lichtzeigerprinzips auf eine Photodiode reflektiert wird. Die Photodiode ist in zwei oder vier Segmente unterteilt, so dass die genaue Position des Lasers - und damit auch die Verbiegung des Cantilevers - durch die Differenz der Signale der einzelnen Segmente bestimmt werden kann. Um zu

vermeiden, dass die Kräfte zu groß werden und die Probe zerstören, wird die Verbiegung des Cantilevers möglichst konstant gehalten, indem die Entfernung zwischen Probe und Spitze mit dem z-Scanner nachgeregelt wird. Aus den Daten der Verbiegung des Cantilevers (Deflection) und der Einstellung des z-Scanners können sowohl Oberflächenstruktur und Konsistenz der Probe (beim Abbilden) als auch ihre Stabilität innerhalb ihrer Umgebung (bei Kraftmessungen) bestimmt werden.

2.2 Anwendungen des Rasterkraftmikroskops

2.2.1 Abbilden

Beim Abbilden wird die Oberflächenstruktur der Probe bestimmt, indem die Probe mit der Spitze zeilenweise abgerastert wird. Hierbei bleiben Spitze und Probe entweder in ständigem Kontakt (Contact Mode), wobei sich das Bild der Oberfläche dann aus dem Deflection- und Höhenbild zusammensetzt. Eine andere Möglichkeit ist das Abrastern im Tapping Mode, in dem die Spitze zum Oszillieren gebracht wird, so dass sich das Bild der Oberfläche aus Änderungen der Amplitude der schwingenden Spitze ergibt, die durch Wechselwirkungen zwischen Spitze und Probe entstehen. Der Tapping Modus eignet sich besonders bei biologischen Proben, da die Proteine nicht so stark deformiert werden wie im Contact Mode. So wird eine Auflösung im Nanometerbereich erreicht, bei der Substrukturen reproduzierbar erkennbar sind, die vergleichbar mit der entsprechenden Kristallstruktur sind (Möller et al., 1999; Heymann et al., 1999). Dies erlaubt es, die Komplexbildung und Dynamik von Membranproteinen sichtbar zu machen, was zum einen durch den Vergleich vieler Bilder einzelner Proteine erreicht wird (Scheuring et al., 2003; Scheuring et al., 2004) und zum anderen durch die Weiterentwicklung der Methode zum Highspeed Imaging (Viani et al., 2000). Hierbei werden viele Bilder von der Probe mit einer Geschwindigkeit aufgenommen, die es erlaubt sie zu einem Film über die molekularen Vorgänge zusammen zu setzen.

2.2.2 Kraftspektroskopie

Im Gegensatz zum Abbilden, bei dem die Spitze die Probe möglichst nicht beeinflussen soll, wird bei der Kraftspektroskopie gerade ausgenutzt, dass die Probe durch die Spitze manipulierbar ist. Das zu untersuchende Protein wird hierbei kovalent an die Spitze

gebunden, so dass es beim Wegziehen der Spitze von der Unterlage auseinander gezogen wird und sich sequentiell entfaltet. Die kovalente Bindung wird entweder durch starkes Eindrücken der Spitze in die Probe mit entsprechend hohen Kräften (300-1000 pN) erreicht, (Oesterhelt et al., 2000) oder das Protein wird über spezielle Kopplungschemie spezifisch an die Spitze gebunden. Für Proteine wurden solche Versuche zuerst am Muskelprotein Titin (Rief et al., 1997) durchgeführt, bevor dann auch Messungen an Membranproteinen wie Bacteriorhodopsin (BR) (Oesterhelt et al., 2000), Halorhodopsin (Cisneros et al., 2005), dem Na/H-Antiporter (Kedrov et al., 2004) und anderen folgten. Für die Entfaltung von Membranproteinen nimmt vor allem das BR die Rolle als Modellsystem ein.

Nach früheren Entfaltungsexperimenten an BR wurde das Zwei-Schritt-Modell zur Faltung von Membranproteinen entwickelt. Hiernach bildet die Sekundärstruktur stabile Segmente in der Membran, die sich dann erst zur Tertiärstruktur formieren (Popot et al., 1987; Popot et al., 1990). Bei Kraftmessungen wird nun das Protein durch die Abstandsvergrößerung zwischen Spitze und Oberfläche entlang seines Polypeptidstranges auseinander gezogen, wodurch die Sekundärstrukturelemente in definierten Sequenzen (z. B. paarweise α-Helices) entfaltet werden, was durch definierte Zwischenabrisse (Peaks) zu sehen ist. Die Kraftkurve der Entfaltung eines einzelnen Proteins zeigt den Anstieg der Kraft bei Dehnung der Polypeptidkette mit zunehmendem Abstand. Die Kraft steigt bis sie so groß ist, dass die Sekundärstruktur nicht mehr stabil ist und sich entfaltet, so dass sich die Polypeptidkette verlängert und die Kraft wieder nachlässt bevor sie mit weiterem Ziehen erneut ansteigt (Abb. 2). In der Umkehrung faltet sich das Protein in Rückfaltungsexperimenten ebenfalls in diesen Segmenten (Janovjak et al., 2004). Die Abrisse werden mit einer Genauigkeit in z-Richtung von ca. 1 nm und die entsprechende Aufwendung von Kraft mit einer Genauigkeit von ca. 5 pN bestimmt. Die Kettenlänge der entfalteten Polypeptidkette und ihre Elastizität kann mit dem Worm Like Chain (WLC) Modell beschrieben werden (Bustamante et al., 1994). Im Gegensatz zum Freely Jointed Chain (FJC) Modell, das eine Kette als Aneinanderreihung vieler in sich steifer Glieder sieht, die nur an ihren Verlinkungen beweglich sind, stellt das WLC-Modell eine Kette dar, die mit einer gewissen Steifheit kontinuierlich beweglich ist. Ihre Dehnung x unter der Kraft F hängt von der thermischen Energie k_BT, der Konturlänge der Kette L_0 und der Persistenzlänge P ab:

$$\frac{FP}{k_B T} = \frac{1}{4}\left(1 - \frac{x}{L_0}\right)^{-2} - \frac{1}{4} + \frac{x}{L_0} \qquad [1]$$

Über die Beschreibung von Kraft-Weg Kurven mit dem WLC Fit können Kurven über ihre Länge und die Abstände der Abrisse zueinander selektiert werden.

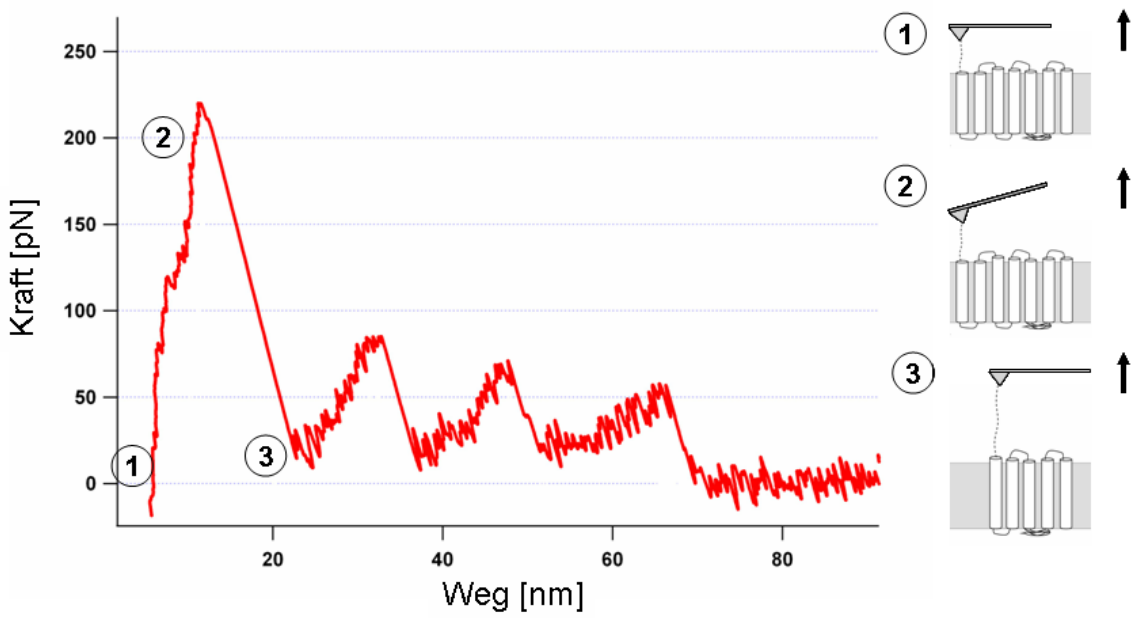

Abbildung 2: **Beispiel Kraftkurve und Schema**

Typische Kraftkurve der Entfaltung eines Bacteriorhodopsins (rote Kurve); das Schema zeigt den jeweiligen Zustand des Bacteriorhodopsins. (1) Die Spitze ist auf der Oberfläche, es wirkt noch keine Kraft. (2) Mit zunehmendem Weg, mit dem sich die Spitze von der Oberfläche entfernt, wird das Polypeptidkette des N-Terminus gedehnt und die Kraft steigt. (3) Der N-Terminus wurde so weit gedehnt, dass die Kraft auf die noch gefaltete Sekundärstruktur so groß wurde, dass sich die ersten beiden α-Helices entfalten. So wird die ungefaltete Polypeptidkette länger und die Kraft lässt nach. Mit weiterem Abstand zwischen Spitze und Probe wiederholt sich das sequentielle entfalten des Bacteriorhodopsins bis das Protein vollständig entfaltet und von der Oberfläche gelöst ist

2.3 Rasterkraftspektroskopie zur Untersuchung von Membranproteinen

Um funktions- und lebensfähig zu sein muss sich die Zelle von ihrer Umgebung abgrenzen; eukaryontische Zellen besitzen zudem verschiedene Kompartimente, in denen unterschiedliche Bedingungen herrschen. So können lebenswichtige Faktoren wie der Energiehaushalt in Mitochondrien oder die Entsorgung von überflüssigen Proteinen in Lysozymen aufrechterhalten und gesteuert werden. Für die Kompartimentierung sind Membrane verantwortlich, die nach dem Modell von Singer und Nicholson (Singer. und

Nicolson, 1972) aus einer zweidimensional flüssigen, doppelten Phospholipidschicht bestehen, in die entweder integrale Membranproteine eingebettet oder membrangebundene Proteine verankert sind. Die Phospholipidschicht ist impermeabel für Makromoleküle und nur selektiv permeabel für Ionen, so dass der Verkehr solcher Substanzen durch Membranproteine kontrolliert wird. Diese werden unterteilt in diejenigen, die den Transport aktiv gegen einen Konzentrationsgradienten unterstützen und als Pumpen unter Aufwendung von Energie zum Überleben der Zelle oder des Organismus beitragen oder in solche, die den Transport als Kanal ermöglichen und steuern und so Energie gewinnen können, wie zum Beispiel Bacteriorhodopsin (Berg, Tymoczko, Stryer, 2002).

Trotz dieser vielschichtigen Aufgaben und Relevanz von Membranproteinen, fällt auf, dass verhältnismäßig wenige Strukturen bekannt sind, wenn man die Anzahl veröffentlichter Strukturen von Membranproteinen mit der von löslichen Proteinen vergleicht. Dieses Verhältnis verlagert sich noch mehr bei der Betrachtung von Membrankomplexen und ihren bekannten Struktur-Funktionsbeziehungen und Mechanismen. Das mag sicherlich an der schwierigeren Handhabung von Membranproteinen liegen, und daran, dass es für viele biophysikalische Techniken erforderlich ist, dass das Protein in gelöster Form vorliegt. Es gibt deutlich weniger Kristallstrukturen von Membranproteinen, da die wegen ihrer Hydrophobizität hinzugefügten Detergenzien die für die Röntgenbeugung notwendige Kristallisation aus der Lösung erschweren. Ebenso zeigen sich momentan Grenzen in der Strukturbestimmung mittels NMR- (Nuclear Magnetic Resonance) Spektroskopie, die sich dadurch ergeben, dass sich Proben rekonstituierter Membranproteine in Lösung sehr anisotrop bewegen wodurch eine genaue Auswertung heute unmöglich ist. Dieses Problem kann zwar durch die Anwendung von Feskörper-NMR gelöst werden, aber auch hier sind die Daten der Messungen größerer Proteine zu komplex um Struktur-Funktionsbeziehungen zu erhalten.

Ungeachtet dessen sind bessere Kenntnisse der Struktur von Membranproteinen für die Medizin sehr wichtig, da Fehler in deren Struktur häufig verantwortlich für Krankheiten sind und sie auch oft als Ziel für Medikamente genutzt werden (Dobson et al., 1999).

Die Untersuchung von Membranproteinen mit dem Rasterkraftmikroskop hat wesentliche Vorteile: Membranproteine können innerhalb einer Membran untersucht werden, die Proteine können durch die induzierte kovalente Bindung zur Spitze direkt manipuliert werden und durch die Messung vieler einzelner Proteine können Aussagen über Subpopulationen getroffen werden, wie es Ensemblemessungen nicht ermöglichen würden. Für AFM-Messungen werden Membranproteine in künstlichen Lipiden rekonstituiert, auf

der Oberfläche adsorbiert und in Puffer gemessen. Dies erlaubt es Membranproteine unter Bedingungen abzubilden, die den nativen Bedingungen einigermaßen ähnlich sind. Im Gegensatz dazu stehen Messungen in Lösung oder in Mizellen, wie sie z. B. für NMR- oder EPR- (Electron Paramagnetic Resonance) Spektroskopie nötig sind, oder auch die Anordnung im Kristallgitter. Beim Abbilden kann die Oberflächenstruktur mit einer Auflösung von unter einem Nanometer sichtbar gemacht werden (Czajkowski et al., 1998; Engel und Müller, 2000), wobei die einwirkenden Kräfte von einigen Pikonewton biologische Bindungen und Anordnungen weitaus weniger beeinflussen, als es bei optischen Messungen oder durch Elektronenmikroskopie der Fall ist. Während bei der Elektronenmikroskopie die Energie der eingestrahlten Elektronen ausreicht, kovalente Bindungen zu brechen, erlauben die Messbedingungen optischer Methoden keine direkte hochauflösende Abbildung von Biomolekülen.

Ein weiterer Vorteil der Rasterkraftmikroskopie besteht darin, dass das untersuchte Protein durch die Interaktion mit der Spitze direkt manipulierbar ist. So sind durch Entfaltung auch intra- und intermolekulare Interaktionen, die bei der Proteinfaltung eine Rolle spielen, messbar (Kellermayer et al., 1997; Oesterhelt et al., 2000). Auch können Ligand-Rezeptor- Wechselwirkungen gemessen werden, indem der an die Spitze gekoppelte Ligand gezielt und unter definierten Bedingungen entsprechend zum Zielprotein positioniert werden kann.

Das Entfalten einzelner Moleküle erlaubt es individuelle Unterschiede der Faltungs- und Entfaltungswege, und damit die jeweiligen Ursprungszustände, aufzulösen, wie es in Ensemblemessungen nicht der Fall ist. So kann aus den Kraftmessungen auch ein Bild über die Energielandschaft und mögliche Faltungstrichter und deren Abhängigkeit von der physiologischen Umgebung gewonnen werden (Radford et al., 2000; Janovjak et al., 2004).

Zusammen mit den Kenntnissen der allgemeinen Struktur aus röntgenkristallografischen Daten und Ergebnissen der NMR-Messungen und den Erkenntnissen über die Dynamik einzelner gelabelter Aminosäuren aus z.B. EPR- oder Fluoreszenzmessungen trägt die Rasterkraftmikroskopie so erheblich zum grundlegenden Verständnis der Struktur-Funktionsbeziehungen von Membranproteinen bei.

3 Entwicklung und Anwendung von Methoden zur Bestimmung der freien Energielandschaft einer Bindung

Im folgenden Kapitel wird der Hintergrund zur Publikation „Direct and model free calculation of force-dependent dissociation rates from force spectroscopic data" beschrieben, die zusammen mit Dr. Filipp Oesterhelt entwickelt wurde und ein neues Modell zur Bestimmung der freien Energielandschaft einer Bindung vorstellt.

Durch die Faltung eines Proteins in seine korrekte Struktur wird aus einem Polypeptidstrang ein komplexes System, das durch definierte Bewegungsfreiheit seine spezielle Funktion erfüllen kann und so zu einer Maschine der Zelle wird. Die Faltung entsteht durch die Bildung der korrekten Bindungen innerhalb des Polypeptidstranges, die durch ihre spezielle Energielandschaft vorgegeben sind. Diese Energielandschaft kann entsprechend des Levinthal-Paradoxons als Faltungstrichter beschrieben werden (Levinthal, 1986). Demnach erfolgt die korrekte Faltung nicht durch zufälliges Ausprobieren aller möglichen Kombinationen an Bindungen, da dies rein rechnerisch zu Faltungszeiten von Proteinen führen würde, die in der Größenordnung des Alters der Erde liegen, sondern durch Bildung von Strukturelementen in einer trichterähnlichen Energielandschaft. Zudem wird sie durch zusätzliche Faltungshelferproteine (Chaperone) unterstützt (Buchner, 2002). Umgekehrt wird bei Kraftmessungen das Protein auseinander gezogen und so dessen Struktur aufgelöst. Wie oben beschrieben entfalten sich hier zuerst die Strukturelemente, wie α-helices oder β-Faltblätter. So beträgt die Lebensdauer einer einzelnen α-Helix 100 s und die paarweise angeordneter α-Helices 10 000 s, was der gleichen Größenordnung wie der der Stabilität löslicher Proteine entspricht (Janovjak et a., 2004). Der Vergleich der Entfaltungsmuster einzelner BR Proteine zeigt, dass neben den Hauptpeaks, die für alle BR Proteine gleich sind und die auf das Entfalten in Sekundärstrukturelemente hinweist, auch verschiedene Nebenpeaks auftreten, die auf unterschiedliche Entfaltungswege hindeuten. Hierbei zeigt sich, dass äußere physiologische Bedingungen eine wichtige Rolle in der Statistik spielen, welcher Entfaltungsweg bevorzugt wird. So hat die Temperatur (Janovjak et al., 2003), der pH-Wert (Kedrov et al., 2004) oder der oligomerische Zustand einen deutlichen Einfluss auf das Entfaltungsmuster.

Durch das Lösen einzelner Bindungen können unter Zuhilfenahme Kramers Theorie (Kramers, 1940) Teile des Energiepotentials mittels Kraftspektroskopie beschrieben werden. Hierbei bilden die stabilen Zustände Täler, die durch energetisch höhere Berge voneinander getrennt sind; um also vom Zustand A in einem Tal in den Zustand B des anderen Tals zu gelangen, muss ein energetisch höherer Übergangszustand B' durchlaufen werden (Abb. 3). Im Protein können diese zwei Zustände zum Beispiel die geöffnete und geschlossene Form eines Kanals sein, oder die aktive und inaktive Konformation eines Enzyms, oder der gebundene und ungebundene Zustand eines Rezeptor-Ligand Systems.

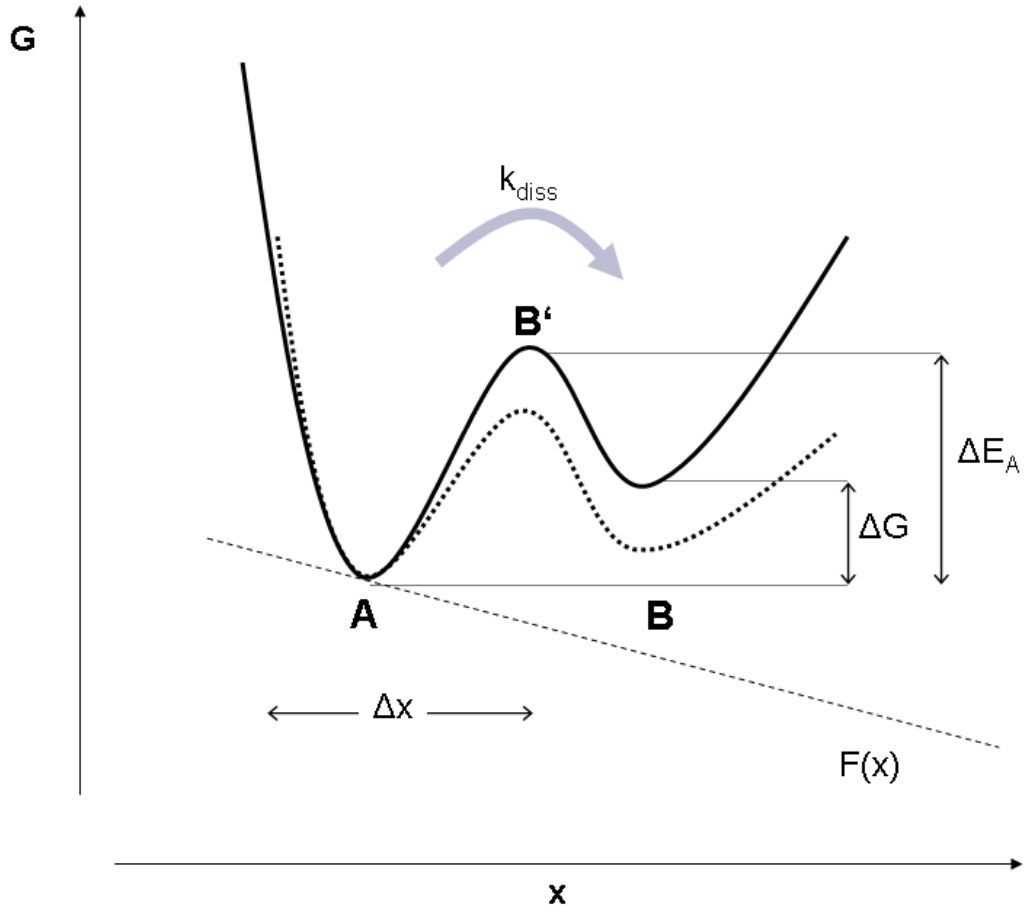

Abbildung 3: Schema der Energiepotentiale unter Einwirkung von Kraft

Gezeigt ist der Zusammenhang zwischen den Potentialen der Zustände A und B (durchgezogene Linie) und deren Änderung unter Einwirkung von Kraft (gestrichelte Linie). Durch die Ratenabhängigkeit der Abrisse kann wie in Formel [4] beschrieben die Weite des Energiepotentials Δx und seine Zerfallsrate k_{diss} bestimmt werden. Mithilfe von Jarzynskis Gleichung [5] lässt sich die Differenz der freien Energien der Gleichgewichtszustände ΔG beschreiben**.**

Die Häufigkeit mit der die Barriere überwunden wird, wird durch die Dissoziationsrate k_{diss} angegeben. Ohne äußere Einwirkung wird dieses Ereignis durch die Arrhenius-Gleichung beschrieben, wonach k_{diss} folgendermaßen von der thermischen Energie k_BT, der Aktivierungsenergie des Systems E_A und der charakteristischen Schwingungsfrequenz υ_0 abhängt:

$$k_{diss} = \upsilon_0 * \exp(\Delta E_A/k_BT). \qquad [2]$$

Durch Anlegen einer Kraft F reduziert sich die Aktivierungsenergie um das Produkt der Potentialweite Δx mit der angelegten Kraft (Bell et al., 1978; Evans et al., 1997):

$$k_{diss} = \upsilon_0 * \exp((\Delta E_A - F * \Delta x)/k_BT). \qquad [3]$$

Die Abhängigkeit der Dissoziationskonstante k_{diss} in dieser Gleichung erklärt sich dadurch, dass die Kraft bei den AFM-Messungen konstant ansteigt und das System daher nicht im Gleichgewicht gemessen wird. Bei langsamem Ziehen ist die Wahrscheinlichkeit, dass der Übergangszustand durch thermisches Rauschen überwunden wird, deutlich erhöht, so dass durchschnittlich geringere Abrisskräfte gemessen werden. Bei schnellerem Ziehen kann das System dagegen nicht schnell genug reagieren, um seinen Zustand direkt zu ändern, so dass die Kraft bis zum Lösen des Zustands weiter ansteigt und durchschnittlich höhere Kräfte gemessen werden. Nach Bell-Evans lassen sich die Dissoziationskonstante k_0 (bei der keine Kraft auf das System wirkt), sowie die Potentialweite Δx aus dem linearen Zusammenhang des Maximums der Kraftverteilung und dem Logarithmus der Ladungsrate F` bestimmen (Izrailev et al., 1997):

$$f = k_BT/\Delta x * \ln((F' * \Delta x)/(k_BT * k_{diss})). \qquad [4]$$

Die Ladungsrate hängt von der Federkonstante der Spitze und der Ziehgeschwindigkeit ab und gibt die Kraft an, die pro Zeiteinheit auf das System wirkt. Dies gilt allerdings nur unter der Annahme, dass der Kraftanstieg linear ist (Izrailev et al. 1997, Evans und Ritchie 1997) und gibt daher für viele Systeme nur einen Annäherung. Ein Beispiel ist der nichtlineare Kraftanstieg bei der Dehnung von PEG. Zudem vernachlässigt die Analyse weitere systematischer Messfehler. So unterliegt das Molekül durch die Ziehrichtung einer vorgegebenen Ausrichtung, was die Zahl der Freiheitsgrade reduziert. Auch werden das

Rauschen der Blattfeder und daraus resultierende Schwankungen in der gemessenen Kraft nicht mit in die Analyse einbezogen.
Obwohl auf diese Weise annäherungsweise die Potentialweite und die Lebensdauer eines Zustands bestimmt werden können, gibt diese Analyse keinen Aufschluss über die Freie Energiedifferenz zwischen den beiden Zuständen des Systems. Diesem Problem widmet sich die Jarzynski-Gleichung, die einen theoretischen Zusammenhang zwischen Nichtgleichgewichtsmessungen an beliebigen Systemen und Gleichgewichtsgrößen herstellt (Jarzynski, 1997; Liphardt et al., 2002). Sie beschreibt den Zusammenhang zwischen der Arbeit ΔW, die aufgewendet werden muss um vom Gleichgewichtszustand A zum Nichtgleichgewichtszustand B zu kommen, und der Differenz der freien Energien der Gleichgewichtszustände A und B:

$$\exp(-\Delta G/ k_B T) = < \exp(- \Delta W/ k_B T)> \qquad [5]$$

Der Mittelwert wird für eine große Zahl von experimentellen Realisierungen berechnet, bei denen sich zwangsläufig unterschiedliche Nichtgleichgewichtszustände B' ergeben.

In der Publikation „Direct and model free calculation of force-dependent dissociation rates from force spectroscopic data." (Oberbarnscheidt et al., 2009), die zusammen mit Dr. Filipp Oesterhelt entwickelt wurde, wird ein neues Modell zur Bestimmung des Energiepotentials vorgestellt, die es zum einen ermöglicht systematische Fehler durch thermisches Rauschen zu vermeiden und zum anderen nicht von einem Modell zum Fitten der Kurven abhängig ist. Die kraftabhängige Dissoziationskonstante ergibt sich hier aus dem Verhältnis zwischen der Anzahl der Kraftabrisse bei einer bestimmten Kraft und der aufsummierten Zeit in der bei dieser Kraft kein Abriss gemessen wurde und die aus den Daten aller Kraftkurven ermittelt wird.

4 Einfluss von inter- und intramolekularen Interaktionen auf den Mechanismus von Membranproteinen am Beispiel von Sensorhodopsin II

Im folgenden Kapitel wird der Hintergrund zu den Publikationen „Transducer binding establishes localized interactions to tune sensory rhodopsin II" und „Single-molecule force spectroscopy measures structural changes induced by light activation and transducer binding in sensory rhodopsin II" beschrieben. Erstere entstand in Zusammenarbeit mit Dr. David Cisneros aus der Gruppe von Prof. Dr. Daniel Müller, TU Dresden; die zweite beschreibt zum einen eine Weiterentwicklung der Analyse der Daten aus den Kraftkurven und neben dem Einfluss der Komplexbildung auch den der Lichtaktivierung.

Sensorhodopsin II (SRII) gehört zur Familie der Rhodopsine (Sharma et al., 2006; Klare et al., 2008), die Vertreter in allen drei Bereichen des Lebens hat. Ein bekannter Vertreter dieser Familie, der im Menschen vorkommt, ist das Rhodopsin, welches im Auge in den Stäbchen für das Hell-Dunkel-Sehen verantwortlich ist. Aber auch das Iodopsin, welches in den Zapfen lokalisiert ist und das Farbsehen ermöglicht, gehört zu dieser Familie.
Die Rhodopsine in Archeae sind so eng miteinander verwandt, dass nach Mutation spezieller Aminosäuren ein Rhodopsin, z.B. Bacteriorhodopsin, die Funktionen eines anderen, z.B. Sensorhodopsin, übernehmen kann (Sudo und Spudich, 2006), obwohl diese Funktionen sehr unterschiedlich sind. Der Mechanismus, der den mikrobiellen Rhodopsinen gemeinsam zugrunde liegt, ist mithilfe des Zusammenspiels verschiedenster biophysikalischer Techniken weitestgehend aufgeklärt (Review von Klare et al., 2008). So ist die Kristallstruktur von SRII, BR und anderen im Grundzustand, sowie in verschiedenen aktiven Zwischenzuständen verfügbar (Gordeliy et al., 2002; Moukhametzianov et al., 2006). Die allgemeine Struktur besteht aus sieben transmembranen α-Helices. Ein all-trans Retinal ist kovalent an die Mitte der siebten Helix gebunden, und befindet sich im aktiven Zentrum. Nach Lichtaktivierung findet eine 13-cis Isomerisierung des Retinals statt, wodurch sich anliegende Aminosäuren aufgrund sterischer Hinderung umorientieren. Diese Umorientierung leitet den Photozyklus ein, bei dem das Protein mehrere intermediäre Zustände durchläuft, die K, L, M, N und O genannt werden (Haupts et al., 1997; 1999). Obwohl alle Mitglieder der mikrobiellen Rhodopsine bei Aktivierung diesen Zyklus durchlaufen, zeigen sich doch deutliche Unterschiede in der

Geschwindigkeit (Klare et al., 2008). So durchläuft BR den Photozyklus ungefähr hundertmal so schnell wie SRII.

Die strukturellen Änderungen im aktiven Zentrum wirken sich auf das gesamte Protein aus, so dass sich die Helix F nach Aktivierung nach außen dreht (Klare et al., 2008; 2004). Für BR wird beschrieben, dass der cytoplasmatische Kanal durch die Drehung von Helix F besser für Protonen zugänglich wird. Dadurch wird die Aktivität des Proteins als Protonenpumpe ermöglicht (Spudich, 1998). Das Sensorhodopsin II pumpt in Abwesenheit seines Transducers auch Protonen, wenngleich auch mit einer viel niedrigeren Turnover Rate (Schmies et al., 2001; Sudo et al., 2001)), und ist hauptsächlich für Phototaxis zuständig. Während SRI für positive Phototaxis verantwortlich ist und dafür sorgt, dass sich der Organismus zur Energie liefernden Lichtquelle hinbewegt, absorbiert SRII Licht in dem Bereich, der schädlich für den Organismus ist, und setzt über seinen Transducer HtrII eine Signalkaskade in Gang, die negative Phototaxis veranlasst. Der Transducer HtrII besitzt zwei transmembrane Helices (TM1 und TM2) und eine große cytoplasmatische Domäne (Klare et al., 2004; Spudich, 2006). SRII bindet HtrII hauptsächlich über der gesamten Länge von Helix F von NpSRII, sowie dem EF loop mit Helix TM2 des Transducers (Hippler-Mreyen et al., 2003; Yang et al., 2004; Wegener et al., 2000). Die durch die Lichtaktivierung induzierte Auswärtsbewegung von Helix F des SRII überträgt das Signal auf den Transducer, dessen cytoplasmatische Domäne an der Weiterleitung des Signals an eine Phosphorylierungskaskade beteiligt ist. Am Ende der Signalkaskade wird der flagellare Motor des Archeons aktiviert und es entfernt sich von der Lichtquelle (Rudolph und Oesterhelt, 1995; 1996).

Das Sensorhodopsin II eignet sich aus mehreren Gründen gut als Modellsystem zur Untersuchung eines Membrankomplexes mittels Kraftspektroskopie: Erstens ist es dem Bacteriorhodopsin sehr ähnlich, dessen Entfaltung unter verschiedenen Bedingungen bereits beschrieben ist (Janovjak et al., 2006) und zweitens sind auch die Mechanismen der Aktivierung und Signalübertragung weitestgehend durch andere biophysikalische Methoden bekannt (Klare et al., 2008). Dies erlaubt es die kraftspektroskopischen Daten des Komplexes im aktiven und nicht aktiven Zustand einzuordnen und Aussagen über AFM-Messungen von inter- und intramolekularen Interaktionen in einem Membrankomplex im Allgemeinen zu treffen. Zudem bleibt es ein interessantes System, da die Komplexbildung zu so unterschiedlichen inter- und intramolekularen Wechselwirkungen führt, die direkten Einfluss auf die Struktur- Funktionsbeziehung haben.

In dieser Arbeit wurden mittels Rasterkraftspektroskopie Änderungen der molekularen Stabilität durch Änderung intra- und intermolekularer Interaktionen in bestimmten Regionen des Proteins identifiziert, die durch die Komplexbildung und/oder Aktivierung beeinflusst werden. Somit wurde ein tieferes Verständnis der Auswirkung von Komplexbildung in Membranproteinen auf ihren Mechanismus und damit ihre Struktur-Funktionsbeziehung gewonnen.

Die Publikation „Transducer binding establishes localized interactions to tune sensory rhodopsin II“ (Cisneros DA, Oberbarnscheidt L, Pannier A, Klare JP, Helenius J, Engelhard M, Oesterhelt F, Muller DJ., 2008) beschreibt welche Auswirkung die Bindung des Transducers auf die Stabilität innerhalb des Sensorhodopsin II hat. Um die Änderung der Stabilität in Regionen von wenigen Aminosäuren zu bestimmen, wurden Kraftkurven der Entfaltung von Sensorhodopsin II erst in An- und Abwesenheit des Transducers und später auch im aktiven und nicht-aktiven Zustand aufgenommen und miteinander verglichen. Hier wurde die Auswirkung der Komplexbildung auf die Änderung inter- und intramolekularer Interaktionen als Durchschnittskraft berechnet, indem die Daten der Kraftkurven der Einzelmolekülmessungen zusammengefasst und als Ensemblemessung behandelt wurden. Histogramme über die gemittelte Durchschnittskraft ergeben sich demnach aus dem Produkt der Häufigkeit eines Abrisses in einem festgelegten Bereich und der entsprechenden Kraft, die zu diesem Abriss führt. Mit dieser Analyse zeigte sich eine Stabilisierung der meisten Teile von Helices G und F, die in direktem Kontakt zum Transducer stehen. Daraus lässt sich auch die Bedeutung dieser Regionen für die unterschiedliche Funktionsweise des Rezeptors ableiten. Die Analyse der Berechnung der Durchschnittskraft zeigt sich also als sehr geradlinige Methode kraftspektroskopische Daten auszuwerten um die Stärke inter- und intramolekularer Interaktionen eines Membrankomplexes zu bestimmen und diese zu lokalisieren, vor allem weil sich kein direkter Zusammenhang zwischen Abrisshäufigkeit und –stärke feststellen lässt.

Die Publikation „Single-molecule force spectroscopy measures structural changes induced by light activation and transducer binding in sensory rhodopsin II” (Oberbarnscheidt L, Janissen R, Martell S, Engelhard M, Oesterhelt F., 2009) vergleicht nicht nur die Änderungen durch Binden des Transducers, sondern auch den Einfluss der Lichtaktivierung. Um nun den Einfluss der Änderung der Stabilität besser zu verstehen, wurde nicht nur der Einfluss der Komplexbildung, sondern auch der der Lichtaktivierung verglichen und das Analyseverfahren weiter entwickelt. Dadurch, dass bei der

Durchschnittskraft alle Daten zusammengenommen und dann als Ensemblemessung gewertet werden, gehen Informationen über den Einfluss der einzelnen Proteine und die Bandbreite ihres Verhaltens verloren. Durch die Multiplikation ist auch der Einfluss der Kraftstärke nicht von dem der Abrisshäufigkeit zu unterscheiden. Daher wurde beim weiterentwickelten Analyseverfahren die Auswertung der Häufigkeit der Kraftabrisse getrennt von der Kraft der Abrisse analysiert. Im Gegensatz zur Durchschnittskraft, wurde die Stabilität also mit der Häufigkeit der Abrisse angegeben ohne ihre Stärke zu berücksichtigen. So werden Regionen innerhalb des Proteins bis auf wenige Aminosäuren genau bestimmt, in denen Interaktionen zur Entfaltung der Struktur gebrochen werden müssen. Um eine höhere Auflösung zu erreichen, wurde die Breite der Balken des Histogramms variiert und der entsprechenden Anzahl der Ereignisse angepasst. Zusätzlich wurde der Fehler eines willkürlich gewählten Startpunktes und damit einhergehende Minderung der Auflösung vermieden, indem sich das endgültige Histogramm über die Abrisshäufigkeiten bei der Entfaltung des Proteins aus der Mittelung vieler Histogramme mit variierendem Startpunkt berechnet wurde. Mit dieser Analyse konnten zusätzlich zu den durch den Vergleich der Durchschnittskraft bereits beschriebenen Regionen verschiedene andere Regionen im Sensorhodopsin II genauer identifiziert werden, die bei der Aktivierung eine Rolle spielen und in denen das Binden des Komplexpartners einen Einfluss ausübt.

Bei dieser Art der Analyse wurde der Fokus auf die Häufigkeit der Abrisse gelegt ohne die Kraft, mit der dieser Abriss stattfindet, zu berücksichtigen. Unter Berücksichtigung der Kraft kann anhand der in Kapitel 2 beschriebenen Analysmethode die Energielandschaft der Faltung und Stabilität von Membranproteinen weiter analysiert werden.

Um die Energiepotentiale von Bindungen innerhalb transmembraner Helices zu testen, wird eine große Anzahl von Daten benötigt um eine gute Statistik zu garantieren. Daher wurden außer von SRII in den unterschiedlichen Zuständen auch Kraftkurven der Mutante von Bacteriorhodopsin BR D96N aufgenommen. Bacteriorhodopsin ist ein enger Verwandter von Sensorhodopsin; beide haben eine ähnliche Struktur und auch eine sehr ähnliche Anordnung von Aminosäuren im aktiven Zentrum. In Abwesenheit des Transducers verhält sich SRII wie BR und pumpt Protonen durch die Membran, wenngleich auch deutlich langsamer. Frühere Studien zeigten, dass die Funktion von BR auch umgekehrt an den Transducer binden und die Funktion von SRII übernehmen kann, wenn entsprechende Aminosäuren mutiert sind (Sudo and Spudich, 2006). Durch die

Mutation in der BR D96N Mutante, bei der die Asparaginsäure im aktiven Zentrum durch Lysin ersetzt wurde, verlangsamt BR seine Aktivität, so dass der aktive Zustand noch mit dem AFM aufgelöst werden und die Stabilität von BR im aktiven und nicht aktiven Zustand verglichen werden kann. Da die Aufnahmerate auswertbarer Kraftkurven von Bacteriorhodopsin zehn- bis dreißig mal höher ist als die von Sensorhodopsin, sollte die neue Analysemethode erst für Bacteriorhodopsin getestet werden, was eine bessere Statistik gewährleistet, und erst dann auf die Kraftkurven aus den Messungen von Sensorhodopsin angewendet werden.

5 Oberflächenfunktionalisierung und Spitzenmodifikation

Im folgenden Kapitel wird der Hintergrund zur Publikation „Optimized straight forward procedure for covalent surface immobilization of different biomolecules for single molecule applications" beschrieben. Um die zu untersuchenden Proben gerichtet und in einer definierten Konzentration anzubinden und die Kraftkurven über einen Linker optimal selektieren und auswerten zu können, wurde in Zusammenarbeit mit Dr. Richard Janissen ein Oberflächenprotokoll entwickelt, dass eine schnelle, saubere, kontrollierte und gerichtete Anbindung von Biomolekülen über einen PEG- Linker an eine aktivierte Oberfläche ermöglicht. Das Protokoll ist besonders für die Präparation von Proben für die Rasterkraftspektroskopie und –mikroskopie geeignet.

Um die Interaktionen einzelner Bindungspartner zu messen, ist es erforderlich, dass beide Partner kontrolliert zueinander positioniert werden. Hierzu wird ein Bindungspartner, zum Beispiel ein Rezeptor, definiert und in bestimmter Ausrichtung an die Oberfläche gebunden, während der andere, zum Beispiel ein Ligand, an die Spitze gebunden wird. Um Einzelmolekülmessungen zu gewährleisten, muss die Oberfläche homogen funktionalisiert werden, wobei jegliche Verunreinigungen zu vermeiden sind. Zudem muss die Möglichkeit bestehen, die Konzentration der Bindungspartner zu regulieren, so dass nur eine Bindung entsteht und damit auch nur eine Bindung gemessen wird, wenn die Spitze an die Oberfläche angenähert wird. Dies wird meist durch einen Polymerteppich aus PEG (Polyethlyenglycol)-Linkern erreicht. Die Verwendung dieses Linkers birgt weitere Vorteile, da er für einen Abstand des zu untersuchenden Moleküls von der Oberfläche sorgt und somit sterische Probleme reduziert. Zusätzlich können spezifische Kraftabrisse durch das bekannte Muster der Ausdehnung von PEG in den Kraft-Abstandskurven selektiert werden und sind so von Kraftabrissen, die durch unspezifische Interaktionen verursacht werden, zu unterscheiden.
Um den PEG-Linker sowohl an die Oberfläche als auch an das zu untersuchende Molekül zu binden, werden PEG-Polymere verwendet, die an beiden Enden reaktive, funktionale Gruppen besitzen (Veronese, 2001; Roberts et al., 2002). Zur Kopplung von Proteinen oder Peptiden werden häufig Amino- mit Carboxygruppen (aktiviert zu NHS-Estern) gekoppelt. Eine weitere gängige Alternative ist die Kopplung von Thiolgruppen von Cysteinen mit Maleimid, wohingegen die Reaktion von Epoxy- oder Aldehydgruppen mit Alkoholen

weniger oft zum Einsatz kommt. Um eine Carboxylgruppe mit einer Aminogruppe eines Lysins zu koppeln, wird sie mit einem Carbodiimid wie EDC (Ethyl(dimethylaminopropyl) Carbodiimid) oder DIC (Dicyclohexylcarbodiimid) zu NHS-(N-Hydroxysuccinylimid) Ester aktiviert. Im Gegensatz zur Carboxygruppe bildet der NHS- Ester eine gute Abgangsgruppe, die in Anwesenheit einer Base mit Aminogruppen reagiert, so dass eine Peptidbindung entsteht. Umgekehrt kann auch die Carboxygruppe eines Aspartats oder Glutamats aktiviert werden und mit aminofunktionalisiertem PEG reagieren. Um Kreuzreaktionen und daraus entstehende Polymerisierung von Biomolekülen zu verhindern, wird Schutzgruppenchemie angewandt. Das bedeutet, dass z. B. die Aminogruppen des zu untersuchenden Moleküls geschützt werden, wenn es über seine aktivierte Carboxygruppe an eine aminofunktionalisierte Oberfläche gebunden werden soll. Üblicherweise werden Aminogruppen entweder mit dem Carbonsäureester BOC (Di-tert-butyl dicarbonat) oder Fmoc (Fluorenylmethyloxycarbonyl chlorid) geschützt. BOC reagiert in wässriger, basischer Umgebung mit dem Amin, und lässt sich durch Zugabe von Säure (meist Trifluoressigsäure) leicht entfernen. Dies erlaubt orthogonales Schützen von Fmoc, das in Anwesenheit von Salzsäure bindet und durch basische Bedingungen abgespalten werden kann.

Am einfachsten wird die Anbindung des zu untersuchenden Biomoleküls durch Fluoreszenz nachgewiesen. Abhängig von den Eigenschaften des entsprechenden Moleküls wird es entweder durch Fluoreszenz gelabelte Antikörper markiert oder es wird ein Fluorophor in einem weiteren Schritt kovalent gebunden. Die Intensität der mit einer CCD-Kamera gemessenen Fluoreszenz erlaubt Rückschlüsse auf die Effizienz und Homogenität der Anbindung. Durch Negativ-Kontrollen müssen hierbei Fluoreszenz von unspezifischen Wechselwirkungen oder Verunreinigungen ausgeschlossen werden.

6 Einfluss der Multivalenz des Ni- NTA- Histag Symstems auf seine Eigenschaft als molekularer Griff

Im folgenden Kapitel wird der Hintergrund zum Manuskript für die Publikation „Multivalent interactions in flexible interaction pairs increase their affinity but not the mechanical stability“ beschrieben. Das Projekt entstand in Kooperation mit der Gruppe von Prof. Dr. Jacob Piehler, wobei NTA-funktionalisierte Oberflächen von Dr. Annett Reichel vorbereitet wurden und Herr Maniraj Bhagawati die Affinitäts-Messungen der verschiedenen Komplexe durchführte.

Um Entfaltungskurven von Membranproteinen zu messen, muss die Spitze mit dem Terminus des Proteins interagieren. Bei den Messungen von Sensorhodopsin II wurde diese Bindung erreicht, indem die Spitze unspezifisch in eine Membran, die rekonstituiertes Sensorhodopsin II enthielt, gedrückt wurde. Dadurch, dass der Terminus einige Aminosäuren lang aus der Membran herausragt, war die Wahrscheinlichkeit am größten, dass die Spitze das Protein am Terminus bindet. Die entsprechenden Kraftkurven der Entfaltung des Proteins konnten zwar über die Länge selektiert werden, aber die exakte Position der Aminosäure, die mit der Spitze interagiert, kann bei dieser Art des Experiments nicht bestimmt werden. Zudem kommt es durch das kräftige Eindrücken leicht zu Verunreinigungen der Spitze. Um das Protein gezielt an einer Aminosäure zu greifen, können auch Spitzen aus Gold verwendet werden, die bevorzugt mit einem rekombinanten Cystein am Terminus des Zielproteins interagieren (Oesterhelt et al., 2000). Diese Methode hat aber den Nachteil, dass die Spitze schnell mit Proteinen verunreinigt ist und oft ausgewechselt werden muss.

Eine gute Alternative wäre ein molekularer Griff, mit dem das Protein von Interesse gezielt mit der Spitze aus der Membran gezogen werden kann. Diese Alternative würde es auch erlauben, die Entfaltung des Proteins nicht nur in einer rekonstituierten Membran, sondern auch in der Umgebung seiner natürlichen Membran zu untersuchen. Der NTA (Nitrilotriessigsäure)-Komplex ist in der Biochemie und Molekularbiologie bereits ein gängiges Werkzeug um Proteine über einen Histag aufzureinigen. Der Histag besteht aus sechs rekombinanten Histidinen, die am Terminus des Zielproteins exprimiert werden. Der Komplex bildet sich, indem ein zentrales Nickelatom vier koordinative Bindungen zum NTA ausbildet und die verbleibenden zwei Koordinationsstellen mit den Histidinen

interagieren. Aufgrund dieser Eigenschaften eignet sich der Komplex auch gut als Werkzeug, um ein Membranprotein von Interesse mit einem über einen Linker an die Spitze gebundenes Ni-NTA sauber aus der Membran zu ziehen (Schmitt et al., 2000). Hierzu müssen die Kräfte des Komplexes größer sein als die Kräfte, die zur Entfaltung des Proteins nötig sind. Frühere Kraftmessungen ergaben sehr unterschiedliche Kräfte in einem Bereich zwischen 38 pN und 500 pN für die Bindung eines einzelnen mono-NTA/His6 Komplexes (Conti et al., 2000; Schmitt et al., 2000; Kienberger et al., 2000; Verbelen et al., 2007; Valle et al., 2008). Diese Unterschiede lassen sich nicht durch die Kraftrate erklären und sind wahrscheinlich das Resultat vielfacher Interaktionen.

Der Mono-NTA/His6 Komplex ist sehr dynamisch. Studien haben gezeigt, dass die Affinität durch Multivalenz deutlich erhöht wird (Lata et al., 2005). Dazu wurden Konstrukte mit drei NTAs (Tris-NTA) entwickelt, an die sechs Histidine binden können. Kraftmessungen an multivalenten Systemen haben gezeigt, dass die durch die Multivalenz bedingten Kräfte von der Geometrie des Systems abhängig sind (Sulchek et al., 2006). Das wahrscheinlich bekannteste Beispiel von Kraftmessungen an einem multivalenten Biomolekül ist antiparallele DNA. Hier werden die komplementären Basen über viele Basenpaare hinweg reißverschlussartig gebrochen, was sich in der Kraftkurve in einem Kraftplateau mit einer relativ geringen Kraft von etwa 60 pN (Clausen-Schaumann et al., 2000) zeigt. Ein solches Kraftplateau entsteht, wenn die einzelnen Bindungen sequentiell abreißen, was nur dann der Fall ist, wenn der Abstand zwischen den jeweiligen Bindungen lang genug ist um zu erlauben, dass die Kraft auf jede Bindung einzeln wirken kann. Falls dies nicht der Fall ist und die Abstände zwischen den einzelnen Bindungen so kurz sind, dass die Kraft parallel anliegt, sind viel größere mechanische Kräfte notwendig, um die multivalente Bindung zu brechen (Sulchek et al., 2006; Ratto et al., 2006).

Die Geometrie des NTA ist so komplex, dass es nicht intuitiv vorherzusehen ist, ob die erhöhte Multivalenz, die zu höherer Affinität führt, auch eine höhere mechanische Stabilität gewährleistet. Dies wurde wie im Manuskript zur Publikation „Multivalent interactions in flexible interaction pairs increase their affinity but not the mechanical stability“ beschrieben, untersucht**.** Interessanterweise zeigte sich, dass mit zunehmender Multivalenz zwar die Affinität, aber nicht die mechanische Stabilität des Ni- NTA-Histag Systems zunimmt. Die Lebenszeiten aller Systeme ändern sich bei den Kraftmessungen nicht, während sie bei den Affinitätsmessungen an der Oberfläche von Mono-NTA/His2, über Tris-NTA/His2, dann Mono-NTA/His6 bis schlussendlich Tris-NTA/His6 zunehmen. Im Vergleich entsprechen alle Lebenszeiten der Kraftmessungen denen des Mono-

NTA/His2 der Affinitätsmessung, so dass davon auszugehen ist, dass die Geometrie des Systems dazu führt, dass die angelegte Kraft auf nur eine Mono-NTA/His2 Interaktion gleichzeitig wirkt. Gleichzeitig bedeutet dies für die Affinitätsmessung, dass die Rückbindungsraten, die in den Kraftmessungen mechanisch verhindert werden, ausreichend hoch sind, um zusammen mit einer höheren Multivalenz für die ausreichende Stabilität beim Anbinden von Proteinen an Säulen oder Oberflächen zu sorgen. Daraus ist auf eine Geometrie des tris-NTA Komplexes zu schließen, die eine antiparallele Bindung mit dem His-Peptid erlaubt und somit zu einem sequentiellen Abreißen von einzelnen NTA/His-Bindungen führt. Die angestrebte Verwendung des NTA-Systems als molekularen Griff, der ausreichend hohe Kräfte in der Kraftspektroskopie aushält, erfordert eine erhöhte mechanische Bindungskraft des NTA-Systems.

7 Das Lantibiotikum Nisin und der ABC- Transporter NisT

Nisin ist ein Antibiotika, das vor allem verwendet wird um Milch- und Backprodukte, sowie Gemüse, Fleisch und Fisch haltbar zu machen. Als Modell-Lantibiotikum ist seine Biosynthese und Wirkungsweise Ziel verschiedener Untersuchungen (Lubelski et al., 2008). Es tötet grampositive Bakterien, indem es an Lipid II der Zellmembran bindet und dort eine Pore aus acht Nisinmolekülen und vier Lipid II Molekülen bildet, die einen Durchmesser von 2 bis 2,5 Nanometern besitzt. Lipid II besitzt eine Undecaprenylkette, die über Diphosphat an N-Acetylmuramin gebunden ist, was zusammen mit N-Acetylglucosamin das Rückrat des Peptidoglycan-Netzwerks der Zellwand zusammenhält. Durch die Bildung von Poren wird die Membran permeabilisiert und die Zellwandsynthese inhibiert, was letztendlich zum Tod des Bakteriums führt. In der Zelle reichen nanomolare Konzentrationen aus um die Membran zu permeabilisieren, wohingegen aber mikromolare Konzentrationen zum Permeabilisieren künstlicher Membranen nötig sind.

Nisin wird in *Lactococcus lactis*, einem gram-positiven Bakterium, das zur Herstellung von Buttermilch und Käse verwendet wird, produziert. Dort wird es zuerst als nicht aktives Präpeptid (Pränisin) synthetisiert. Aktives Nisin besitzt ein Lanthionin, vier Methyllanthionine, ein Dehydrobutyrin, zwei Dehydroalanine sowie einundzwanzig unmodifizierte Aminosäuren und entsteht durch mehrfache Modifikationen des 57 Aminosäure langen Präpeptides (Abb. 4) (Kaletta and Entian, 1989).

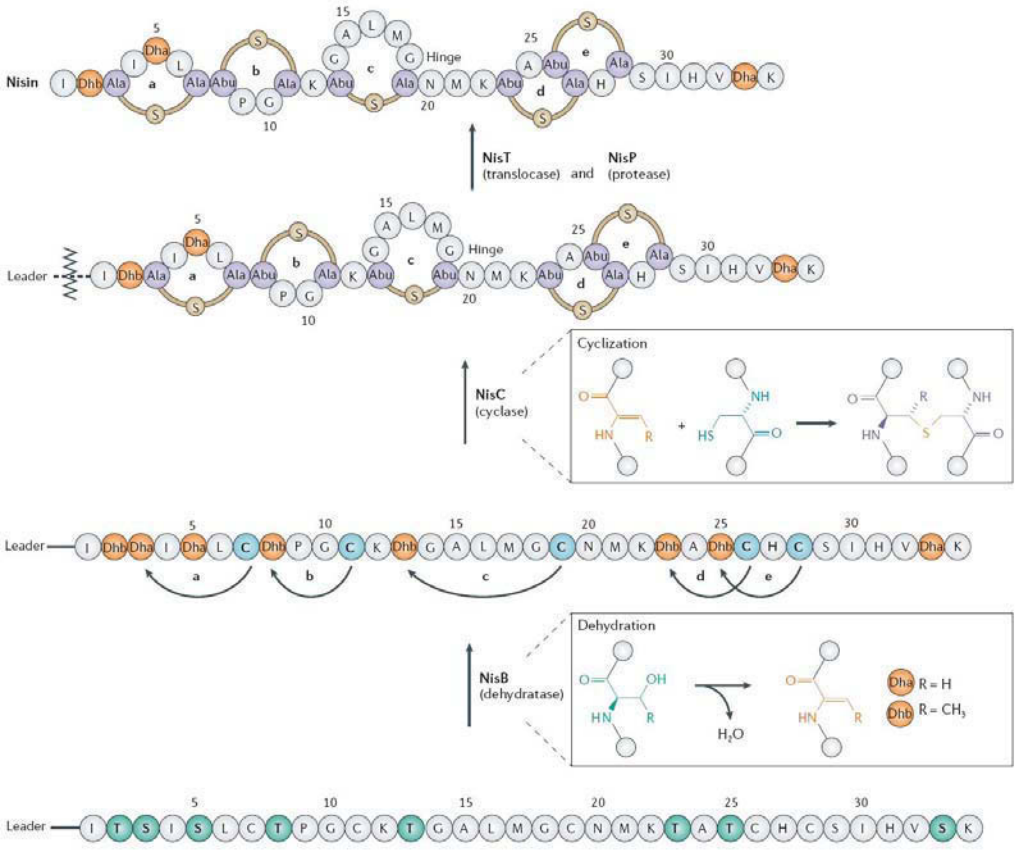

Abbildung 4: Strukturformel von Pränisin, übernommen von Chatterjee et al., 2005

Im ersten Modifikationsschritt werden Serine und Threonine von NisB dehydriert, woraufhin die Cyclase NisC eine regioselektive Ringbildung aus den dehydrierten Aminosäuren und Cysteinen katalysiert. Das immer noch inaktive Pränisin wird durch den ABC-Transporter NisT durch die Membran transportiert, wo es dann durch Abspalten der 23 Aminosäure langen Präsequenz durch die Protease NisP aktiviert wird. Die Biosynthese von Nisin wird durch einen Rückkopplungsmechanismus über das zwei Komponenten-System NisRK reguliert (Abb. 4, 5). Interessanterweise bilden die Enzyme, die an der Synthese von Nisin (NisC als Dimer, NisB und NisT als Dimer) (Siegers, et al., 1996) beteiligt sind, einen membranassoziierten Komplex, der aber nicht essentiell für die Funktion der einzelnen Enzyme ist (Siegers, et al., 1996). Der Transport von Pränisin ist bisher nur indirekt durch Knockout Studien und Überexpression nachgewiesen. Eine bisherige Charakterisierung hat gezeigt, dass NisT eine breite Substratspezifität besitzt, da es auch nicht modifiziertes Nisin sowie andere Peptide, unter anderem auch Nicht-Lantibiotika, durch die Membran transportiert, sofern sie an die Leadersequenz von Nisin gekoppelt sind (Kuipers et al., 2004).

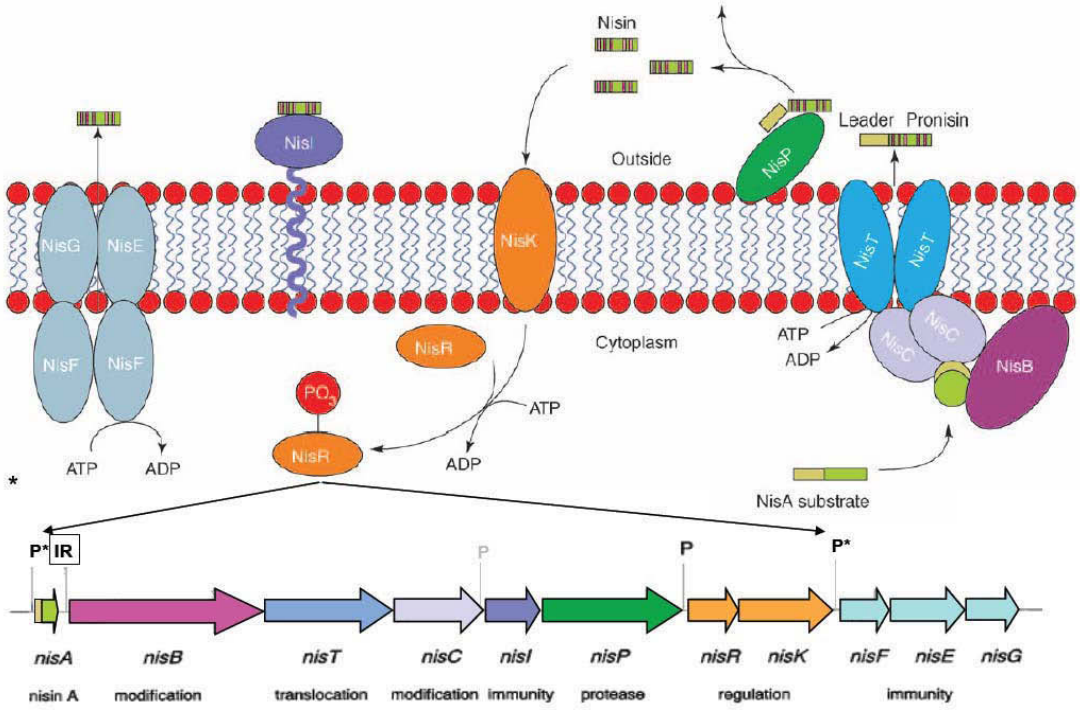

Abbildung 5: Posttranslationale Modifizierungsmaschinerie von Nisin, übernommen von Patton et al., 2005

NisT gehört zur Familie der ABC Transporter (ATP binding cassette), deren wohl bekanntester Vertreter - das P-Glykoprotein - für die Drogenresistenz verantwortlich ist (Kartner et al., 1983, Leslie et al., 2005). ABC-Transporter sind entsprechend ihrer Quartärstruktur in drei Hauptklassen unterteilt. Zur Klasse 1 gehören ABC Transporter, die in einer einzigen Polypeptidkette exprimiert werden. ABC-Proteine, die nicht an eine Transmembrandomäne gekoppelt sind, gehören zur Klasse 2 und solche, in denen die ABC-Domäne und die Transmembrandomäne in zwei Polypeptidketten exprimiert werden, werden der Klasse 3 zugeordnet. Allgemein bilden ABC-Transporter ein Homodimer, der jeweils aus einer Transmembrandomäne (TMD) und einer ins Cytoplasma orientierten Nukleotid bindenden Domäne (Nucleotide Binding Domain, NBD) besteht (Kenneth et al., 2003; Oswald et al., 2006). Während sich in der TMD Domäne von Exportern wenig generelle Gemeinsamkeiten finden lassen, besitzt die NBD verschiedene charakteristische Motive. Da sie durch die Hydrolyse von ATP die Energie für den Transport aufbringt, ist sie in allen drei Bereichen des Lebens konserviert.

NisT gehört zu den Exportern von denen eine bekannte Kristallstruktur, die des putativen MDR (multi drug resistance) Protein Sav1866 from *S. aureus* (Dawson and Locher, 2006) (Abb. 6) ist.

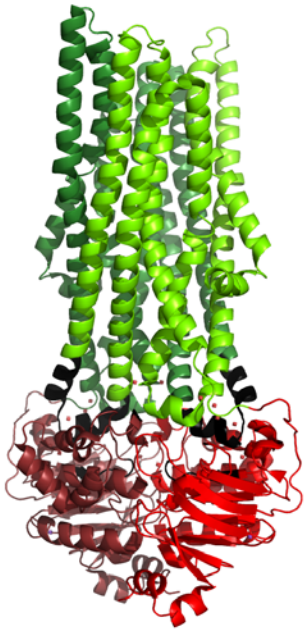

Abbildung 6: **Struktur des putative MDR (multidrug resistance) Protein Sav1866 aus *S. aureus*** (Dawson and Locher, 2006). Sie ist ein Beispiel einer Kristallstruktur eines ABC-Exporters und zeigt das Homodimer mit den beiden TMDs (grün) und der NBD (rot).

Entsprechend dem allgemeinen Modell für ABC-Transporter (Lu et al., 2005; Zaitseva et al., 2006) induziert das Binden von ATP eine Dimerisierung. Nach der ATP Hydrolyse dissoziiert der Dimer und ADP wird entlassen.

In der vorliegenden Arbeit ist die Bindung von Pränisin an den Transporter NisT untersucht worden, wobei die weiter oben beschriebenen Methoden angewendet wurden. Hierzu wurde Pränisin am C-terminalen Ende über einen PEG-Linker an die AFM-Spitze gebunden um es mit dem AFM gezielt an inside-out Vesikel zu positionieren, die 80 % überexprimiertes NisT enthalten. Aus den daraus resultierenden Kraftkurven soll das Bindungspotential der Interaktion bestimmt werden.

7.1 Material und Methoden

7.1.1 Herstellung Pränisin

Die Reinigung von Pränisin erfolgte nach einem im Institut für Biochemie der Heinrich-Heine Universität Düsseldorf etablierten Protokoll. Zur Produktion von Pränisin wurden über Nacht *Lactococcus lac tis* Bakterien, in M17 Medium kultiviert. Anschließend wuchsen sie eine weitere Nacht in 500 ml Minimal Medium (Jensen und Hammer, 1993).

Nach dem Abzentrifugieren der Bakterien (Sorvall SLA 30 000, 10 000 rpm, 20 min 8 °C) wurde das Pränisin aus dem gefilterten und mit gleichem Volumen von 50 mM Milchpuffer verdünnten Überstand über Ionenaustauschchromatographie (5 ml HiTrap, GE Healthcare) aufgereinigt. Die Elution erfolgte in 50 mM Milchsäure, 1 M NaCl und es wurden 1 ml Fraktionen gesammelt.
Die Fraktionen mit Pränisin wurden über SDS- Gelelektrophorese mit anschließender Silberfärbung überprüft. Das Pränisin wurde durch TCA Fällung pelletiert und bei -20 °C gelagert.

7.1.2 Schutz mit BOC

Um eine Aggregation durch ungewollte Kopplung zwischen der terminalen Carboxygruppe und den Aminen der Lysine von Pränisin bei der Oberflächenfunktionalisierung zu vermeiden, werden die Amine des aufgereinigten Pränisins mit der Schutzgruppe BOC geschützt. Hierzu wurde das Peptid im späteren Reaktionspuffer (100 mM MES) gelöst und die Lösung mit Natronlauge basisch gemacht. Das BOC-Anhydrid wurde in einer Konzentration von 15 mM in p-Dioxan gelöst und zur Peptidlösung hinzu gegeben, so dass die Probe über Nacht bei Raumtemperatur reagieren konnte. Nach Zugabe von Wasser konnte das nun geschützte Pränisin mit Ethylacetat extrahiert werden.

7.1.3 Anbinden Pränisin

Die Anbindung von Pränisin wurde ausgehend vom Protokoll der Oberflächenpräparation nach Janissen et al., 2009 entwickelt. Hierzu wurden saubere Glasoberflächen mit 5 M Ethanolaminehydrochlorid gelöst in DMSO über Nacht bei Raumtemperatur inkubiert, in Wasser gewaschen und im Stickstoffstrom getrocknet. Anschließend erfolgte die Reaktion mit PEG in einer Lösung aus 2 mM NHS-PEG-COOH (MW 3000, Iris Biotech) gelöst in 1,5 ml Chloroform (ChromosolvV) und 30 µl Triethylamin für 1 h bei Raumtemperatur. Nach erneutem Waschen in Wasser und anschließendem Trocknen wurde die Carboxygruppe des PEG durch Inkubieren in 100 mM Ethylendiamin und 10 mM EDC gelöst in 100 mM MES, pH 4,7 für 1 Stunde bei Raumtemperatur in eine funktionale Aminogruppe umgewandelt. Die Oberfläche wurde wieder in Wasser gewaschen und getrocknet, bevor Pränisin durch Zugabe von 10 µM geschütztem Pränisin und 10 mM EDC gelöst in 100 mM MES, pH 4,7 eine Stunde bei Raumtemperatur gebunden wurde.

Nach erneutem Waschen in Wasser wurde Pränisin im letzten Schritt mit einer 95 % TFA Lösung entschützt. Die Oberflächen wurden erneut gewaschen und direkt in Puffer vermessen.

7.1.4 Labeln von Pränisin mit alexa488 über einen PEG-Linker

Im ersten Schritt wird alexa488-Cadaverin (Invitrogen) an den PEG-Linker gekoppelt. Im Gegensatz zu den Oberflächenpräparationen wurde hierzu geschütztes NHS-PEG-NH(Boc) (MW 6000) verwendet. Die Reaktion von 300 mM alexa488-NH_2 mit 300 mM NHS-PEG-NH(Boc) erfolgte in 1 ml wasserfreiem Chloroform (ChromosolvV) für eine Stunde bei Raumtemperatur. Anschließend wurde das Chloroform im Ofen verdampft und die Schutzgruppe vom PEG durch Gabe einiger Tropfen 95%iger TFA-Lösung abgespalten. Überschüssiges alexa488 wurde über Größenausschlusschromatographie in 100 mM MES, pH 4.7 (HiPrep 26/10, GE Healthcare) abgetrennt. Fraktionen mit alexa488-PEG waren durch ihre Farbe erkennbar und wurden mit Amicons (Millipore, Cut-off 3 kDa) aufkonzentriert. Aufgereinigtes alexa488-PEG-NH_2 wurde im fünffachen Überschuss mit 200 µM geschütztem Pränisin unter Aktivierung von 10 mM EDC in 100 mM MES, pH 4,7 inkubiert um Pränisin zu koppeln. Die Schutzgruppe des Pränisins wurde wiederum mit TFA abgespalten und das Konstrukt wurde über Größenauschlusschromatographie (HiPrep 26/10, GE Healthcare) von überschüssigem Pränisin getrennt und in 20 mM HEPES, 150 mM NaCl, pH 6.5 gepuffert. Die Fraktionen waren durch ihre Farbe erkennbar und wurden mit Amicons (Millipore, Cut-off 3 kDa) aufkonzentriert.

7.1.5 Anbinden NisT

Nach der Ernte wurden die Bakterien in Messpuffer (HBS: 20 mM HEPES, 150 mM NaCl, pH 6.5) homogenisiert, so dass Aliquots von Proben mit Vesikeln mit einem Proteinanteil mit einer Endkonzentration von 5 mg/ml schockgefroren und bei -80 °C gelagert wurden.
Zur Präparation der Proben wurden Deckgläser in Hellmanex und Wasser im Ultraschall gewaschen und die Oberfläche durch Einwirken von konzentrierter GOPTS- Lösung (ABCR) für 15 Minuten bei 75 °C funktionalisiert. Danach wurden die Gläser in wasserfreiem Chloroform gewaschen und im Stickstoffstrom getrocknet. Die Vesikel wurden unmittelbar vor der Anbindung aufgetaut und mit 0.2 µl DiD (cell labeling solution, Invitrogen) pro 20 µl Aliquot gefärbt. Danach wurden sie für 5 Minuten auf den

funktionalisierten Gläsern inkubiert. Die angebundenen Vesikel wurden mehrmals in HBS gewaschen, bevor sie direkt vermessen wurden.

7.1.6 Kontrollmessung zum Binden von modifiziertem Pränisin an NisT

Die Proben wurden fluoreszent markiert und mit einem invertierten Mikroskop (Olympus IX71, Hamburg, Germany) und einer Peltier gekühlten ECCD camera (Andor IXON, 512x512 pixels, Belfast, Ireland) gemessen. Die Fluoreszenz wurde durch das Anstrahlen mit einer 150 W Xenon-Lampe induziert, bei der ein spezielles Filterset entsprechend der gemessenen Fluorophore verwendet wurde (AHF, Tübingen, Germany) (F41-054 für alexa488, F41-008 für DiD). Die Aufnahmen wurden über 10 Bilder akkumuliert, die je eine Sekunde mit einem Gain von 100 aufgenommen wurden.
Nachdem die markierten Vesikel erst ohne Zugabe von gelabeltem Pränisin in gefiltertem HBS gemessen wurden und auch die Fluoreszenz im Blaulicht kontrolliert wurde, wurde für wenige Minuten gelabeltes Pränisin auf die Probe gegeben, danach gründlich gespült und die Fluoreszenz erneut gemessen.

7.1.7 Kraftmessungen von Pränisin an NisT Vesikeln

Um die Spitze über einem Vesikel zu positionieren wurden die Position der Spitze und des zu untersuchenden angefärbten Vesikels unter Anwendung der Fluoreszenzmessung im Rotlicht bestimmt. Um eine genaue Positionierung zu erreichen, wurde der zu untersuchende Vesikel mit dem AFM Scanner mit Hilfe einer von Frau Dr. Olga Franco in IGOR geschriebenen Software unter der AFM Spitze platziert. Kraftmessungen wurden mit einem AFM MFP-3D von Asylum durchgeführt. Dazu wurde die funktionalisierte Spitze (größter Cantilever der veeco-MLCT Chips) mit einer Geschwindigkeit von 1000 nm/s von der Probe entfernt und die Deflection mit einer Rate von 33.333 Hz gemessen. Pro Experiment wurden 1000 Kraftkurven aufgenommen; anschließend wurde die Position des Vesikels durch ein AFM Image kontrolliert. Die Kraftkonstante der Spitze wurde über das Equipartitionstheorem bestimmt. Die Auswertung erfolgte mit selbst geschrieben Prozeduren in IGOR.

7.2 Ergebnisse

7.2.1 Kopplung Pränisin

Die Anbindung von aufgereinigtem Pränisin über einen PEG Linker wurde ausgehend von Janissen et al., 2008 weiter entwickelt. In der Literatur ist beschrieben, dass sich die PEGylierung von Nisin als schwierig erweist (Guiotto et al., 2003). Demzufolge ist die Anbindung von PEG-Hz (PEG-Hydrazin) an die terminale Carboxylgruppe von Nisin nicht möglich, wohingegen die Kopplung von PEG-SPA, einem aktivierten Ester, an die Aminogruppen der Lysine zwar möglich ist, das Peptid aber inaktiviert.

Da die Präsequenz zugänglich für NisT bleiben soll, wurde hier versucht, die Carboxygruppe zu PEGylieren. Anstatt Hydrazin als funktionelle Gruppe zu verwenden, wurde Amino-PEG eingesetzt, dass die Carboxygruppe unter sterischer Sicht leichter angreifen kann. Um zu vermeiden, dass sich das Pränisin durch Ringkopplungen zwischen den Amino-Seitengruppen und der aktivierten terminalen Carboxygruppe aggregiert, wurden die Amino-Seitengruppen in einem ersten Schritt Boc-geschützt. Der C-Terminus des Boc-geschützten Peptides wurde mit EDC aktiviert, so dass es mit der Aminogruppe des PEG reagieren konnte.

Die Bindung von Pränisin an PEG wurde auf PEGylierten Glasoberflächen getestet, indem erst ein für die Präsequenz spezifischer Antikörper gebunden wurde, der wiederum durch einen fluoreszenzmarkierten Zweitantikörper nachgewiesen wurde. Der Vergleich der Proben mit entsprechenden Negativ-Kontrollen zeigt, dass die Anbindungsstrategie erfolgreich ist (Abb. 7). Mithilfe der gleichen Kopplungsstrategie sollte die Leadersequenz von Pränisin auch über einen PEG-Linker an alexa488-Cadaverin gebunden werden. Das Binden des gelabelten Pränisin-PEG-alexa488 Konstrukts an inside-out Vesikel mit NisT dient als Nachweis, dass die Präsequenz des Konstrukts immer noch aktiv ist.

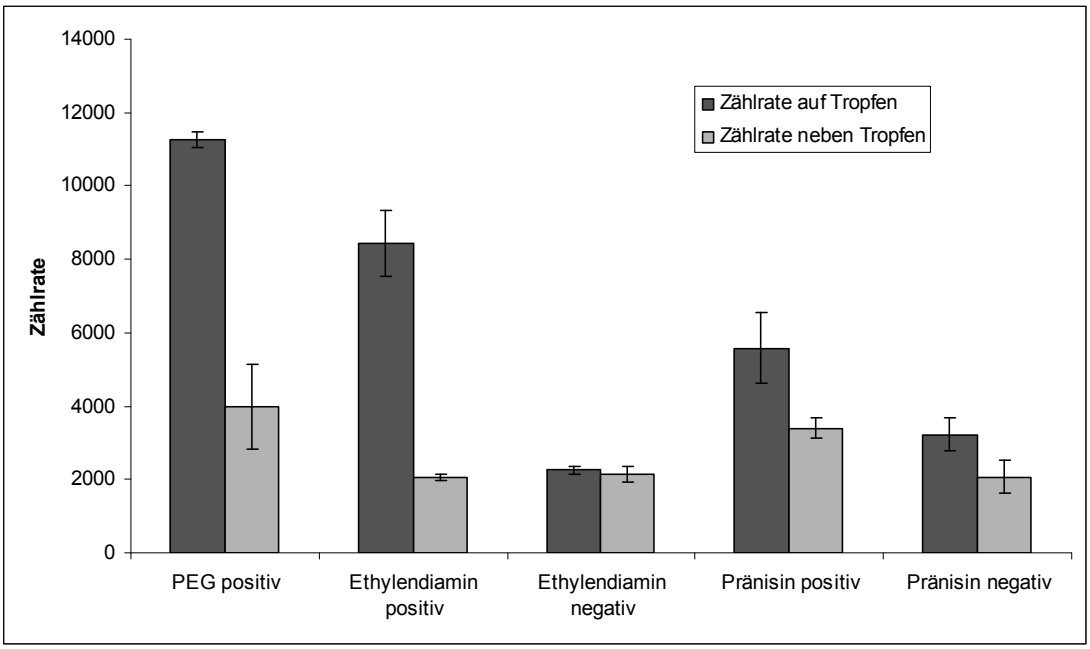

Abbildung 7: Anbindung von Pränisin über einen PEG-Linker an Glasoberflächen.

Schwarze Balken zeigen die mittleren Counts von fluoreszenzmarkierten Spots (positiv), grau sind die entsprechenden Hintergrundwerte, die neben dem Probenspot gemessen wurden (gemessen mit 40x Objektiv, ANDOR). PEG positiv: Anbindung von NH_2-PEG-COOH mit anschließender Kopplung von alexa488-Cadaverin. Ethylendiamin positiv: Test der Aminogruppe des PEGs, die durch Umwandlung der Carboxygruppe nach Reaktion mit Ethylendiamin entsteht, getestet durch Anbinden von alexa-COOH. Ethylendiamin negativ: Negativ Test des Bindens von alexa-COOH an PEG-COOH. Pränisin positiv: Fluoreszenz des alexa488 gelabelten Sekundärantikörpers der an den anti-leader Antikörper gebunden ist, um die Kopplung von Pränisin nachzuweisen. Pränisin negativ: Fluoreszenz des alexa488 gelabelten Sekundärantikörpers, der auf Probe mit anti-leader Antikörper ist, aber auf der kein Pränisin angebunden ist.

Hierzu wurde im ersten Schritt alexa488-Cadaverin an NH_2-PEG-NH(Boc) gekoppelt und mittels Größenausschlusschromatographie aufgereinigt. Nach Aufkonzentrieren der entsprechenden Fraktionen wurde die Schutzgruppe mittels TFA entfernt und geschütztes Pränisin unter Zugabe von EDC entweder in MES oder in Chloroform gebunden. Weiteres Aufreinigen des Konstrukts mittels Größenausschlusschromatographie entfernt ungelabeltes Pränisin aus der Probe, trennt aber reagiertes PEG aufgrund seines großen hydrodynamischen Radius nicht ab (Abb. 8). Auch ist nur PEG-alexa488, nicht aber ungebundenes PEG über seine Absorption sichtbar.

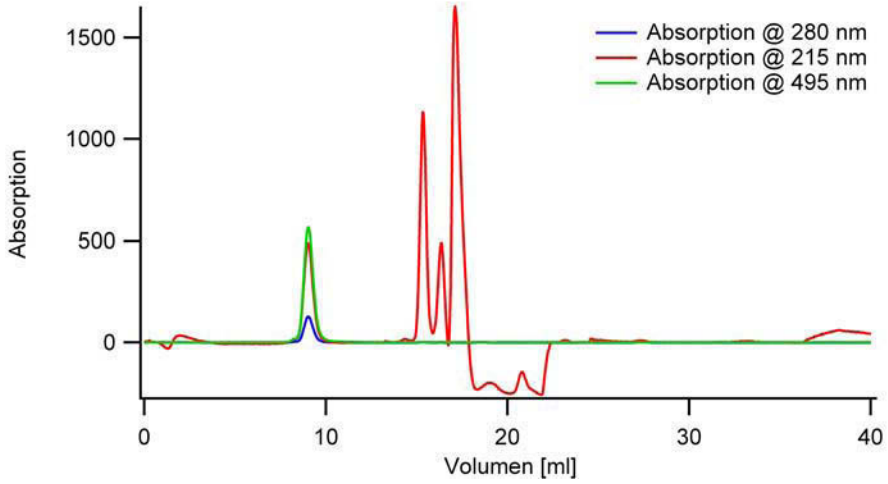

Abbildung 8: Elutionsprofil der Größenausschlusschromatographie des alexa488-PEG-Pränisin Konstrukts

Bei 280 nm ist geringe Proteinabsorption und Absorption von alexa 488 zu sehen, bei 215 nm absorbiert die Peptidbindung und alexa488, bei 495 absorbiert alexa488. Das Elutionsprofil zeigt drei Peaks von ungelabelten Pränisin zwischen 15 und 20 ml, die wahrscheinlich von geschütztem, ungeschützten und aggregierten Pränisin stammen, sowie einen Peak nach 9 ml, der entweder vom PEG-alexa488 Konstrukt, dem Pränisin-PEG-alexa488 Konstrukt oder einer Mischung aus beidem stammt.

Weiteres Aufreinigen des Konstrukts über einen 10-90 % Acetonitril/Wasser-Gradienten mittels HPLC trennt die Probe in zwei Peaks, deren Inhalt aber nicht mittels Massenspektrometrie bestimmt werden kann, da der Anteil an PEG in beiden Proben so hoch ist, dass sein Signal alle weiteren Signale überdeckt.

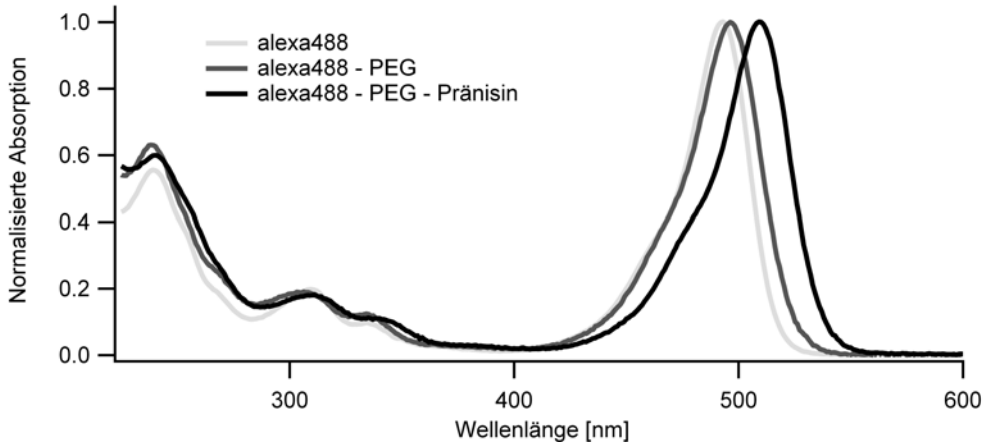

Abbildung 9: Normierte Absorptionsspektren von alexa488, alexa488-PEG und alexa488-PEG-Pränisin.

Bei 215 nm lässt sich die Konzentration der jeweiligen Konstrukte nicht bestimmen, da der im Puffer gelöste Sauerstoff interferiert. Es ist aber ein Shift des Absorptionsmaximums des alexa488-PEG-Pränisin Konstrukts zu erkennen.

Da die Menge an Pränisin nur durch die Peptidbindung bei 215 nm messbar ist, ist es nicht möglich den Anteil an alexa-PEG-Pränisin im Absorbtionsspektrum zu bestimmen. In diesem Bereich ist die Messung aufgrund der störenden Sauerstoffabsorption quantitativ sehr ungenau, so dass der Unterschied zu der im Vergleich zu alexa488 gemessenen Absorption nicht groß genug ist, um den Anteil an gelabeltem Pränisin zu bestimmen. Allerdings zeigt sich eine Verschiebung des Absorptionsmaximums von alexa488 von 495 nm im Konstrukt ohne Pränisin zu 510 nm im alexa488-PEG-Pränisin Konstrukt (Abb. 9), was ein Hinweis für eine erfolgreiche Kopplung sein könnte.

7.2.2 Anbinden NisT und Kontrollmessung zum Binden von modifiziertem Pränisin an NisT

Die Zellen wurden abzentrifugiert und im Messpuffer homogenisisert, wodurch ein Probengemisch aus Membranpatchen, Vesikeln und inside-out Vesikeln entstand. Die Membran der Vesikel besteht neben den natürlichen Proteinen des Bakteriums aus überexprimiertem NisT. Ein Vergleich der Anbindung der Vesikel über die Amino-Seitengruppen der Membranproteine zeigte, dass mit einer Anbindung an eine GOPTS funktionalisierte Oberfläche bessere Oberflächen erhalten wurden als mit einer Anbindung über Oberflächen mit Carboxy-PEG(MW 35000) oder Carboxy-PEG(MW3000). Um die Vesikel auf der Oberfläche zu lokalisieren, werden sie mit DiD gefärbt, wodurch sie bei Fluoreszenzmessungen als nur wenige Pixel große Spots sichtbar sind. DiD ist ein Farbstoff, der sich in die Membran setzt und im Rotlicht absorbiert. Dieser Farbstoff hat den Vorteil, dass er im gleichen Spektrum zu erkennen ist wie die AFM-Spitze, was für die kombinierte Messung mit dem AFM und der Fluoreszenz unabdingbar ist.
Um die Anbindung der Vesikel und die Funktionalität von NisT an PEGyliertem Pränisin zu überprüfen, wurde die Anwesenheit der Vesikel über Fluoreszenz im Rotlicht, die vom DiD herrührt, gemessen (Abb. 10A). Es wurde überprüft, dass bei Absorption im Blaulicht keine Fluoreszenz messbar war, bevor das alexa488-PEG-Pränisin Konstrukt hinzugegeben wurde. Nach Spülen der Oberfläche war nun auch Fluoreszenz im Blaulicht zu sehen, wenn auch weniger Spots auszumachen waren als im Rotlicht (Abb. 10B). Das deutet darauf hin, dass das Pränisin nur an das NisT der inside-out Vesikel gebunden hat. Wiederholt man das Experiment in Anwesenheit von ATP und Mg^{2+}, zeigt sich auch hier eine Bindung von fluoreszenzmarkiertem Pränisin (Abb. 10C). Die Negativ-Kontrollen schließen unspezifisches Binden des PEG-alexa488 Konstrukts an NisT Vesikel (Abb.

10D) und unspezifisches Binden des alexa488-PEG-Pränisin Konstrukts an die Vesikel ohne NisT (Abb. 10E) aus.

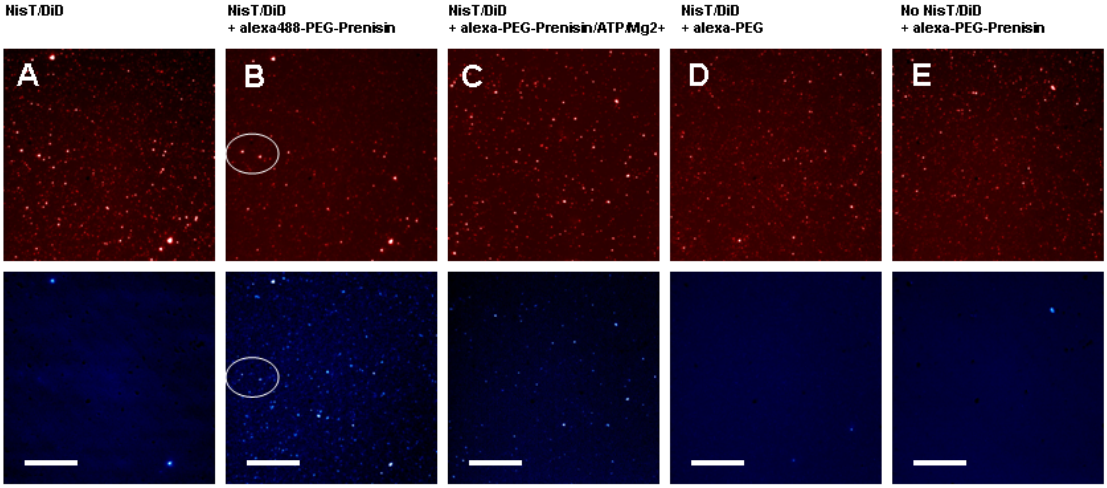

Abbildung 10: Kontrollmessungen zum Binden von PEG-Pränisin an NisT Vesikel.

Rote Bilder zeigen die Fluoreszenz von Vesikeln durch DiD, blaue Bilder zeigen die Fluoreszenz von alexa488, was über einen PEG Linker an Pränisin gebunden ist. **A**. Der Vergleich von Fluoreszenz bei Rotlicht und Blaulicht der DiD gefärbten Vesikel zeigt nur ihre Fluoreszenz im Rotlicht, die beiden Spots im Blaulicht sind Verunreinigungen und dienen zur Orientierung. **B**. Nach Zugabe von alexa488-PEG-Pränisin zur gleichen Probe wie A und gründlichem Waschen ist auch deutlich Fluoreszenz im Blaulicht zu erkennen, obwohl kein ATP/Mg^{2+} im Puffer war. **C**. Gleiches gilt, wenn ATP/Mg^{2+} im Puffer enthalten ist. **D**. und **E.** Die Negativ Kontrollen ohne Pränisin (**D**) bzw. ohne NisT in den Vesikeln (**E**) zeigt kein Binden von fluoreszenzmarkiertem Pränisin. Die Bilder wurden aufgenommen mit einer ANDOR-CCD Kamera, 60x Objektiv, Aufnahme akkumuliert über 10 Bilder, Belichtungszeit 1 s, gain 100, der Balken zeigt eine Länge von 200 µm.

Um nachzuweisen, dass die Fluoreszenzspots von Vesikeln herrühren, wurden sie mithilfe einer von Frau Dr. Olga Franco entwickelten Software unter der AFM Spitze positioniert und abgebildet (Abb. 11). Die Positionierung erfolgt durch die Berechnung des Intensitätspeaks der Pixel im Bereich weniger Nanometer genau und das AFM-Bild zeigt einen Vesikel von etwa 500 nm x 300 nm Breite und einer Höhe von etwa 120 nm. Die Größe des Vesikels ist demnach ausreichend groß um die Ungenauigkeit der Positionierung auszugleichen.

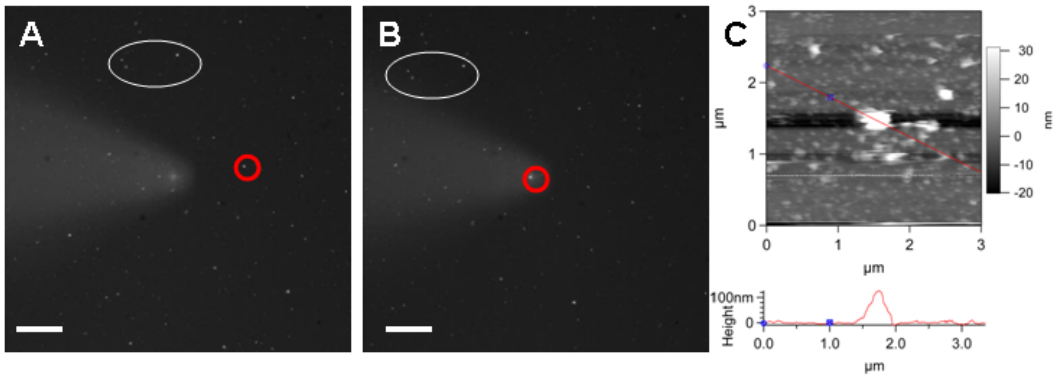

Abbildung 11: Abbilden zur Kontrolle DiD markierter Vesikel mit dem AFM

A. Fluoreszenzbild der AFM Spitze und der Probe mit NisT Vesikeln. Die Spitze ist deutlich zu erkennen, der anvisierte Vesikel ist durch einen roten Kreis markiert. Die Vesikel, die durch ein weißes Oval gekennzeichnet sind, dienen der Orientierung. Der Balken zeigt eine Länge von 100 µm. **B**. Das gleiche Bild, nachdem der ausgewählte Vesikel unter der AFM Spitze positioniert wurde. **C**. AFM-Bild des Vesikels über einen 3 x 3 µm großen Ausschnitt. Der ausgewählte Vesikel befindet sich in der Mitte und besitzt eine Größe von etwa 500 nm x 300 nm Breite und eine Höhe von etwa 120 nm. Daneben liegen Membranpatches auf der Glasoberfläche, die als Erhebungen zu erkennen sind.

7.2.3 Kraftspektroskopie zur Messung der Pränisin- NisT- Interaktion

Die beschriebenen Vorexperimente erlauben nun Kraftmessungen, in denen die Kraft gemessen wird, mit der Pränisin und NisT auf inside-out Vesikeln interagieren. Hierzu wird Pränisin, das über einen PEG-Linker mit der Spitze verbunden ist, an ein Vesikel, der NisT enthält, positioniert. Beim Aufnehmen der Kraftkurven wird darauf geachtet, dass die Kraft, mit der die Spitze auf die Probe drückt, minimal ist um unspezifische Wechselwirkungen zu vermeiden. Um eine Interaktion zwischen NisT und Pränisin zu ermöglichen, wird die Spitze mit einer Kraft von etwa 50 pN auf das Vesikel gedrückt, was der doppelten Kraft des Rauschens entspricht. Für die Messung der Interaktion zwischen Pränisin und NisT wird erwartet, dass in den Kraftkurven die Dehnung von PEG zu erkennen ist, und ein Kraftabriss zu sehen ist, wenn die Bindung zwischen NisT und Pränisin bricht. Dementsprechend werden die Kurven selektiert, die exakt mit dem PEG-Modell übereinstimmen (Abb. 12A). Dies ist in den Experimenten mit Pränisin und NisT unabhängig von der Anwesenheit von ATP in etwa 3 % der Kurven der Fall und entspricht damit etwa 10-30 % aller Kurven, in denen Abrisse gemessen wurden. Die anderen Kurven zeigen drei verschiedene Muster, die sich auch in den Negativ-Experimenten ohne NisT oder mit unmodifizierter Spitze wieder finden lassen.

Negativ-Kontrollen, die mit einer unmodifizierten Spitze ohne PEG-Pränisin durchgeführt wurden, zeigen, dass die Spitze bei 1 % der Kurven mit dem Vesikel interagiert (Abb. 12B). Diese Kurven zeigen eine charakteristische Form, die die Dehnung des Vesikels beschreibt. In weiteren Negativ-Kontrollen, in denen die Wechselwirkung zwischen der PEG-Pränisin modifizierten Spitze und Vesikeln ohne NisT gemessen wurden, zeigen sich zwei weitere charakteristische Muster in den Kraftkurven, die durch unspezifische Wechselwirkungen mit PEG oder Pränisin und den Vesikeln entstehen (Abb. 12C, D). Allerdings zeigen auch Kurven aus dieser Messung typische Abrisskurven, die das Dehnen von einem PEG beschreiben, mit der gleichen Häufigkeit wie in Messungen auf NisT Vesikeln.

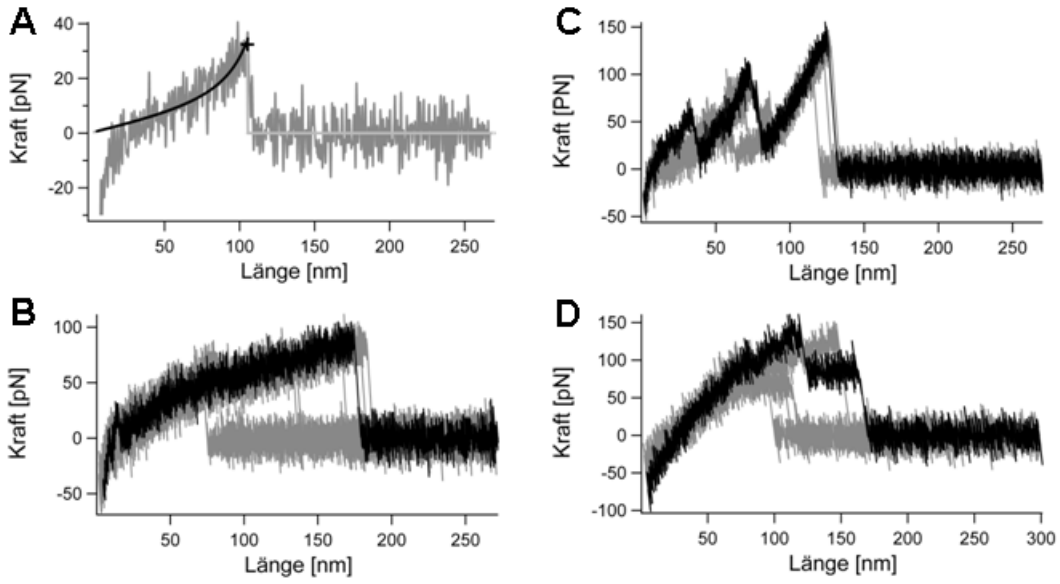

Abbildung 12: Beispielkurven, die typische unspezifische Wechselwirkungen zwischen den Vesikeln und der Spitze zeigen.

A. Kraft-Abstandskurve einer spezifischen Interaktion, die die sich mit der Dehnungskurve von PEG beschreiben lässt **B**. Beispiel für eine typische Interaktion zwischen der Spitze und den Vesikeln. **C**. und **D**. Beispielkurven mit typischem Muster für unspezifisches Binden von PEG an die Vesikel.

Ein Vergleich der Histogramme über die Verteilung der gefitteten Kräfte und Monomerlängen zeigt aber einen Unterschied zwischen den Positiv-Experimenten und den Experimenten ohne NisT (Abb. 13). In vier von fünf Experimenten mit Pränisin und NisT zeigt sich in Anwesenheit von ATP eine klare Kraftverteilung um 27 pN mit einer Peakbreite von 9 pN; ähnliches gilt für die Messungen in Abwesenheit von ATP mit einer Kraftverteilung von 29 pN und einer Peakbreite von 10 pN in drei von sechs

Experimenten. Die anderen Experimente zeigen eine Kraftverteilung, die der der Negativ-Messung von Pränisin mit Vesikeln ohne NisT gleicht. Hier sind die Kräfte mit einem Peak von 48 pN und einer Breite von 24 pN deutlich höher und breiter verteilt.

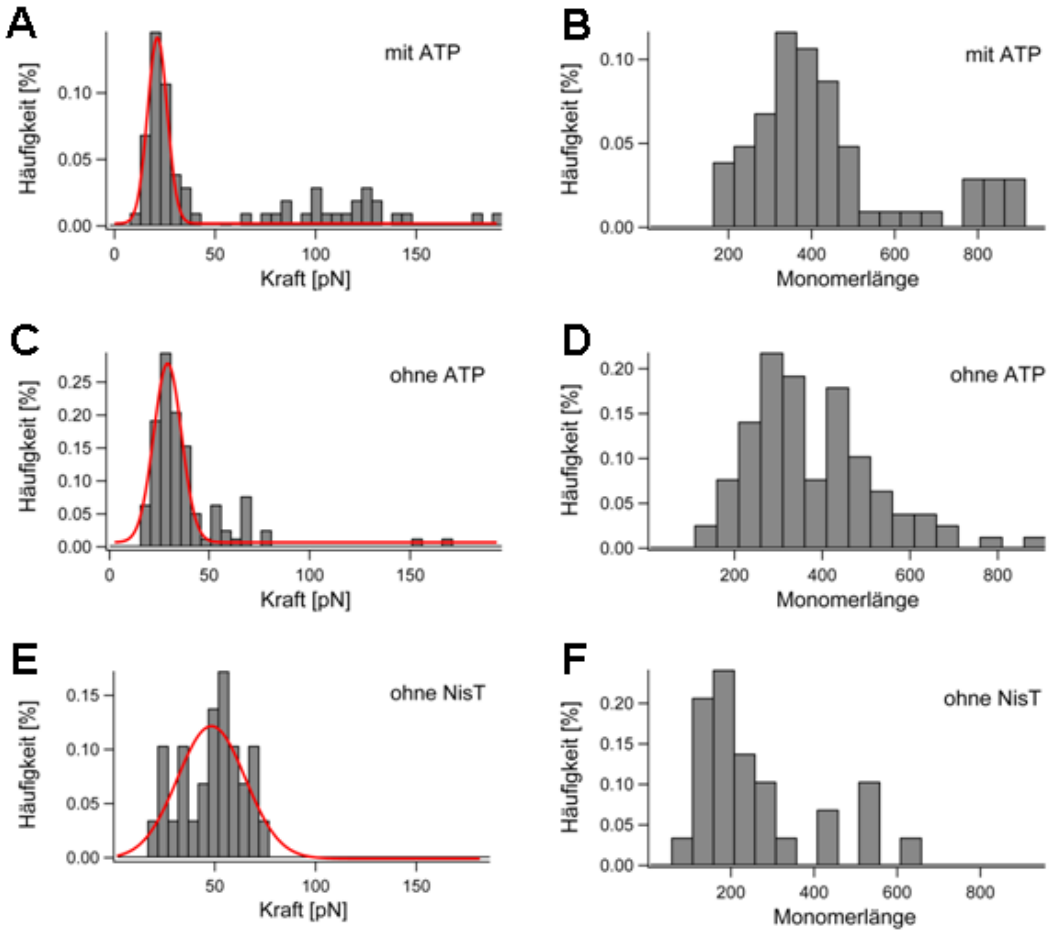

Abbildung 13: Vergleich der Verteilung der Kräfte und Monomerlänge der Kraft-Abstandskurven der NisT – Pränisin Experimente.

Histogramme zeigen die normalisierte Häufigkeit der Abrisskräfte und Monomerverteilung der über das Muster der Dehnung von PEG selektierten Kurven. **A, B** : Histogramme der Messung der Interaktion zwischen Pränisin und NisT in Überschuss an ATP; **C, D** : Histogramme der Messung der Interaktion zwischen Pränisin und NisT in Abwesenheit von ATP; **E, F**: Negativ-Kontrolle der Messung mit Vesikeln ohne NisT. Der Gaußfit der Kräfte (rot) gibt das jeweilige Maximum und die Breite der Verteilung an.

Neben dem Vergleich der Kraftverteilung zeigt auch ein Vergleich der Verteilung der Monomerlänge einen deutlichen Unterschied zwischen Messungen mit Pränisin und NisT und der Negativ-Kontrolle ohne NisT. In ersteren werden PEG-Moleküle gedehnt, die aus 200 bis 400 Einheiten bestehen, während in den Messungen ohne NisT deutlich kürzere Polymere gedehnt werden. Die Breite der Verteilung erklärt sich zum einen dadurch, dass

die Polymere an verschiedenen Stellen der Spitze gebunden sein können und zum anderen, dass die Ausgangspolymere bedingt durch die Produktion nicht alle gleich lang sind.
Da Pränisin über PEG mit einem Molekulargewicht von 6000 g/mol an die Spitze gebunden wurde, sollte für die Kraft-Abstandskurven eine Monomerlänge von 150 erwartet werden. Die Abweichung zu den gemessenen Werten kann dadurch entstehen, dass auch die Vesikel der Kraft nachgeben, was zum einen den Weg der Ausdehnung verlängert und zum anderen den PEG-Fit beeinflusst. Dieser ist im Bereich kleiner Kräfte flach, so dass kleine Abweichungen leicht zu einer Änderung der Einschätzung der Monomerlänge führen können.

7.3 Diskussion

Zur Produktion von aktivem Nisin wird in der Zelle ein inaktives Präpeptid hergestellt, was erst verschiedene Modifikationsschritte wie Dehydrierung und Zyklisierung durchläuft, bevor es durch NisT aus der Zelle transportiert und erst durch Abtrennen der Leader-Sequenz aktiviert wird. NisT ist ein ABC-Exporter, der die Leadersequenz erkennt und durch die Membran transportiert (Kuipers et al., 2004). In diesem Kapitel ist die Interaktion zwischen Pränisin und NisT durch Fluoreszenzmessungen und Kraftspektroskopie untersucht worden, indem Pränisin über einen Linker entweder fluoreszenzmarkiert oder an die AFM-Spitze gebunden wurde.
Zuerst wurde Pränisin über sein Carboxy-terminales Ende an den PEG-Linker gebunden, was an funktionalisierten Oberflächen mit fluoreszenzmarkierten Antikörpern gegen die Leader-Sequenz nachgewiesen wurde. Um zu zeigen, dass NisT auch an das mit dem PEG-Linker modifizierte Pränisin bindet, wurden Fluoreszenzmessungen mit alexa488 gelabeltem Pränisin durchgeführt. Hier ist der Nachweis über ein erfolgreiches Labeln schwieriger, da die Eigenschaften von PEG die meisten gängigen biochemischen Analysemethoden beeinträchtigt. Die Änderung des Absorptionsspektrums von alexa488 ist aber ein indirekter Nachweis der Kopplung des Farbstoffs an das Pränisin-PEG Konstrukt.
Vesikel, die überexprimiertes NisT enthalten, lassen sich durch DiD anfärben, wodurch ihre Anbindung an die Oberfläche nachgewiesen werden kann. Ein Vergleich der Fluoreszenz von mit DiD angefärbten Vesikeln, die im Roten absorbieren, und mit alexa488 gelabeltem PEG-Pränisin, die im Blauen absorbieren, zeigt, dass Pränisin an vielen Vesikeln bindet. Negativ-Kontrollen mit Vesikeln ohne NisT schließen

unspezifisches Binden des gelabelten Pränisins an Vesikel aus, während Messungen des PEG-alexa488 Konstrukts ohne Pränisin zeigen, dass kein unspezifisches Binden von PEG oder alexa488 an die Vesikel messbar ist.

Da die Vesikel durch Homogenisieren der Membran hergestellt werden, bedeutet dies, dass sich in der Probe nicht nur die gewünschten inside-out Vesikel befinden, sondern auch Membranpatches und Vesikel, in denen NisT nach innen orientiert ist. Demnach ist es erwartungsgemäß, dass das Binden von gelabeltem Pränisin nicht bei allen Vesikeln zu sehen ist.

Die Fluoreszenzmessungen zeigen außerdem, dass Pränisin-PEG-alexa488 bei einem Überschuss an ATP und Mg^{2+} im Puffer deutlich schlechter bindet, als in Abwesenheit des Nukleotids. Gemäß dem „ATP switch Modell“ (Higgins and Linton, 2004), was die heutigen Erkenntnisse der Funktion von ABC-Transportern zusammenfasst und für Importer sowie Exporter gilt, durchläuft der ABC-Transporter während des Mechanismus verschiedene Konformationen. Im Ausgangszustand haben die NBDs kein ATP gebunden und die Bindungsstelle für das Transportmolekül besitzt eine hohe Affinität. Binden von ATP führt zur Dimerisierung der NBDs, die eine strukturelle Änderung der Transmembrandomäne induziert und die Bindungsaffinität zum Transportmolekül ändert. Durch die Hydrolyse von ATP kehrt der Transporter in seinen Ausgangszustand zurück und der Dimer zerfällt. Demnach liegt die Bindungsstelle für Pränisin in Abwesenheit von ATP frei und es kann mit hoher Affinität binden. Im Gegensatz dazu führt die hohe Konzentration an ATP in der Probe dazu, dass die meisten Transporter in der ATP-gebundenen Konformation vorliegen, bei der die Bindungsstelle für Pränisin eine deutlich niedrigere Affinität hat.

Die Ergebnisse der Kraftspektroskopie deuten ebenfalls auf spezifisches Binden von Pränisin an NisT hin. In mehreren Experimenten, in denen die Bindung von Pränisin an NisT gemessen wurde, zeigte sich eine spezifische Kraftverteilung der Kurven, die entsprechend ihrem Muster einer PEG-Dehnungskurve selektiert wurden, die nicht bei der Messung zu sehen war, in der die Vesikel kein NisT hatten. Auch hier zeigen manche Experimente mit NisT und Pränisin in der Probe eine ähnliche Kraft- und Monomerverteilung wie die Negativ-Probe. Dies ist erwartungsgemäß, da die Probe nicht nur aus inside-out Vesikeln besteht. Allerdings zeigen die Kraftmessungen keinen Unterschied der Kraftverteilung in Abhängigkeit von ATP. Auch wenn die Kraft bei den Messungen mit ATP etwas geringer ist, liegt dieser Unterschied im Bereich statistischer Ungenauigkeit und kann somit nicht die Ergebnisse der Fluoreszenz unterstützen. Da es

sich bei der Kraftspektroskopie um Einzelmolekülmessung handelt, ist es möglich, dass Pränisin beim Annähern der Spitze genug Zeit hatte die Bindungsstelle mit höherer Affinität zu finden. Die Affinität zur anderen Bindungsstelle könnte auch so niedrig sein, dass die Kräfte zu gering sind, um sie mit dieser Methode aufzunehmen oder die Affinitäten unterscheiden sich nicht genug, um mit der bisher geringen Statistik aufgelöst zu werden. Wie in Kapitel 5 beschrieben kann auch Multivalenz der Bindung einen Einfluss auf den Unterschied ihrer Beschreibung durch die Kraftverteilung und die Fluoreszenzmessung auf der Oberfläche haben.

In der Literatur wird die Möglichkeit von ein, zwei oder mehr Bindungsstellen des ABC-Transporters für das Transportmolekül diskutiert, die unterschiedliche Affinität besitzen können (Biemans-Oldehinkel and Poolman, 2003; Schuurman-Wolters and Poolman, 2005; van Veen et al., 2000; Senior et al., 1995; Urbatsch et al., 2003). Die hier gezeigte Kraftverteilung besitzt nur einen Peak, was der Bindung mit nur einer Affinität entsprechen würde. Allerdings lassen sich Bindungen mit anderer Affinität aus den oben diskutierten Gründen nicht ausschließen. Eine Untersuchung der Ratenabhängigkeit sollte es erlauben, die Energiepotentiale besser abschätzen zu können. Sollte es Bindungsstellen mit verschiedenen Affinitäten geben, würden sich diese durch einen Unterschied der Ratenabhängigkeit identifizieren lassen. Auch würden schnellere Ziehgeschwindigkeiten bedingt durch die Ratenabhängigkeit zu höheren Kräften führen, so dass zwei Peaks besser aufgelöst werden könnten. Mit einer besseren Statistik können auch die Dissoziationsraten über die in Kapitel 2 beschriebene Methode berechnet werden. Um eventuelle Zwischenschritte beim Auseinanderziehen der Pränisin – NisT Interaktion zu sehen, die Rückschlüsse auf Zwischenschritte des Transportmechanismus zulassen würden, ist das Rauschen in den Kraftkurven zu groß. Solche Fragen müssten durch eine Optimierung und Stabilisierung des Systems, wie etwa das Einführen von Rückkopplungsmechanismen oder einer kontrolliert oszillierenden Spitze, adressiert werden.

Die bisherige Arbeit zeigt, dass Pränisin an NisT bindet, auch wenn es an einen PEG-Linker gebunden ist. Diese Bindung lässt sich sowohl mit Fluoreszenz als auch durch Kraftspektroskopie nachweisen, was eine gute Ausgangsposition bietet, die Interaktion des Transportmoleküls mit dem ABC-Exporter im Detail zu untersuchen.

8 Zusammenfassung

Membranproteine spielen eine wichtige Rolle zur Aufrechterhaltung vieler essentieller Bedingungen in der Zelle und ihre Struktur-Funktionsbeziehungen sind von großem Interesse um ihre Wirkungsweise zu verstehen. Mittels Rasterkraftspektroskopie lassen sich sowohl die inter- und intramolekularen Kräfte eines Proteins in der Membran, als auch die Bindungsraten von Rezeptor – Ligand Interaktionen bestimmen, so dass sie sich als geeignete Technik erweist, die gängigen strukturbiologischen Untersuchungen zu ergänzen.

Im ersten Teil dieser Arbeit wurde durch Entfaltungsexperimente an Sensorhodopsin II der Einfluss von Lichtaktivierung und Komplexbildung auf seine inter- und intramolekularen Kräfte untersucht. Hierzu wurde die Analysemethode zur Bestimmung der Stabilität einer Bindung oder Proteinregion weiter entwickelt. Ein Ansatz ist es, die Durchschnittskraft der Stabilität einer Proteinregion anzugeben, indem die Daten der Einzelmolekülmessung als Ensemble-Messung betrachtet werden. In einem anderen Ansatz wurde die Stabilität einer Proteinregion über die Abrisshäufigkeit einer Bindung in dieser Region bestimmt und die Auflösung der Histogramme erhöht. Beide Ansätze identifizieren Regionen, in denen sich die Stabilität in Abhängigkeit von Lichtaktivierung und Komplexbildung ändert, was dazu beiträgt, den Reaktionsmechanismus besser zu verstehen.

Um den Einfluss der Kraft auf das Energiepotential der Bindung zu berücksichtigen, wurde eine Analysemethode entwickelt, bei der die Dissoziationskonstante aus dem Verhältnis der Anzahl der Datenpunkte bei einer bestimmten Kraft zu der Anzahl der Abrisse bei dieser Kraft bestimmt werden kann.

Im zweiten Teil der Arbeit wurden Rezeptor – Ligand Interaktionen gemessen, für die die Interaktionspartner gezielt an die Oberfläche gebunden wurden, um eine kontrollierte Interaktion zu messen. Zum einen wurde der Einfluss der Multivalenz auf den Ni-NTA-Histag Komplex untersucht. Der Vergleich des Tris-NTA/His6 Systems mit dem Mono-NTA/His2 System zeigt, dass die Affinität mit zunehmender Multivalenz deutlich ansteigt, aber die mechanische Stabilität beider Systeme gleich bleibt. Dies lässt sich auf die Geometrie des Komplexes zurückführen und trägt damit zum Verständnis multivalenter Bindungen bei. Des Weiteren wurde die Interaktion des Präpeptids des Lantibiotikums Nisin mit dem ABC-Exporter NisT, der Bestandteil der Modifizierungsmaschinerie zur Produktion von Nisin ist, untersucht. Fluoreszenzmessungen sowie Kraftspektroskopie zeigen spezifisches Binden des Präpeptids und erlauben somit Einblicke in die Interaktion.

9 Summary

Inside the cell membrane proteins play a crucial role to keep up many essential conditions and thus, the investigation of their structure-function relationship is of great interest to understand their mechanism. Atomic force spectroscopy proves to be a suitable technique to complement other established methods in structural biology, as it not only determines inter- and intramolecular forces of a protein but also binding kinetics of receptor – ligand interactions.

In the first part of this work the influence of light activation and complex formation on the inter- and intramolecular forces of sensory rhodopsin II has been investigated by unfolding experiments and the analysis to determine the stability of a protein region has been improved. In one approach, the stability is given as average fore derived by treating the data form single molecule measurements as if they were derived from ensemble measurements. In another approach the stability of a protein region was determined by the frequency of rupture events in the respective region. Also, the resolution of the histograms was increased.

In both approaches regions are identified, in which light activation and complex formation induce changes in stability, which leads to a better understanding of the reaction mechanism.

Furthermore, an analysis which considers the influence of the forces was developed. Here, the dissociation constant is derived from the relation of the number of data points at a specific given force and the number of rupture events at this force.

In the second part of this work receptor – ligand interactions were investigated, which requires the controlled and specific binding of two interaction partners towards the surface. First, the influence of the multivalency on the Ni-NTA-histag complex was probed. Comparison of the behaviour of the tris-NTA/His6 system and the mono-NTA/His2 system reveals that affinity increases with increasing multivalency, but mechanical stability does not change. This might be explained by the geometry of the complex and thus leads to a deeper understanding of multivalent binding. Another application of force spectroscopic measurements of a receptor – ligand interaction was the investigation of the interaction between the prepeptid of the lantibiotic nisin and the ABC-exporter NisT. NisT is part of the modification machinery in the production of nisin. Fluorescent measurements as well as force spectroscopic data show a specific binding of prenisin, which allows deeper insights in this interaction.

Abkürzungsverzeichnis

AFM	Atomic Force Microscope
EPR	Electron Paramagnetic Resonance
NMR	Nuclear Magnetic Resonance
ABC Transporter	ATP-binding cassette Transporter
BR	Bacteriorhodopsin
SRII	Sensorhodopsin II
TM1 und TM2	transmembrane Helices 1und 2 des Transducers von SRII
TMD	Transmembrandomäne
NBD	Nukleotid bindende Domäne (Nucleotide Binding Domain)
BOC	Di-tert-butyl dicarbonat
DIC	Dicyclohexylcarbodiimid
EDC	Ethyl(dimethylaminopropyl) Carbodiimid
Fmoc	(Fluorenylmethyloxycarbonyl chlorid)
NHS	N-Hydroxysuccinylimid
NTA	Nitrilotriessigsäure
PEG	Polyethlyenglycol
WLC-Model	Worm Like Chain Model

Abbildungsverzeichnis

Anhang

L. Oberbarnscheidt , A. Reichel, M. Bhagawati, R. Janissen, J. Piehler, F. Oesterhelt, 2010
Multivalent interactions in flexible interaction pairs increase their affinity but not the mechanical stability
Manuskript in Revision

L. Oberbarnscheidt, R. Janissen, F. Oesterhelt, 2009
Direct and model free calculation of force-dependent dissociation rates from force spectroscopic data
Biophys. J., 97(9), 19-21

L. Oberbarnscheidt, R. Janissen, S. Martell, M. Engelhard, F. Oesterhelt, 2009
Single-molecule force spectroscopy measures structural changes induced by light activation and transducer binding in sensory rhodopsin II
J. Mol. Biol., 394(3), 383-390

R. Janissen, L. Oberbarnscheidt, F. Oesterhelt, 2009
Optimized straight forward procedure for covalent surface immobilization of different biomolecules for single molecule applications
Colloids Surf B Biointerfaces,71(2), 200-207

D.A. Cisneros, L. Oberbarnscheidt, A. Pannier, J.P. Klare, J. Helenius, M. Engelhard, F. Oesterhelt, D.J. Muller, 2008
Transducer binding establishes localized interactions to tune sensory rhodopsin II
Structure, 16(8), 1206-1213

Literaturverzeichnis

G.I. Bell, 1978
Models for the specific adhesion of cells to cells
Science, 200, 618–627

J.M. Berg, J.L Tymoczko, L. Stryer, 2002
Biochemie
Spektrum Verlag, 5. Auflage

E. Biemans-Oldehinkel, M.K. Doeven, B. Poolman, B., 2006
ABC transporter architecture and regulatory roles of accessory domains.
FEBS Lett. 580, 1023–1035.

G. Binnig, C.F. Quate, C. Gerber, 1986
Atomic force microscope
Phys. Rev. Letter, 56, 930

J. Buchner, 2002
Introduction: the cellular protein folding machinery
Cell Mol. Life Science, 59,1587-1588

C. Bustamante, J.F. Marko, E.D. Siggia, S. Smith, 1994
Entropic elasticity of λ-phage DNA
Science, 265, 1995

C. Chatterjee, M.Paul, L. Xie, W.A. van der Donk, 2005
Biosynthesis and Mode of Action of Lantibiotics
Chem. Rev. 105, 633-683

D.A. Cisneros, L. Oberbarnscheidt, A. Pannier, J.P. Klare, J. Helenius, M. Engelhard, F. Oesterhelt, D.J. Müller, 2008
Transducer binding establishes localized interactions to tune sensory rhodopsin II
Structure, 16(8), 1206-1213

D.A. Cisneros, D. Oesterhelt, D.J. Müller, 2005
Probing origins of molecular interactions stabilizing the membrane proteins halorhodopsin and bacteriorhodopsin
Structure, 13, 235–242

H. Clausen-Schaumann, M. Rief, C. Tolksdorf, H.E. Gaub, 2000
Mechanical stability of single DNA molecules
Biophys J. 2000, 78(4), 1997-2007

M. Conti, G. Falini, B. Saporì, 2000
How Strong Is the Coordination Bond between a Histidine Tag and Ni ± Nitrilotriacetate? An Experiment of Mechanochemistry on Single Molecules
Angew. Chem. Int. Ed., 39, 1

D.M. Czajkowsky, Z. Shao, 1998
Submolecular resolution of single macromolecules with atomic force microscopy
FEBS Lett., 430, 51–54

R.J. Dawson, K.P. Locher, 2006
Structure of a bacterial multidrug ABC transporter.
Nature 443, 180–185

C.M. Dobson, 1999
Protein misfolding, evolution and disease
Trends Biochem. Sci., 24, 329–332

C.M. Dobson, 2002
Getting out of shape
Nature, 418, 729–730

A. Engel, D.J. Müller, 2000
Observing single biomolecules at work with the atomic force microscope
Nat. Struct. Biol., 7, 715–718

E. Evans, K. Ritchie, 1997
Dynamic strength of molecular adhesion bonds
Biophys. J., 72, 1541–1555

E. Evans, 1998
Energy landscapes of biomolecular adhesion and receptor anchoring at interfaces explored with dynamic force spectroscopy
Faraday Discuss 111, 1–16

E. Evans, 2001
Probing the relation between force lifetime and chemistry in single molecular bonds
Annu. Rev. Biophys. Biomol. Struct., 30, 105–128

A. Guiotto, M. Pozzobon, M. Canevari, R. Manganelli, M. Scarin, F.M. Veronese, 2003
PEGylation of the antimicrobial peptide nisin A: Problems and perspectives
Il Farmaco, 58, 45-50

V.I. Gordeliy, J. Labahn, R. Moukhametzianov, R. Efremov, J. Granzin, R. Schlesinge, 2002
Molecular basis of transmembrane signalling by sensory rhodopsin II–transducer complex
Nature, 419, 484–487

U. Haupts, J. Tittor, E. Bamberg, D. Oesterhelt, 1997
General concept for ion translocation by halobacterial retinal proteins: The isomerization/Switch/Transfer (IST) model
Biochemistry, 7, 2–7

U. Haupts, J. Tittor, D. Oesterhelt, 1999
Closing in on bacteriorhodopsin: Progress in understanding the molecule
Annu. Rev. Biophys. Biomol. Struct., 28, 367–399

J.B. Heymann, D.J. Müller, E. Landau, J. Rosenbusch, E. Pebay-Peroulla, G. Büldt, 1999
Charting the surfaces of the purple membrane
J. Struct Biol., 128, 243–249

C.F. Higgins, K.J. Linton, 2004
The ATP switch model for ABC trasnporters
Nat.Struct.Mol.Biol. 918-926

S. Hippler-Mreyen, J.P. Klare, A.A. Wegener, R. Seidel, C. Herrmann, G. Schmies, 2003
Probing the sensory rhodopsin II binding domain of its cognate transducer by calorimetry and
electrophysiology
J. Mol. Biol., 330, 1203–1213

S. Izrailev, S. Stepaniants, M. Balsera, Y. Oono, K. Schulten, 1997
Molecular dynamics study of unbinding of the Avidin-Biotin complex
Biophys. J., 72, 1568–1581

R. Janissen, L. Oberbarnscheidt, F. Oesterhelt., 2009
Optimized straight forward procedure for covalent surface immobilization of different biomolecules for single molecule applications.
Colloids Surf B Biointerfaces, 71(2), 200-207

H. Janovjak, A. Kedrov, D.A. Cisneros, K.T. Sapra, J. Struckmeier, D.J. Müller, 2006
Imaging and detecting molecular interactions of single transmembrane proteins
Neurobiology of Aging, 27, 546–561

H. Janovjak, M. Kessler, H. Gaub, D. Oesterhelt, D.J. Müller, 2003
Unfolding pathways of native bacteriorhodopsin depend on temperature
EMBO J., 22, 5220–5229

H. Janovjak, J. Struckmeier, M. Hubain, A. Kedrov, M. Kessler, D.J. Müller, 2004
Probing the energy landscape of the membrane protein bacteriorhodopsin
Structure, 12, 871–879

C. Jarzynski, 1997
Nonequilibrium Equality for Free Energy Differences
Phys. Rev. Lett., 78, 2690-2693

P.R. Jensen, K. Hammer, 1993
Minimal Requirements for Exponential Growth of Lactococcus lactis, 1993
Appl. Environ. Microbiol., 59(12), 4363-4366

C. Kaletta, K.D. Entian, 1989
Nisin, a peptide antibiotic: Cloning and sequencing of the nisA gene and posttranslational processing of its peptide product
J. Bacteriol., 171(3), 1597-1601

N. Kartner, J.R. Riordan, V. Ling, 1983
Cell surface P-glycoprotein associated with multidrug resistance in mammalian cell lines.
Science, 221, 1285–1288.

A. Kedrov, C. Ziegler, H. Janovjak, W. Kühlbrandt, D.J. Müller, 2004
Controlled unfolding and refolding of a single sodium-proton antiporter using atomic force microscopy
J. Mol. Biol., 340, 1143–1152

S.K. McKeegan, M.I. Borges-Walmsley, A.R. Walmsley, 2003
The structure and function of drug pumps: An update
TRENDS in Microbiology, 11, 1

M.S. Kellermayer, S.B. Smith, H.L. Granzier, C. Bustamante, 1997
Folding unfolding transitions in single titin molecules characterized with laser tweezers
Science, 276, 1112–1116

F. Kienberger, G. Kada, H.J. Gruber, V.Ph. Pastushenko, C. Riener, M.Trieb, H.G. Knaus, H. Schindler, P. Hinterdorfer, 2000
Recognition Force Spectroscopy Studies of the NTA-His6 Bond
Single Mol. 1, 1, 59-65

J.P. Klare, I. Chizhov, M. Engelhard, 2008
Microbial rhodopsins: Scaffolds for ion pumps, channels, and sensors
Results Probl. Cell Differ., 45, 73–122

J.P. Klare, V.I. Gordeliy, J. Labahn, G. Büldt, H.-J. Steinhoff, M. Engelhard, 2004
The archaeal sensory rhodopsin II/Transducer complex: A model for transmembrane signal transfer
FEBS Lett., 564, 219–224

H. A. Kramers, 1940
Brownian motion in a field of force and the diffusion model of chemical reactions
Physica, 7, 284-304

A. Kuipers, E. de Boef, R. Rink, S. Fekken, L.D. Kluskens, A.J.M. Driessen, K. Leenhouts, O.P.Kuipers, G.N. Mol, 2004
NisT, the Transporter of the Lantibiotic Nisin, Can Transport Fully Modified, Dehydrated, and Unmodified Prenisin and Fusions of the Leader Peptide with Non- Iantibiotic Peptides
JBC Papers, 279(21), 22176-82

S. Lata, A. Reichel, R. Brock, R. Tampé and J. Piehler, 2005
High-Affinity Adaptors for Switchable Recognition of Histidine-Tagged Proteins
J. Am. Chem. Soc., 127, 10205-10215

E.M. Leslie, R.G. Deeley, S.P. Cole, 2005
Multidrug resistance proteins: role of P-glycoprotein, MRP1, MRP2, and BCRP (ABCG2) in tissue defense
Toxicol. Appl. Pharmacol, 204, 216–237

C. Levinthal, 1968
Are there pathways for protein folding?
Journal de Chimie Physique et de Physico-Chimie Biologique 65, 44–45

J. Liphardt, S. Dumont, S.B. Smith, I. Tinoco Jr., C. Bustamante, 2002
Equilibrium Information from Nonequilibrium Measurements in an Experimental Test of Jarzynski's Equality
Science, 296, 5574, 1832–1835

G. Lu, J.M.Westbrooks, A.L. Davidson, J. Chen, 2005
ATP hydrolysis is required to reset the ATP-binding cassette dimer into the resting-state conformation
Proc. Natl. Acad. Sci. USA 102, 17969–17974

J. Lubelski, R. Rink, R. Khusainov, G.N. Moll, O.P. Kuipers, 2008
Biosynthesis, immunity, regulation, mode of action and engineering of the model lantibiotic nisin
Cell. Mol. Life Sci., 65, 455–476

J.F. Marko, E.D. Siggia, 1995
Stretching DNA
Macromolecules, 28, 8759

C. Möller, M. Allen, V. Elings, A. Engel, D.J. Müller, 1999
Tapping mode atomic force microscopy produces faithful high-resolution images of protein surfaces
Biophys J., 77, 1050–1058

R. Moukhametzianov, J.P. Klare, R. Efremov, C. Baeken, A. Göppner, J. Labahn, 2006
Development of the signal in sensory rhodopsin and its transfer to the cognate transducer
Nature, 440, 115–119

L. Oberbarnscheidt, R. Janissen, S. Martell, M. Engelhard, F. Oesterhelt, 2009
Single-molecule force spectroscopy measures structural changes induced by light activation and transducer binding in sensory rhodopsin II
J Mol Biol., 394(3), 383-90

L. Oberbarnscheidt, R. Janissen, F. Oesterhelt, 2009
Direct and model free calculation of force-dependent dissociation rates from force spectroscopic data.
Biophys J., 97(9), 19-21

F. Oesterhelt, D. Oesterhelt, M. Pfeiffer, A. Engel, H.E. Gaub, D.J. Müller, 2000
Unfolding pathways of individual bacteriorhodopsins
Science, 288, 143–146

C. Oswald, I.B. Holland, L. Schmitt, 2006
The motor domains of ABC-transporters: What can structures tell us?
Naunyn-Schmiedeberg's Arch Pharmacol, 372, 385–399

G.C. Patton, W.A. van der Donk, 2005
New developments in lantibiotic biosynthesis and mode of action.
Curr Opin Microbiol., 8(5), 543-51

J.L. Popot, D.M. Engelmann, 1990
Membrane protein folding and oligomerization: The two stage model
Biochemistrty, 29, 4031–4037

J.L. Popot, S.E. Gerchmann, D.M. Engelmann, 1987
Refolding of bacteriorhodopsin in lipid bilayers: A thermodynamically controlled two-stage process
J. Mol. Biol., 198, 655–676

S.E. Radford, 2000
Protein folding: Progress made and promises ahead
Trends Biochem. Sci., 25, 611–618

T.V. Ratto, R.E. Rudd, K.C. Langry, R.L. Balhorn, M.W. McElfresh, 2006
Nonlinearly Additive Forces in Multivalent Ligand Binding to a Single Protein Revealed with Force Spectroscopy
Langmuir, 22, 1749-1757

M. Rief, M. Gautel, F. Oesterhelt, J.M. Fernandez, H.E. Gaub, 1997
Reversible unfolding of individual titin immunoglobulin domains by AFM
Science, 276, 1109–1112

M.J. Roberts, M.D. Bentley, J.M. Harris, 2002
Chemistry for peptide and protein PEGylation
Adv. Drug. Deliv. Rev., 17, 54(4), 459-476

J. Rudolph, D. Oesterhelt, 1995
Chemotaxis and phototaxis require a CheA histidine kinase in the archaeon Halobacterium salinarium
EMBO J., 14, 667–673

J. Rudolph, D. Oesterhelt, 1996
Deletion analysis of the che operon in the archaeon Halobacterium salinarium
J. Mol. Biol., 258, 548–554

K.T. Sapra, H. Besir, D. Oesterhelt, D.J. Müller, 2006
Characterizing molecular interactions in different bacteriorhodopsin assemblies by single-molecule force spectroscopy
J. Mol. Biol., 355(4), 640-650

S. Scheuring, J.L. Rigaud, J.N. Sturgis, 2004
Variable LH2 stoichiometry and core clustering in native membranes of Rhodospirillum photometricum
EMBO J., 23, 4127–4133

S. Scheuring, J. Seguin, S. Marco, D. Levy, B. Robert, J.L. Rigaud, 2003
Nanodissection and high-resolution imaging of the Rhodopseudomonas viridis photosynthetic core complex in native membranes by AFM
Proc. Natl. Acad. Sci., 100, 1690–1693

L. Schmitt, M. Ludwig, H.E. Gaub, Robert Tampé, 2000
A Metal-Chelating Microscopy Tip as a New Toolbox for Single-Molecule Experiments by Atomic Force Microscopy
Biophys. J., 78, 3275–3285

G. Schmies, M. Engelhard, P.G. Wood, G. Nagel, E. Bamberg, 2001
Electrophysiological characterization of specific interactions between bacterial sensory rhodopsins and their transducers
Proc. Natl. Acad. Sci., 98, 1555–1559

A.K. Sharma, J.L. Spudich, W.F. Doolittle, 2006
Microbial rhodopsins: functional versatility and genetic mobility
Trends Microbiol., 14, 463–469

G.K. Schuurman- Wolters, B. Poolman, B., 2005
Substrate specificity and ionic regulation of GlnPQfrom Lactococcus lactis. An ATP-binding cassette transporter with four extracytoplasmic substrate-binding domains
J Biol. Chem. 280, 23785–23790

A.E. Senior, M.K. al-Shawi, I.L. Urbatsch, 1995
The catalytic cycle of P-glycoprotein
FEBS Lett 377, 285–289.

K. Siegers, S. Heinzmann, K.D. Entian, 1996
Biosynthesis of lantibiotic nisin. Posttranslational modification of its prepeptide occurs at a multimeric membrane-associated lanthionine synthetase complex
J. Biol. Chem., 271(21), 12294–12301

S.J. Singer, G.L. Nicolson, 1972
The fluid mosaic model of the structure of cell membranes.
Science, 175, 720–731

J.L. Spudich, 1998
Variations on a molecular switch: Transport and sensory signalling by archaeal rhodopsins
Mol. Microbiol., 28, 1051–1058

Y. Sudo, M. Iwamoto, K. Shimono, M. Sumi, N. Kamo, 2001
Photo-induced proton transport of pharaonis phoborhodopsin (sensory rhodopsin II) is ceased by association with the transducer
Biophys. J., 80, 916–922

Y. Sudo, J.L. Spudich, 2006
Three strategically placed hydrogen-bonding residues convert a proton pump into a sensory receptor
Proc. Natl. Acad. Sci., 103, 16129–16134

T. Sulchek, R. W. Friddle, A. Noy, 2006
Strength of Multiple Parallel Biological Bonds
Biophysical Journal, 90, 4686–4691

I.L. Urbatsch, G.A. Tyndall, G. Tombline, A.E. Senior, 2003
P-glycoprotein catalytic mechanism: studies of the ADP-vanadate inhibited state.
J Biol. Chem. 278, 23171–23179

F. Valle, G. Zuccheri, A. Bergia, L. Ayres, A.E. Rowan, R.J.M. Nolte, B. Samorì, 2008
A polymeric molecular "handle" for multiple AFM-based single-molecule force measurements
Angew. Chem. Int. Ed., 47, 2431-2434
.
C. Verbelen, H.J. Gruber, Y.F. Dufrêne, 2007
The NTA-His6 bond is strong enough for AFM single-molecular recognition studies
J. Mol. Recognit., 20(6),490-4

H.W. van Veen, A. Margolles, M. Muller, C.F. Higgins, W.N. Konings, 2000
The homodimeric ATP-binding cassette transporter LmrA mediates multidrug transport by an alternating two-site (two-cylinder engine) mechanism.
EMBO J 19, 2503–2514

F.M. Veronese, 2001
Peptide and protein PEGylation: A review of problems and solutions
Biomaterials, 22(5), 405-417

M.B. Viani, L.I. Pietrasanta, J.B. Thompson, A. Chand, I.C. Gebeshuber, J.H. Kindt, 2000
Probing protein–protein interactions in real time
Nat. Struct. Biol., 7, 644–647

J.E. Walker, M. Saraste, M.J. Runswick, N.J. Gay, 1982
Distantly related sequences in the alpha- and beta-subunits of ATP synthase, myosin, kinases and other ATP-requiring enzymes and a common nucleotide binding fold
Embo J., 1, 945–951

A.A. Wegener, I. Chizhov, M. Engelhard, H.J. Steinhoff, 2000
Time-resolved detection of transient movement of helix F in spin-labelled pharaonis sensory rhodopsin II
J. Mol. Biol., 301, 881–891

C.S. Yang, O. Sineshchekov, E.N. Spudich, J.L. Spudich, 2004
The cytoplasmic membraneproximal domain of the HtrII transducer interacts with the E-F loop of photoactivated Natronomonas pharaonis sensory rhodopsin II
J. Biol. Chem., 279, 42970–42976

J. Zaitseva, S. Jenewein, T. Jumpertz, I.B. Holland, L. Schmitt, 2005
H662 is the linchpin of ATP hydrolysis in the nucleotide-binding domain of the ABC transporter HlyB.
Embo J., 25(14), 3432-43

J. Zaitseva, C. Oswald, T. Jumpertz, S. Jenewein, A .Wiedenmann, I.B. Holland, L. Schmitt, 2006
A structural analysis of asymmetry required for catalytic activity of an ABC-ATPase domain dimer. EMBO J 25, 3432– 3443.

Danksagung

Mein Dank für die Unterstützung bei der Erstellung meiner Doktorarbeit, für das interessante Thema und die Möglichkeit meine Ideen entwickeln zu können, geht an meinen Doktorvater Dr. Filipp Oesterhelt.

Auch möchte ich mich für die kollegiale Atmosphäre und Zusammenarbeit in der Gruppe Oesterhelt bei Dmytro Rodnin, Arpita Roychoudhury, Dr. Olga Franco und Dr. Richard Janissen, ihm besonders für die Einarbeitung und Hilfe mit der Software, bedanken.

Allen Mitgliedern des Instituts für physikalische Chemie II danke ich für die gute Arbeitsatmosphäre; vor allem Heike Hornen, Andreas Renner für Unterstützung im Biolabor, Markus Richert und Marcel Merkwitz für Hilfe mit der HPLC, Dr. Ralph Kühnemuth und Denis Dörr für verschiedenste fachliche Diskussionen und Prof. Dr. Claus Seidel für seine Unterstützung. Dafür, dass auf sie immer Verlass ist, möchte ich mich besonders bei Stefanie Grabowski und Heike Hornen bedanken.

Darüber hinaus bedanke ich mich bei meinen Kooperationspartnern, den Biochemikern aus Düsseldorf, Britta Tschapek, Nino Mavaro, Patrick Bakkes, Dr. Sander Smits und Prof. Dr. Lutz Schmitt für eine direkte, offene, hilfsbereite und spannende Kooperation.
Ebenso gilt mein Dank den Kooperationspartnern in Frankfurt, bzw. Osnabrück Dr. Annett Reichel und Prof. Dr. Jacob Piehler für eine fruchtbare und gute Kooperation.

BioStruct danke ich für finanzielle und organisatorische Unterstützung.

Von Herzen möchte ich mich auch bei meiner Familie und Freunden bedanken.

Leoni Oberbarnscheidt

Multivalent interactions in flexible interaction pairs increase the affinity but not the mechanical stability

Multivalent Ni-NTA binds oligohistidine peptides with very high affinity. The binding interface, however, is probably highly flexible in nature. Here, we explored the mechanical stability of these complexes by applying single molecule force spectroscopy. By rate-dependent force measurements, an off-rate of 0.5 s^{-1} was obtained for the mono-NTA/H2 complex in good agreement with the dissociation rate constant determined by total internal reflection fluorescence spectroscopy (TIRFS). Interestingly, the rupture forces of the mono-NTA/H2 complex were found to be the same as those of the tris-NTA/H6 complex and show the same dependence on the loading rate, while the affinity measured by TIRFS significantly increases. This counter-intuitive result can be explained by the flexibility of the multivalent complex and point towards how to engineer mechanical stabilities of multivalent interactions.

Stabilization of noncovalent macromolecular complexes by multivalent interactions plays an important role for many biological processes including signal transduction, viral infection, pathogen recognition and their elimination by the immune system.[1,2] During the past decade, multivalency has been very successfully exploited for rational design of high affinity binders in biology, chemistry and nanoscience.[3-9] Recently, this approach has been applied for designing multivalent chelators (MCH) as high-affinity binders of oligohistidine peptides.[10] For this purpose, multiple nitrilotriacetic acid (NTA) moieties were grafted onto different scaffolds. Individual Ni(II)-NTA complexes can bind two histidine residues in the octahedral ligand sphere of the Ni(II) ion (Figure 1a), yielding a binding affinity of ~10 µM.[10] In contrast, binding affinities tow ards oligohistidine peptides in the lower nanomolar range were achieved for the MCH tris-NTA (Figure 1b), which can simultaneously coordinate six histidine residues. These complexes, however, were shown to have a highly dynamic interface, where histidine residues constantly exchange coordination sites.[11,12] This property can be ascribed to the highly flexible nature of both interaction partners and the degenerate nature of the interaction sites. Here, we explored the consequences of such dynamic interfaces in multivalent complexes for their mechanical properties. To this end, we probed the mechanical stability on the single molecule level by dynamic force spectroscopy and compared it with the spontaneous dissociation kinetics. While equilibrium measurements result in dissociation rates, force measurements in addition give insights in its complex geometry. A more antiparallel orientation of the single coordinative bonds of the multivalent complex would lead to an increased unbinding force, whereas a more parallel, zipper like orientation would result in none or only a very small increase in unbinding force.

A peptide containing either two or six histidine residues (H2 and H6, respectively) was attached to an AFM tip via a poly(ethylene glycol) (PEG) linker and was presented to mono-NTA or tris-NTA chelator heads, which were immobilized on glass surfaces through a PEG polymer brush (Figure 1c).[13] Thus, different interaction scenarios with different degrees of multivalency were probed (Figure 1d). A broad spectrum of rupture forces of the mono-NTA/H6 complex has been reported previously, ranging from 38 pN up to 500 pN.[14-18]

The different unbinding forces might result from a different orientation of the NTA due to different positions where the linker is coupled. This leads to the complexes being ruptured in either a more parallel or antiparallel mode. However, also in the case of identical coupling, different forces were reported by different groups, which might be due to multiple bond measurements and to additional non-specific interactions with the substrate surfaces. In order to minimize these potential biases, mono- and tris-NTA were coupled in low density through a dense PEG polymer brush[13] with an average molecular mass of 6000 g/mol. Binding of fluorescence-labeled H2 and H6 peptides to these surfaces was probed by total internal reflection fluorescence spectroscopy (TIRFS). Highly specific binding of these peptides was observed (Figure 1e, f and Supporting information) confirming the excellent functional properties of these surface architectures.[13] The binding properties of different interaction pairs were characteristic and in line with previous studies: while strong and stable binding of H6 to tris-NTA was observed, transient and much weaker, yet significant binding was observed for H2. Binding to mono-NTA was much weaker compared to tris-NTA, yet specific binding could be detected for both H6 and H2. The relatively strong binding of H6 is probably due to surface multivalency, since even stronger binding was observed for high mono-NTA surface densities (Supporting information).

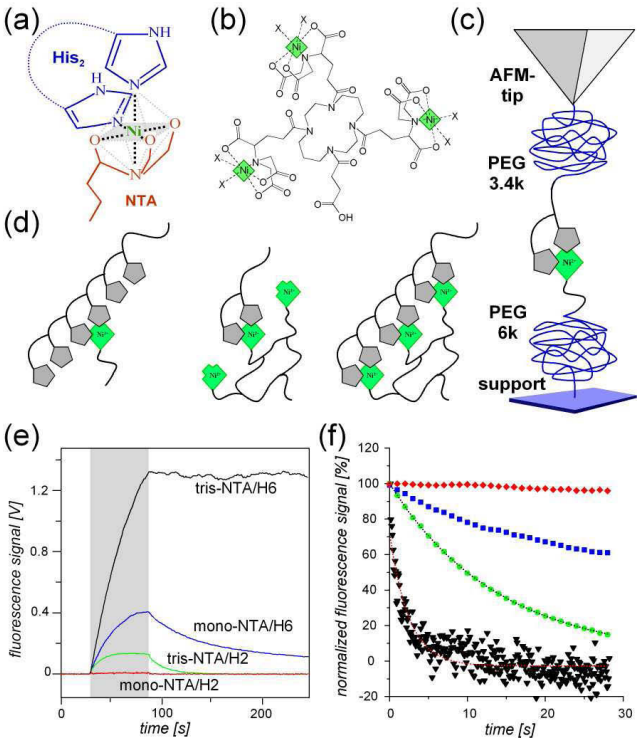

Figure 1 Multivalent recognition of MCH/oligohistidine complexes. (a) Octahedral coordination sphere of Ni(II) chelated by NTA, which binds two adjacent histidine residues. (b) Structure of tris-NTA loaded with three Ni(II) ions. (c) Surface architecture for probing the mechanical stability of NTA/oligohistdine interactions. The PEG spacers are indicated in blue. (d) Architectures of the complexes probed in this study. (e) Binding of 500 nM fluorescence-labeled H2 and H6 peptides to mono- and tris-NTA as detected by TIRFS and spontaneous dissociation upon washing with buffer. The injection period is highlighted in grey. (f) Comparison of the normalized dissociation kinetics from the experiments shown in (e).

The very weak signal obtained for the mono-NTA/H2 complex, however, corresponds to the unbiased interaction of two histidines with an NTA-complexed Ni(II) ion. Fitting an exponential decay to this dissociation phase (Figure 1f) yielded a dissociation rate constant $k_d = 0.5\ s^{-1}$, which is in good agreement to the k_d obtained for mono-NTA/oligohistidine complexes in solution.[10] For dynamic force spectroscopy experiments, the density of histidine peptides coupled to the PEG-modified AFM was systematically optimized for individual interaction events (Supplementary information). Rupture forces and their dependence on the loading rate were determined for all four interaction pairs at different loading rates. Under these optimized conditions, approximately one third of the force-distance curves showed a single rupture event when presenting an H2-modified tip to a mono-NTA functionalized

surface loaded with Ni(II) ions (Figure 2a). Specificity of these rupture events was confirmed by removing Ni(II) ions with EDTA (Supplementary information).

Rupture curves of single NTA/Histidine complexes were fitted with a model that describes the stretching of a single PEG linker (Figure 2a).[19]

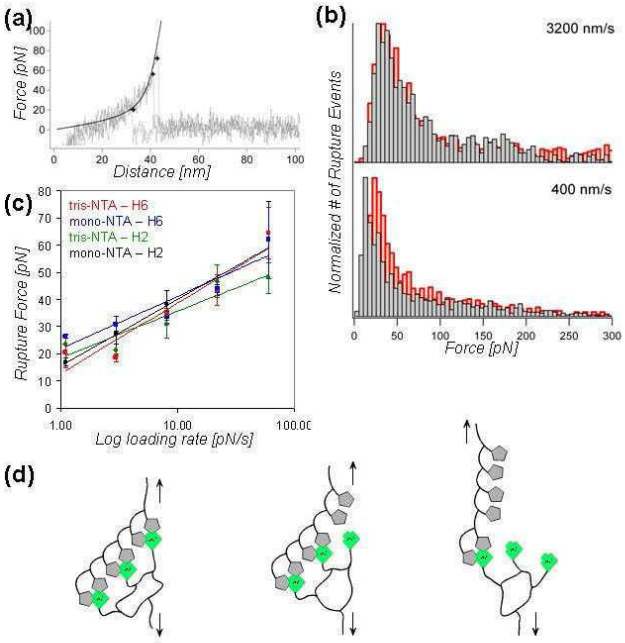

Figure 2 Dynamic force spectroscopy. (a) Overlay of typical retraction curves. Forces needed to rupture the complex are marked as black crosses and were taken for further analysis. (b) Force distribution histograms at different loading rates (top: 3200 µm/s; bottom 400 µm/s) measured for mono-NTA/H2 (black histogram) and tris-NTA/H6 (red histrogram). (c) Loading rate-dependence of the rupture force for all complexes investigated. (d) Potential sequential rupture mechanism explaining the low mechanic stability of multivalent tris-NTA/H6 complexes.

Almost all obtained curves could be fitted with this model, confirming that no multiple events occurred. Moreover, the monomer length distribution showed a monomodal Gaussian distribution. Histograms showing the force distribution of rupture events of the mono-NTA/H2 complex show a main force peak that varies between 15 pN and 70 pN (Figure 2b), which is in the same range as reported previously.[15,16,18] It is proportional to the logarithm of the average instantaneous loading rate (Figure 2c) and according to Bell-Evan´s approach,[20,21] a dissociation rate constant k_d of 0.5 s^{-1} was obtained from the loading rate-dependent rupture

force, which is in good agreement with the dissociation rate constant obtained by the TIRFS binding assays.

Specific, and monomodal binding was also observed for the other three interaction pairs. The equilibrium measurements on the mono-NTA/His6 interaction show that its dissociation rate is significantly higher than that of the MCH complex. Thus, fluctuations within the MCH are so fast that this complex behaves as having a smooth binding potential with only one energy barrier justifying the application of Kramer´s model.

The peak forces measured for the disruption of all these complexes were found to be the same within the error limits of forces measured for the mono-NTA/H2 complex and showed the same dependency on the loading rates (Figure 2c), yielding similar apparent k_d values.

This is in contrast to the highly different spontaneous dissociation kinetics of these complexes as shown in (Figure 1f), which leads to the conclusion that the MCH is loaded in a more stepwise or zipper like manner (Figure 2d). There, the unbinding forces show none or only a minimal increase with increasing multivalency of the complex depending on the length increase upon the rupture of the individual Ni-NTA/H2 bonds, which is also known from DNA force measurements.[22] However, a possible increase in the unbinding forces and length increase upon rupture of the individual Ni-NTA/His2 was below the resolution of the AFM.

We suggest that this low mechanical stability of tris-NTA/H6 complexes may represent a generic feature of highly flexible interaction partners. Thus, these mechanical properties of multivalent NTA/oligohistidine complexes have some important consequences on their general application as molecular handles in single molecule manipulation experiments.

Acknowledgment We thank Gerhard Spatz-Kümbel for technical assistance. J.P was a Heisenberg-Professor funded by the DFG (PI 405/3). L.O. is a fellow of the NRW Research School BioStruct supported by German Federal State NRW and from the Entrepreneur Foundation at the HHU Düsseldorf.

Supporting Information Available: Description of the methods, Figures showing specific and imidazole-reversible binding of oligohistidine peptides, detailed TIRFS binding curves for H2 and H6 peptides, and histograms comparing changes in rupture force when diluting the peptide at the tip and competitive measurements with EDTA.

References

(1) Mammen, M.; Choi, S. K.; Whitesides, G. M., Angewandte Chemie-International Edition, 1998, 37, 2755-2794.

(2) Kitov, P. I.; Bundle, D. R., J. Am. Chem. Soc., 2003, 125, 16271-16284.

(3) Mulder, A.; Huskens, J.; Reinhoudt, D. N., Org. Biomol. Chem., 2004, 2, 3409-3424.

(4) Gargano, J. M.; Ngo, T.; Kim, J. Y.; Acheson, D. W.; Lees, W. J., J. Am. Chem. Soc., 2001, 123, 12909-12910.

(5) Gestwicki, J. E.; Cairo, C. W.; Strong, L. E.; Oetjen, K. A.; Kiessling, L. L., Journal of the American Chemical Society, 2002, 124, 14922-14933.

(6) Kitov, P. I.; Sadowska, J. M.; Mulvey, G.; Armstrong, G. D.; Ling, H.; Pannu, N. S.; Read, R. J.; Bundle, D. R., Nature, 2000, 403, 669-672.

(7) Reczek, J. J.; Kennedy, A. A.; Halbert, B. T.; Urbach, A. R., J. Am. Chem. Soc., 2009, 131, 2408-2415.

(8) Badjic, J. D.; Nelson, A.; Cantrill, S. J.; Turnbull, W. B.; Stoddart, J. F., Acc. Chem. Res., 2005, 38, 723-732.

(9) Kiessling, L. L.; Gestwicki, J. E.; Strong, L. E., Angew. Chem. Int. Ed. Engl., 2006, 45, 2348-2368.

(10) Lata, S.; Reichel, A.; Brock, R.; Tampé, R.; Piehler, J., J. Am. Chem. Soc., 2005, 127, 10205-10215.

(11) Reichel, A.; Lata, S.; Piehler, J., 2009, submitted.

(12) Andre, T.; Reichel, A.; Wiesmüller, K. H.; Tampe, R.; Piehler, J.; Brock, R., Chem.Bio.chem., 2009, 10, 1878-1887.

(13) Lata, S.; Piehler, J., Anal. Chem, 2005, 77, 1096 -1105.

(14) Conti, M.; Falini, G.; Samori, B., Angew. Chem. Int. Ed. Engl., 2000, 39, 215-218.

(15) Schmitt, L.; Ludwig, M.; Gaub, H. E.; Tampe, R., Biophys. J., 2000, 78, 3275-3285.

(16) Kienberger, F.; Kada, G.; Gruber, H. J.; Pastushenko, V. P.; Riener, C.; Trieb, M.; Knaus, H.-G.; Schindler, H.; Hinterdorfer, P., Single Molecule, 2000, 1, 59-65.

(17) Verbelen, C.; Gruber, H. J.; Dufrene, Y. F., J. Mol. Recognit., 2007, 20, 490-494.

(18) Valle F.; Zuccheri G.; Bergia A.; Ayres L.; Rowan A. E.; Nolte R. J. M.; Samorì B., Angew. Chem. Int. Ed., 2008, 47, 2431-2434.

(19) Oesterhelt, F.; Rief, M.; Gaub, H. E., New J. Phys., 1999, 1, 6.

(20) Evans, E.; Ritchie, K., Biophys. J., 1997, 72, 1541-1555.

(21) Bell, G., I. Science, 1978, 200, 618-627.

(22) Clausen-Schaumann H.; Rief M.; Tolksdorf C.; Gaub H.E., Biophys. J., 2000, 78(4), 1997-2007.

Supporting information

Multivalent interactions in flexible interaction pairs increase their affinity but not the mechanical stability

Leoni Oberbarnscheidt[‡], Annett Reichel[†], Maniraj Bhagawati[†], Richard Janissen[‡]
Jacob Piehler[†], Filipp Oesterhelt [‡]

[‡] *Institut für molekulare physikalische Chemie, 40225 Düsseldorf, Germany*
[†]*Division of Biophysics, University of Osnabrück, 49076 Osnabrück, Germany*

Supporting Information

Experimental Section

Materials

Diamino-polyethylene glycol with MW 6000 Da (PEG6000) was purchased from Rapp Polymere and with MW 3400 was custom-synthesized by LaysanBio. Hexahistidine and bishistidine peptides were custom-synthesised at the BMFZ (Biomedizinisches Forschungszentrum, Heinrich-Heine-University). Oregon Green 488 maleimide (OG488 maleimide) was purchased from Invitrogen. OtBu-protected-tris- and mono-NTA carboxylic acids were synthesized as described previously.[1] Si_3N_4 cantilevers are of the MLCT series from Veeco Instruments. Other chemicals were purchased from Sigma Aldrich and used as obtained.

Fluorescent labelling of peptide

H2 and H6 peptides were site-specifically labeled with Oregon Green 488 (OG488) maleimide through a cysteine residue at the C-terminus of the peptide with. The reaction was carried out in HEPES buffered saline (20 mM HEPES, 150 mM NaCl, pH 7.5, HBS) at room temperature with peptide and dye concentrations of 50 µM each.

Surface modification

Functionalization of surfaces with mono- and tris-NTA was carried out as described in detail previously.[2] Transducer slides for simultaneous reflectance interference/total internal

reflection fluorescence spectroscopy (RIf/TIRFS) detection were cleaned with 1 M NaOH for 3 min followed by overnight incubation in a freshly prepared mixture of one part hydrogen peroxide and two parts concentrated sulfuric acid. After rinsing with water and drying in a nitrogen stream, the surfaces were silanized with glycidyloxypropyltrimethoxysilane (GOPTS). PEG6000 was reacted with the epoxy groups on the surface as described before [3]. The surface amines were then coupled with OtBu-protected mono-NTA and tris-NTA carboxylic acids in the presence of N,N'-Diisopropylcarbodiimide (DIC). In order to minimize surface density induced multivalency, a diluted NTA surface was achieved by using an equimolar solution of the respective NTA and acetic acid (12 mM in chloroform) for conducting the reaction. The substrates were then incubated in trifluoroacetic acid overnight to cleave of the tert-butyl esters and free the NTA head groups.

Peptide binding experiments through Reflectance Interference/Total Internal Reflection Fluorescence Spectroscopy (RIf/TIRFS)

Measurements by RIf/TIRFS were carried out with a home-built set-up including continuous flow through conditions as described earlier.[4] Mono-NTA and tris-NTA functionalized substrates were treated with 100 mM HCl in the flow cell, followed by equilibration in HBS. The NTA head groups were then loaded with Ni(II) by the injection of a 10 mM solution of $NiCl_2$ in HBS. Fluorescence-labeled H2 and H6 peptides were then injected and the kinetics of binding and dissociation were monitored. Surfaces were regenerated by an injection of 500 mM imidazole in HBS to remove the peptide and a further wash by 100 mM HCl to remove the bound Ni(II). Data was acquired at a rate of 1 Hz, except for the case of mono-NTA/His2 interaction where an acquisition rate of 16 Hz was used.

Functionalisation of tips

The functionalisation of the tips is based on procedures described in detail previously.[5] Briefly, prior to functionalisation Si_3N_4 cantilevers were washed in chloroform and activated over night in 2.5 M NaOH. For amination the tips were left in 2.5 M ethanolamine hydrochloride, dissolved in water-free DMSO for 12 hours at 70 °C. PEG was coupled by incubation for 1 hour at room temperature in a PEG solution containing 2 mM NHS-PEG-$Maleimide_{MW3400}$ dissolved in water-free chloroform with 0.5% (v/v) triethylamine. To allow measurements of single molecule interactions the moiety of PEG having the maleimide endgroup (which further reacts with the cystein of the histidinepeptide) was diluted by mixing NHS-PEG-$Maleimide_{MW3400}$ and NHS-PEG-$COOH_{MW3400}$ in a ratio of 5:95. The H2 and H6 peptide were coupled to the maleimid-endgroup of the PEG via its cystein by incubation of

the PEGylated tips in 100 µM peptide (diluted in water) for 15 minutes at room temperature. Between each step the tips were washed extensively in the respective solvent. Functionalised tips were stored in HBS for at latest a week.

AFM Measurements and data analysis

Force-distance measurements were performed in HBS with an atomic force microscope from Asylum Research (MFP-3D) using modified Si_3N_4 cantilevers. The spring constant of 30±10 pN/nm was determined using the equipartition theorem.[6] Prior to measurements, NTA-surfaces were washed with HBS containing 100 mM EDTA, then HBS and then directly loaded with HBS-buffer containing 20 mM $NiCl_2$. The peptide-modified tip was presented to the NTA-functionalised surface with a force of ~10 pN for 1s and was then retracted with different velocities (400 nm/s, 800 nm/s, 1600 nm/s, 3200 nm/s, 6400 nm/s). For further analysis force curves of 2-5 experiments (different tip and surface) per combination and pulling velocity were selected and analysed using self written procedures in IGOR. For analysing curves which show the rupture of a single complex, we selected only those which matched the fit showing the stretching of a single PEG linker perfectly.[7] From each experiment with 100-300 selected curves showing the pulling at a single PEG-polymer (10-30 % of force curves) histograms with a binning of 5 pN were created and normalised on the main force peak.

The additional constant force pulling on the cantilever due to viscosity automatically is taken into account by measuring the rupture forces relative to the zero force line directly after the rupture events.

To account for the error in the calculated spring constant which propagates into the resulting average rupture force we calculated the most probable rupture forces of all force curves taken with each individual cantilever. Finally, the average rupture force of these values was calculated for each pulling speed and is shown in Figure 2c.

.

Supporting Figures

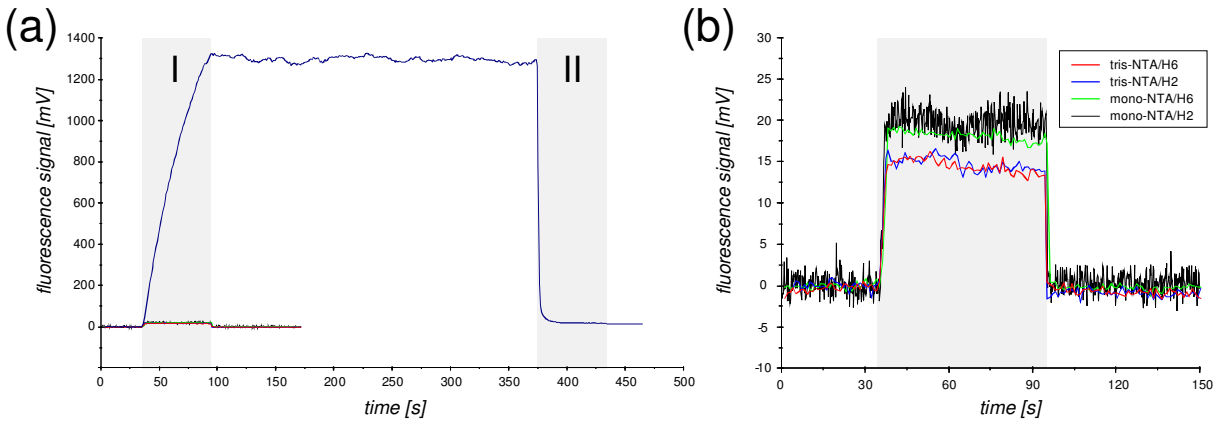

Figure S1 Specificity of H2 and H6 peptide binding. (a) Binding of H2 and H6 peptides to mono- and tris-NTA surfaces in absence of transition metal ions. For comparison, binding of H6 to tris-NTA surfaces after loading Ni(II) ions is shown. The grey bars mark the injections of the peptide (I) and imidazole for regeneration (II). (b) Zoom-up of the binding signals for H2 and H6 peptides showing only the background fluorescence during injection.

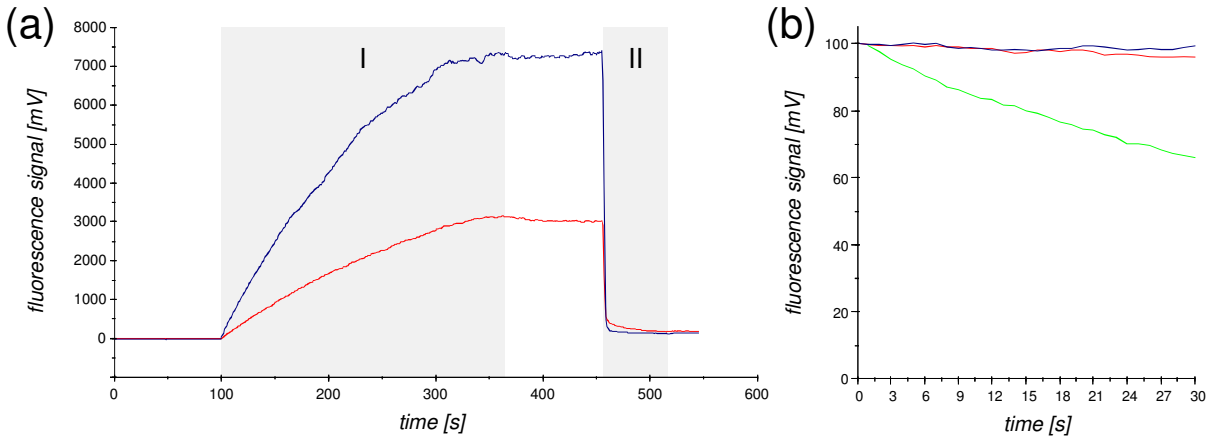

Figure S2 Surface concentration dependence of the mono-NTA/H6 interaction. (a) binding of H6 to PEG surfaces densely functionalized with tris-NTA (blue) and mono-NTA (red). The grey bars mark the injections of the peptide (I) and imidazole for surface regeneration (II). (b) Normalized fluorescence signals showing dissociation behaviour of H6-tags from dense mono-NTA and tris-NTA functionalized surfaces from (a) compared to the dissociation of H6 from diluted mono-NTA surfaces (green).

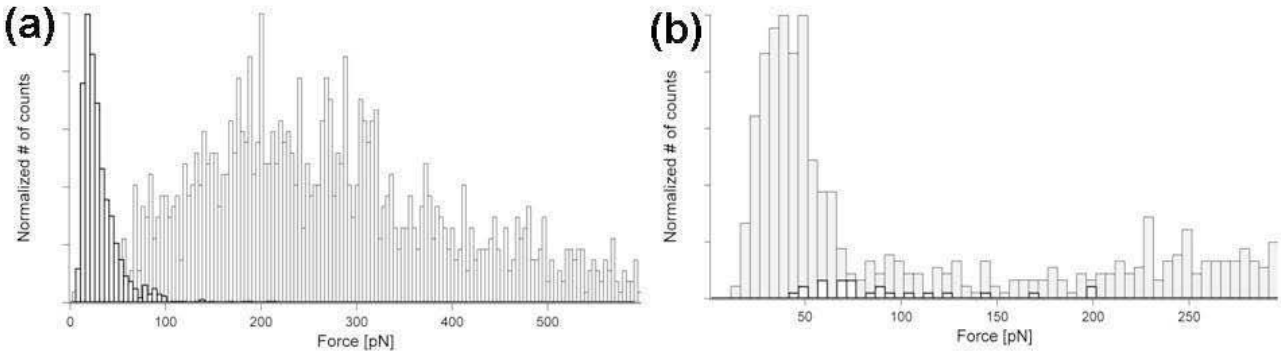

Figure S3 Control measurements of the specificity of the force spectroscopy measurements. (a) Normalized histograms of forces of rupture events between peptide labelled tips and PEG surfaces functionalized with mono-NTA for tips which are fully functionalized with H2 (thin bars) and tips with a diluted density of H2 (thick bars). (b) Histograms of forces of rupture events of mono-NTA/H6 measurements in HBS buffer (thin bars) and in HBS buffer containing 100 mM EDTA (thick bars).

References

(1) Lata, S.; Reichel, A.; Brock, R.; Tampe, R.; Piehler, J., *J. Am. Chem. Soc.*, **2005**, 127, 10205-10215.
(2) Lata, S.; Piehler, J., *Anal. Chem.*, **2005**, 77, 1096 -1105.
(3) Piehler, J.; Brecht, A.; Valiokas, R.; Liedberg, B.; Gauglitz, G., *Biosensors and Bioelectronics*, **2000**, 15, 473-481.
(4) Gavutis, M.; Lata, S.; Lamken, P.; Muller, P.; Piehler, J., *Biophys J.*, **2005**, 88, 4289-4302.
(5) Janissen, R., Oberbarnscheidt, L., Oesterhelt, F., *Colloids Surf. B. Biointerfaces*, **2009**, 71, 200-207.
(6) Butt, H.J., Jaschke, M., Ducker, *W. Bioelectrochem. Bioenerg.*, **1995**, 38, 191–201.
(7) Oesterhelt, F., Rief, M., Gaub, H. E., *New J. Phys.* **1999**, 1, 6.

Direct and Model Free Calculation of Force-Dependent Dissociation Rates from Force Spectroscopic Data

Leoni Oberbarnscheidt, Richard Janissen, and Filipp Oesterhelt*
Institute of Molecular Physical Chemistry, Heinrich-Heine University, Düsseldorf, Germany

ABSTRACT Force spectroscopy allows testing the free energy landscapes of molecular interactions. Usually, the dependency of the most probable rupture force on the force rate or the shape of the rupture force histogram is fitted with different models that contain approximations and basic assumptions. We present a simple and model free approach to extract the force-dependent dissociation rates directly from the force curve data. Simulations show that the dissociation rates at any force are given directly by the ratio of the number of detected rupture events to the time this force was acting on the bond. To calculate these total times of acting forces, all force curve data points of all curves measured are taken into account, which significantly increases the amount of information which is considered for data analysis compared to other methods. Moreover, by providing force-dependent dissociation rates this method allows direct testing and validating of any energy landscape model.

Received for publication 5 October 2008 and in final form 3 August 2009.

*Correspondence: filipp.oesterhelt@uni-duesseldorf.de

When the first single molecule force measurements were done, soon a debate came up why different groups got different rupture forces for the same receptor/ligand complex. On the basis of Bells formula (1), Evans et al. described the dependency of the holding force on the loading rate by the change of the interaction potential under a constant applied force (2). Here, the pulling force adds an energy term which is given by the product of the applied force times the distance x the ligand moves in direction of the pulling force, $f \times x$. Thus, the energy barrier of the binding potential is reduced by $f \times \Delta x$, where Δx is the width of the potential, i.e., the distance between its minimum and the maximum of the energy barrier. Assuming Δx to be independent of the force as a first approximation, the dissociation rate of such a complex under force load is given by

$$k_{\mathrm{diss}}(f) = \nu_0 \times \exp(-\Delta G(f)/k_{\mathrm{B}}T) = \nu_0 \times \exp(-(\Delta G_0 - f \times \Delta x)/k_{\mathrm{B}}T). \quad (1)$$

Here ν_0 is an attempt frequency and ΔG_0 is the height of the free energy barrier at zero force. In single molecule force spectroscopy the length of the molecular system is increased continuously until rupture occurs, detecting the applied force at the time of rupture. As the dissociation of the complex is governed by thermal fluctuations; neither the individual nor the average measured rupture forces are a characteristic parameter of the interaction. Pulling slowly leaves enough time for the system to dissociate at low forces whereas fast pulling increases the applied force to high values before the system had enough time to dissociate. The dependency of the most probable rupture force F on the force rate F^* by which the force is increased with time is described as (3)

$$F = k_{\mathrm{B}}T/\Delta x \times \ln(F^* \times \Delta x/(k_{\mathrm{B}}T \times k_{\mathrm{diss}})). \quad (2)$$

Thus, linear fitting the most probable rupture force versus the logarithm of the force rate reveals the dissociation rate at zero force k_0 and the width of the binding potential Δx. Formula 2 assumes that the applied force increases linear with time when pulling with a constant speed. However, this is not valid for anharmonic linkers which are used in single molecule force measurements.

Recently, attempts have been described which take the chain elasticity into account to derive a modified Bell-Evans formula (4,5). There, the elasticity of the polymer linker was taken into account describing them via the wormlike chain and the freely jointed chain models.

A more direct way to measure the force-dependent dissociation rates and to determine the potential width is known as the force-clamp technique. There, the force applied to the molecular system is held at a constant level while measuring the characteristic survival time of the bond. At a given constant force and the force-dependent rate k_{diss} the measured bond survival times follow an exponential decay. The probability to find the rupture after the time t_{i} is given by

$$P(t_i \mid k_{\mathrm{diss}}) = k_{\mathrm{diss}} \times \exp(-t_i \times k_{\mathrm{diss}}). \quad (3)$$

In this kind of constant force experiments $i = 1 \ldots N$ marks the ith measurement of the bond survival time.

The right side of Eq. 3 regarded as a function of k_{diss} for a given t_{i} is the likelihood function $L(k_{\mathrm{diss}}|t_{\mathrm{i}})$. The most likely rate in this case is given by $k_{\mathrm{diss}} = 1/t_{\mathrm{i}}$. The probability to find the N survival times $\{t_1 \ldots t_{\mathrm{N}}\}$ is given by the product

$$P(\{t_1 \ldots t_N\} \mid k_{\mathrm{diss}}) = \Pi_i P(t_i \mid k_{\mathrm{diss}}) = P(t_{\mathrm{av}} \mid k_{\mathrm{diss}})^N. \quad (4)$$

Editor: Peter Hinterdorfer.

doi: 10.1016/j.bpj.2009.08.015

Here $t_{av} = \Sigma t_i/N$ is the average measured survival time and N is the number of measured dissociation events at a given constant force f. The value $P(t_{av}|k_{diss})^N$ again has its maximum likelihood at $k_{diss} = 1/t_{av}$. Thus, instead of fitting the obtained survival times by a monoexponential decay, the most likely dissociation rate k_{diss} may be calculated directly from the average survival time $k_{diss} = N/\Sigma t_i$.

In fact, this can directly be calculated also from force spectroscopy data. When pulling on a molecular bond, each time window Δt having one data point of the pulling force curve may be regarded as an individual force-clamp experiment. As Δt is short compared to the bond survival time, the probability that the bond ruptures within this time window whereas the force f acts on the bond, is given by $k_{diss}(f) \times \Delta t$. Each time window in which a force f is applied to the bond under investigation may be regarded as an individual Poisson experiment which may result in either a rupture or no rupture. Since these Poisson experiments are completely independent of each other all data points that were taken at the same force may be merged and described as one Poisson experiment. Thus, the dissociation rate $k_{diss}(f)$ can be calculated as

$$k_{diss}(f) = N(f)/(M(f) \times \Delta t). \quad (5)$$

Here, $M(f)$ is the number of data points taken at the force f and $N(f)$ is the number of ruptures observed at this force. The product $M(f) \times \Delta t$ represents the total time of the force f acting on the bond. A similar result was obtained by Dudko et al. (6, Eq. 2). However, in contrast to the approach of Dudko et al., our method extracts the force-dependent off rates directly from the measured data and thus also includes the force noise.

To obtain the force-dependent dissociation rates all fluctuations of the applied force have to be taken into account, since the dissociation rates increase exponentially with the applied force. Therefore, it is important to calculate the forces which are truly acting on the molecular bond.

The fluctuations of the cantilever are driven by thermal noise of the whole system and do not reflect active pulling of the stretched polymer spacers due to its own length fluctuations. Assuming the polymer fluctuates much faster than the cantilevers resonance frequency, it may be regarded as being in the equilibrium state all the time and adapting its own length to the varying tip-surface distance, which fluctuates due to the Brownian motion of the cantilever. This prerequisite can be fulfilled by using short polymer spacers and by the fact that the stretched polymer is strongly restricted in its conformational space and slow diffusional components are reduced.

In the force curve displayed in Fig. 1 *a*, the bending of the cantilever toward the surface, as induced by pulling forces, is displayed as positive values. A bending toward the surface due to thermal fluctuations shows up in the force curve in the same way as a positive pulling force but, in fact, the length

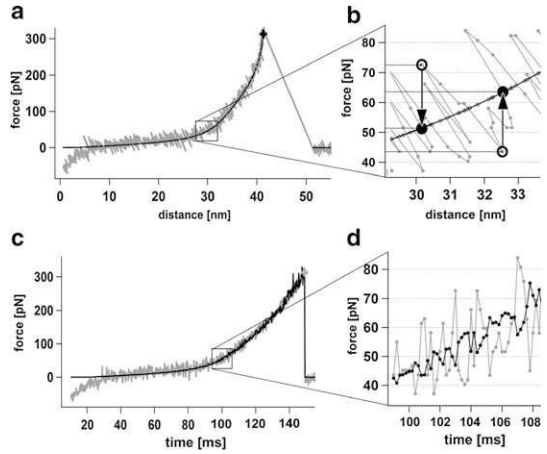

FIGURE 1 (*a*) Typical force curve of PEG (*gray*) fitted with the freely jointed chain plus two states model given in Oesterhelt et al. (7) (*black*). (*b*) Calculation of forces truly acting on the bond (*black*) from the cantilever fluctuations (*gray*). (*c*) The same force curve displayed versus time. The black curve shows the increasing noise in the truly acting forces. (*d*) Thermal fluctuation of the cantilever (*gray*) toward higher pulling forces corresponds with a reduced tip surface distance and thus a lower truly acting force (*black*).

of the polymer shortens in accordance with the reduced tip-surface distance. Thus, the stretching force acting on the polymer, which depends only on the polymers end-to-end distance, is reduced. Consequently, the actual force acting on the bond is given by the average force at the actual tip surface distance, i.e., by the vertical projection of each data point in the force curve onto a fit which describes the force derived from the average cantilever deflection (Fig. 1 *b*). Hence, to obtain the truly acting forces no model describing the polymer is explicitly required. Any curve that describes the average force can be used.

Fig. 1, *c* and *d*, show the same force curve displayed as force versus time (*gray*). The black curve shows the truly acting force calculated for each data point. The thermal noise visible in a force curve is high at low forces and decreases with increasing forces due to the stiffening of the stretched polymer. In contrast, the noise of the truly acting force is minimum at low forces increasing significantly with the applied force. This corroborates the importance of taking the true force fluctuations into account.

Thus, taking all data points from all measured force curves into account the force-dependent dissociation rates may directly be obtained from the rupture force distribution histogram and the histogram of durations of acting forces.

To test the method we applied it to simulated force spectroscopy data, which includes poly(ethylene glycol) (PEG) linkers, thermal noise, and a triangular binding potential, which fulfills the conditions of Bell's formula with a constant potential width $\Delta x = 0.3$ nm and a force-dependent binding energy $\Delta G(f) = \Delta G_0 - F \times \Delta x$ with $\Delta G_0 = 16\ k_BT$.

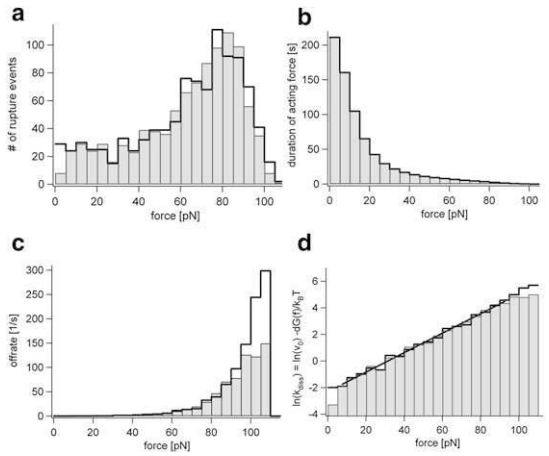

FIGURE 2 (*a*) Force histogram of ruptures of the simulated and analyzed data shown as black cityscape and gray histogram, respectively. (*b*) Total times of acting forces. (*c*) Calculated dissociation rates. (*d*) Logarithm of the dissociation rate which is a direct measure of force-dependent dissociation free energy $\ln(k_{diss}(f)) = \ln(\nu_0) - \Delta G(f)/k_B T$ with a linear fit to the analyzed values.

To generate the force curves we calculated, the forces according to the PEG fit model from Oesterhelt et al. (7), the cantilever deflection signal- and the force-dependent spring constant (slope) of the PEG polymer k_{pol} using the following parameters: data rate = 33 kHz, pulling speed = 100 nm/s, and contour length = 100 nm. Interestingly, the proposed method is independent of the experimental pulling speed, as long as the interaction is in the quasi-adiabatic state. With the spring constant of the cantilever $k_{cant} = 20$ pN/nm the spring constant of the combined system $k_{sys} = k_{pol} + k_{cant}$ was obtained and used to determine the root mean-square width $x = \mathrm{sqrt}(k_B T/k_{sys})$ for a Gaussian-distributed thermal noise, which then was added to the cantilever deflection. To simulate the rupture forces, we then applied the method described above to derive the truly acting forces from the simulated deflection data. Based on these forces a Monte Carlo approach was used to simulate the rupture point in each force curve based on the force-dependent off rate (Eq. 1) and an attempt frequency $\nu_0 = 10^6\ s^{-1}$.

We now applied the proposed analysis procedure to the simulated data. By dividing the number of rupture events counted at each force (Fig. 2 *a*) with the total time each force was applied for (Fig. 2 *b*) the force-dependent dissociation rates (Fig. 2 *c*) were calculated. Only small deviations are observed between the analyzed values (*gray histograms*) and the simulated data (*black cityscape*); the deviations result from the force detection limit (below 5 pN) or the fact that the force analysis procedure can detect only average rupture forces whereas the ruptures occur with higher probability at high force peaks (above 90 pN).

Interestingly, the force histogram (Fig. 2 *a*) is much broader than would be expected from a single force rate and reaches even as low as zero rupture forces. This reflects the different rates acting in the strongly nonharmonic PEG force curve (Fig. 1). However, the logarithm of the dissociation rates (Fig. 2 *d*, *line*) can be fitted by a straight line. The resulting fit parameters $k_0 = 0.121 \pm 0.01\ s^{-1}$ and $\Delta x = 0.301 \pm 0.006$ nm agree well with the parameters used in the simulation $k_0 = 0.113\ s^{-1}$ and $\Delta x = 0.3$ nm.

In conclusion, we want to point out that the approach presented here for deriving the force-dependent dissociation rates is completely model free. Thus, the shape of the force-dependent dissociation free energy (Fig. 2 *d*) calculated from the dissociation rates may directly be used for testing different energy landscape models.

ACKNOWLEDGMENTS

L.O. is a fellow of the North-Rhine-Westphalia Research School BioStruct. This work was supported by grants from the Ministry of Innovation, Science, Research and Technology of the German Federal State North-Rhine-Westphalia, from the Entrepreneur Foundation at the Heinrich-Heine-University of Düsseldorf, and by the BMBF nanotechnology competition, project No. 03N8714.

REFERENCES and FOOTNOTES

1. Bell, G. I. 1978. Models for the specific adhesion of cells to cells. *Science*. 200:618–627.
2. Evans, E., and K. Ritchie. 1997. Dynamic strength of molecular adhesion bonds. *Biophys. J*. 72:1541–1555.
3. Izrailev, S., S. Stepaniants, M. Balsera, Y. Oono, and K. Schulten. 1997. Molecular dynamics study of unbinding of the Avidin-Biotin complex. *Biophys. J*. 72:1568–1581.
4. Ray, C., J. R. Brown, and B. B. Akhremitchev. 2007. Correction of systematic errors in single-molecule force spectroscopy with polymeric tethers by atomic force microscopy. *J. Phys. Chem. B*. 111:1963–1974.
5. Evans, E., and K. Ritchie. 1999. Strength of a weak bond connecting flexible polymer chains. *Biophys. J*. 76:2439–2447.
6. Dudko, O. K., G. Hummer, and A. Szabo. 2008. Theory, analysis, and interpretation of single-molecule force spectroscopy experiments. *Proc. Natl. Acad. Sci. USA*. 105:15755–15760.
7. Oesterhelt, F., M. Rief, and H. E. Gaub. 1999. Single molecule force spectroscopy by AFM indicates helical structure of poly(ethylene-glycol) in water. *New J. Phys*. 1. 6.1–6.11.

doi:10.1016/j.jmb.2009.07.083 J. Mol. Biol. (2009) 394, 383–390

JMB

Available online at www.sciencedirect.com

ScienceDirect

ELSEVIER

Single-Molecule Force Spectroscopy Measures Structural Changes Induced by Light Activation and Transducer Binding in Sensory Rhodopsin II

Leoni Oberbarnscheidt[1], Richard Janissen[1], Swetlana Martell[2], Martin Engelhard[2] and Filipp Oesterhelt[1]*

[1]*Institut für molekulare physikalische Chemie, Universitätsstr. 1, 40225 Düsseldorf, Germany*

[2]*Max-Planck-Institut für molekulare Physiologie, Otto-Hahn-Str. 11, 44227 Dortmund, Germany*

Received 27 May 2009; received in revised form 27 July 2009; accepted 28 July 2009
Available online 3 August 2009

Edited by R. Huber

Microbial rhodopsins are a family of seven-helical transmembrane proteins containing retinal as chromophore. Sensory rhodopsin II (SRII) triggers two very different responses upon light excitation, depending on the presence or the absence of its cognate transducer HtrII: Whereas light activation of the *Np*SRII/*Np*HtrII complex activates a signalling cascade that initiates the photophobic response, *Np*SRII alone acts as a proton pump.

Using single-molecule force spectroscopy, we analysed the stability of *Np*SRII and its complex with the transducer in the dark and under illumination. By improving force spectroscopic data analysis, we were able to reveal the localisation of occurring forces within the protein chain with a resolution of about six amino acids. Distinct regions in helices G and F were affected differently, depending on the experimental conditions. The results are generally in line with previous data on the molecular stability of *Np*SRII. Interestingly, new interaction sites were identified upon light activation, whose functional importance is discussed in detail.

Keywords: sensory rhodopsin; atomic force microscopy; single-molecule force spectroscopy; membrane protein complex; protein unfolding

Introduction

Sensory rhodopsin II (SRII) is a member of the large family of microbial rhodopsins.[1,2] These type 1 rhodopsins are seven-α-helical transmembrane proteins that occur in all three domains of life. An all-*trans*-retinal covalently bound to the middle of the seventh helix absorbs light, and its resulting isomerisation to the 13-*cis* form induces different responses such as ion-pumping activity by bacteriorhodopsin and halorhodopsin or mediation of the phototactic response of sensory rhodopsins SRI and SRII in halophilic archaea in order to trigger phototaxis.

In microbial rhodopsins, the process of light activation includes the isomerisation of the retinal and rearrangements in the active site, finally leading to an outward movement of helix F.[2,3] The excitation, isomerisation and return to the all-trans state of retinal are organised in a photocycle comprising several intermediate states named K, L, M1, M2, N and O, which had been first described for the BR photocycle.[2,4,5] Complex conformational changes (especially of helix F) during the second part of the photocycle, which open the cytoplasmic channel and change the accessibility of the active side to enable ion pumping, have been described.[6]

Interestingly, *Np*SRII from *Natromonas pharaonis* has two distinct functions, depending on the presence of its cognate transducer *Np*HtrII. In the absence of the transducer, *Np*SRII acts as a proton pump,[7,8] although weaker than that of bacteriorhodopsin. In order to mediate phototaxis, *Np*SRII binds tightly to *Np*HtrII, which then activates a signalling cascade homologous to the two-component system of eubacterial chemotaxis.[9,10] The transducer consists of a transmembrane domain of two α-helices (TM1 and TM2), which binds to the receptor, and a large cytoplasmic domain, which is responsible for signal transfer.[3,11] Certain residues in helices F and G were identified to be crucial for both, transducer

*Corresponding author. E-mail address: Filipp.Oesterhelt@uni-duesseldorf.de.

Abbreviations used: SRII, sensory rhodopsin II; SMFS, single-molecule force spectroscopy; AFM, atomic force microscopy; WLC, worm-like chain; EPR, electron paramagnetic resonance; FRET, fluorescence resonance energy transfer.

binding and signal transfer.[12] However, there remain open questions and contradictory arguments about the exact movement of helix F, the possible involvement of a helix G movement and the precise molecular influence between SRII and its transducer.

We performed single-molecule force spectroscopy (SMFS) measurements on *Np*SRII, in the presence and in the absence of *Np*HtrII, and compared them to measurements in its inactive state in the dark and in the illuminated state. *Np*SRII is stable in dark and light, and it retains its native absorption spectrum and photocycle in different membranes.[13] We used the truncated form of the transducer $HtrII_{114}$, which allowed us to minimise the unwanted interaction of the transducer with the atomic force microscope (AFM) tip. This form lacks most of its cytoplasmic domain but interacts with *Np*SRII and is shown to be functional *in vitro*.[14]

In a previous SMFS study, unfolding of *Np*SRII has revealed a pattern similar to that observed in other archaeal rhodopsins[15–17] and has shown that binding of the transducer stabilises helices G and F. Here we present changes in stability upon light activation and their dependency on the presence of the transducer, which were obtained by an optimised SMFS data analysis. By taking the changes in the probability of peak occurrence as a measure for changes in protein stability, we are able to detect and localise structural changes that alter intramolecular and intermolecular bonds.

Results

SMFS of *Np*SRII

We determined the light-dependent reorganisation of interactions that stabilise structural regions of *Np*SRII and *Np*SRII bound to a truncated form of its transducer ($NpHtrII_{114}$) by applying SMFS, as described previously for *Np*SRII and other archaeal rhodopsins.[15–17] Briefly, force–distance measurements were performed on membrane patches with reconstituted *Np*SRII or *Np*SRII/*Np*HtrII, which were adsorbed on mica support. The tip was pushed into the membrane to allow an unspecific interaction between the tip and the C-terminus of the protein (as previously described by Oesterhelt *et al.*[15] and Muller *et al.*[18]). Retraction of the tip led to sequential unfolding of *Np*SRII, which was recorded by detecting the bending of the cantilever. For each force curve, the sample was shifted by 10 nm to ensure that *Np*SRII was always unfolded from an unperturbed part of the membrane. Force–distance traces showing successful unfolding were selected as described by Cisneros *et al.*[17]

The experiments were conducted first in the dark and then under exposure to blue light ($\lambda = 460$–500 nm). The intensity was chosen such that saturation occurs and about 25% of *Np*SRII is in its activated state (passing the M to O state).[2] A total of 103 and 87 force–distance curves for *Np*SRII alone and 94 and 103 force–distance curves for the *Np*SRII/$NpHtrII_{114}$ complex were collected in the dark and under blue light, respectively. The probability of peak occurrence in each data set was analysed separately and then compared to the others.

Peak positions reflect the localisation of intermolecular and intramolecular interactions

An overlay of the force curves shows the characteristic pattern of four main peaks (Fig. 1a), as already described for rhodopsins[15,19] and sensory rhodopsin in particular:[17] Each main peak represents the unfolding of an α-helix pair pulled out from the cytoplasmic side.[15] Additionally, most force curves reveal further side peaks representing unfolding intermediates and alternative unfolding pathways (Fig. 1b) that differ depending on the experimental condition.[16–19]

Each force peak detected an individual force–distance curve was fitted using the worm-like chain (WLC) model with a fixed persistence length of 0.4 nm, which is known to fit an unfolded amino acid chain[18] well above 50 pN. The contour length, as derived from the WLC fit, can be converted into the number of stretched amino acids, giving the unfolded portion of the polypeptide chain and thus elucidates the remaining intermediate structure.

However, the contour length derived from the WLC fit only reflects that part of the unfolded peptide chain that ranges from the tip to the upper surface of the membrane and neglects the part inside the membrane.[15,18] If rupture occurs inside the membrane, we have to correct for the complete chain length and thus calculate the expected measured lengths for all amino acids according to their *z*-positions in the crystal structure (Protein Data Bank ID 1H2S).[20]

Average shifted histograms with varying bin widths allow higher resolution in peak occurrence probabilities

To visualise the peak occurrence probabilities, the fitted rupture lengths are usually displayed as standard histograms. However, the shape of standard histograms significantly depends on the bin width and the chosen starting point, especially at an overall low number of counts. To avoid artefacts due to an arbitrarily chosen starting point and to accurately reflect the density of rupture lengths measured with SMFS, we displayed the rupture lengths data as an average shifted histogram.[21] In the case of monomodal data distribution, an optimal histogram bin width may be calculated from the standard deviation of the data.[22–24] However, the length distributions obtained from protein unfolding experiments are always multimodal. Thus, we extended the average shifted histogram to variable bin widths that were selected such that 20 events were collected per bin. This kept noise at a level that allowed the comparison of various data sets also at rupture lengths where only a low number of events were detected. The heights of the histogram bins in

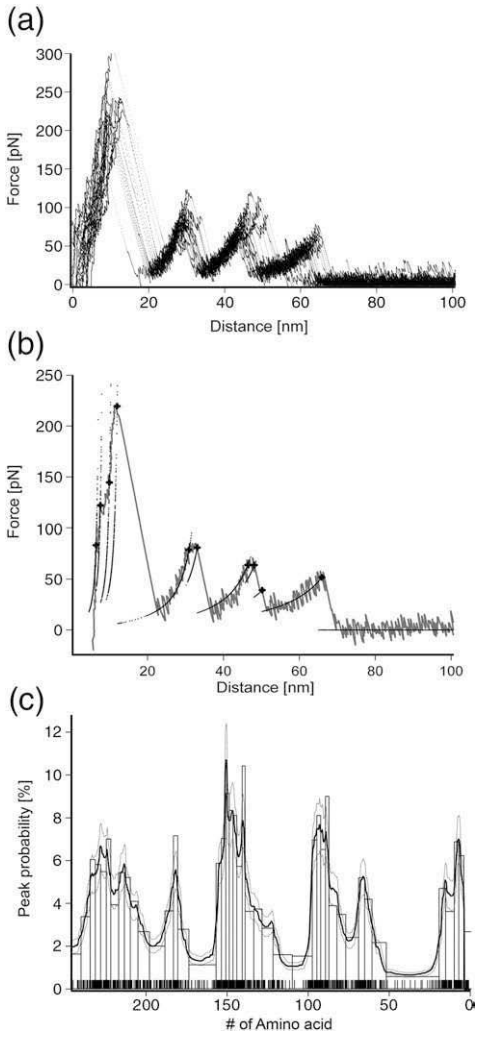

Fig. 1. Illustration of the force curve analysis procedure. (a) Overlaid force curves measured on *Np*SRII alone in the dark. The data are displayed as a dot plot. (b) Single force curve. The rupture force peaks (crosses) were detected by searching for minima in the smoothed derivative of the force curve. The left-hand sides of the force peaks were fitted with the WLC model (dotted black line) (monomer length = 3.6 Å; persistence length = 4.0 Å) to obtain the corresponding chain lengths. (c) Histogram showing the peak frequency of the monomer lengths derived from the WLC fit (bars; 1 bar = 20 events). An "average shifted histogram," which is created by shifting the starting point of the binnings in steps of one (black line), is overlaid. The errors were estimated by assuming a Poisson distribution (dotted black line). Raw data (i.e., individual fitted chain lengths of the rupture event) are shown as sticks below the histogram.

Fig. 1c were calculated such that the area of each bin was normalised to the constant number of 20 counts per bin.

To estimate the errors of a given number of force peaks at a fixed length the standard deviation of the respective probability distribution was calculated. With the assumption of a fixed probability to detect an unfolding event of a length within a given range, the probability to obtain any number of events from the whole data set is given by a Poisson distribution. Therefore, the error bars can be estimated as the square root of the number of detected events per bin (estimated error limits in Fig. 1c).

The force peak histograms (Fig. 1c) show the typical pattern of the unfolding of archaeal rhodopsins, as previously described by Cisneros *et al.*[17] The unfolding of an α-helix pair can be traced in the four main peaks. Additionally, the average shifted histograms give a more detailed picture of the unfolding of smaller substructures, which is revealed in multisubpeaks.

SMFS reveals manifold changes of interactions in helices F and G upon light excitation

To quantify the change in peak probability between the four experimental conditions, we calculated the difference curves between *Np*SRII and *Np*SRII/*Np*HtrII, between *Np*SRII and *Np*SRII$_{light}$, and between *Np*SRII/*Np*HtrII and *Np*SRII/*Np*HtrII$_{light}$ (Fig. 2a–c, lower curves) after having normalised each average shifted histogram on the respective number of measured force curves.

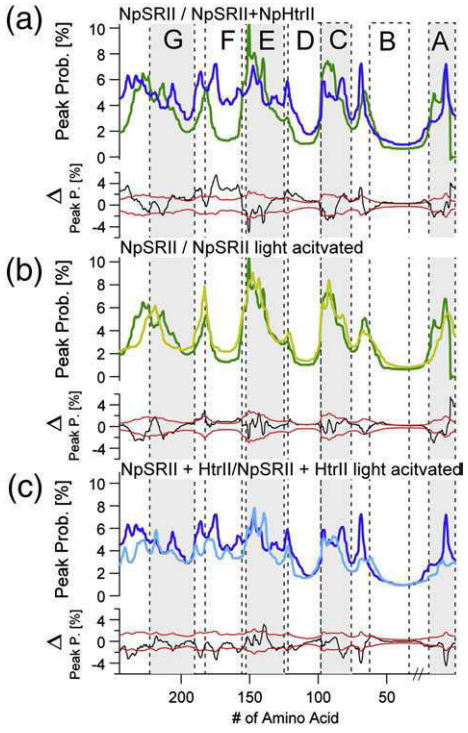

Fig. 2. Peak occurrence probabilities for the unfolding of *Np*SRII. (a) Comparison of the unfolding of *Np*SRII alone (green) and in complex with its transducer *Np*HtrII (blue). (b) Comparing the unfolding of *Np*SRII in dark (dark green) and in the light-activated state (light green). (c) Comparing the unfolding of the *Np*SRII/*Np*HtrII complex in the dark (dark blue) and in the light-activated state (light blue). Under the curves, the differences of the respective peak occurrence probabilities are plotted as black lines, whereas the estimated errors of the curves are shown in red. The vertical dotted lines indicate the range of transmembrane α-helices (Protein Data Bank ID 1H2S).

Since both data sets have errors, 1σ errors (68.3%) for comparing the two data sets (estimated error limits in Figs. 2 and 3) can be calculated by error propagation as the square root of the sum of both squared standard deviations. They give the error limits above or below which changes in the peak occurrence frequency between the different data sets may be regarded as significant, indicating a structural change in the protein.

Under all four experimental conditions, *Np*SRII exhibits different probabilities for force peak detection (Fig. 2). As already known from SMFS experiments on other α-helical membrane proteins in the absence of the transducer, the strongest peak occurrence probability is observed at the onset of the helices with respect to the pulling direction. This is changed upon transducer binding, where an increase in the peak occurrence probability is observed in the second half of the helices, reflecting a stabilising effect of the transducer. Also, light activation shows distinct changes in stabilising interactions. However, they are smaller than those induced upon transducer binding, which may also be due to the fact that only about 25% of illuminated proteins are in their activated state. Interestingly, light-induced changes observed in the presence of the transducer are stronger than those observed in its absence.

Of special interest are the first peaks, which reflect structural changes occurring in helices F and G, since these are involved in both, transducer binding and formation of the intramolecular hydrogen bond network, which plays an important role in proton transfer in the absence of the transducer.[2] The superposition of peak probability histograms for helices G and F is shown in Fig. 3 and reveals similarities and differences between all four data sets: Light activation and transducer binding, in *Np*SRII alone and in complex, lead to a decrease in rupture events in helix G (Fig. 3, region 2) and in the C-terminus. Regarding the receptor alone, light activation and transducer binding lead to a decrease in the middle of helix G (Fig. 3, region 1) and an increase in the loop region (Fig. 3, region 4). The only region where changes occur upon *Np*HtrII binding but not upon light activation is the extracellular part of helix G (Fig. 3a, region 3), where the peak probability decreases. While almost no rupture event was measured in helix F in the absence of the transducer, rupture events occurred almost as frequently as in the extracellular side of helix G in the presence of the transducer (Fig. 3, region 5). However, upon light activation, the number of rupture events again decreases in regions of helix F (Fig. 3, regions 5A and 5B). Altogether, these results reveal complex changes in localised stabilising interactions upon

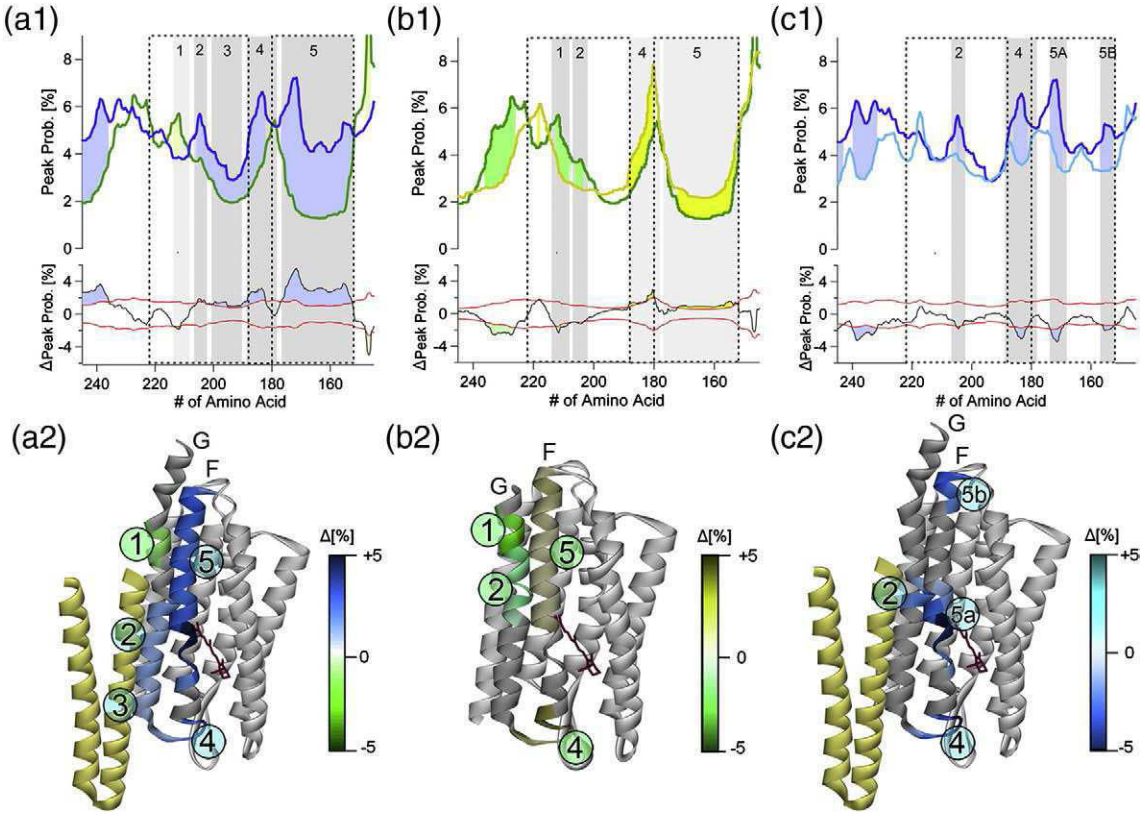

Fig. 3. Zoom to the peak occurrence probabilities in helices G and F. (a1–c1) A zoom to the peak occurrence probabilities in helices G and F, as shown in Fig. 2 (same colour code used). (a2–c2) The respective localisation of significant changes in the crystal structure (Protein Data Bank ID 1H2S). The colour code next to the crystal structure indicates the strength of the change in stabilisation of the respective regions.

light activation, which are again modulated by the presence of the transducer.

Discussion

Advanced SMFS data analysis

*Np*SRII has already been well studied, but there remain some open questions concerning the tilt of helix F and details about the signal transfer between receptor and transducer (reviewed by Klare *et al.*[2]). In contrast to many techniques which require *Np*SRII to be in solution to investigate its structure–function relationship, we are able to study the interactions of wild-type *Np*SRII inside the membrane using AFM. Thus, we avoid artefacts due to the influence of artificial solubilisation.[25]

Former AFM studies on membrane proteins, especially rhodopsins, revealed their unfolding pathways from which a high level of homology of their structural elements could be concluded.[15,18] As previously shown, the unfolding pattern of *Np*SRII is similar to those of other archaeal rhodopsins.[17] In this previous study, ensemble averaged forces were calculated by multiplying the frequency of rupture events with their respective rupture forces, revealing a partial stabilisation of helices G and F upon transducer binding. Here, we present changes upon light activation and introduce an improved force curve analysis (which allows us to achieve a more detailed view of the interaction pattern alone from the rupture frequency) not requiring ensemble average calculation.

As known from the crystal structure,[20] helices G and F are in close proximity to *Np*HtrII. Thus, in our analysis, we concentrated on changes in the stability of helices F and G, which reflect direct interactions with the transducer. By applying our data analysis procedure to the SRII unfolding data, we could reveal five different regions within helices G and F which responded independently to transducer binding and light induction.

Conformational answer after light activation varies with transducer binding

Upon transducer binding, we observe a loss of stabilising interactions in the cytoplasmic half of helix G (Fig. 3a, region 1; Table 1). In contrast, stabilisation is found in the F-G loop (region 4), the extracellular half of helix G (regions 2 and 3) and throughout helix F (region 5). A comparison with crystallographic data[20] reveals that the hydrogen bonds between *Np*SRII and *Np*HtrII existing in these regions may contribute to the observed stabilisations. Thr189 (end of F-G loop) is reported to bind to Glu43 (TM1) and Ser62 (TM2), and Tyr199 (extracellular half of helix G) is reported to bind to Asn74 (TM2). In addition, electron paramagnetic resonance (EPR), isothermal titration calorimetry and fluorescence resonance energy transfer (FRET)[26–28] revealed an interaction of the cytoplasmic side of helix F with the cytoplasmic extension of the transducer, which was not resolved in the crystal structure.

The regions identified here only on the basis of the peak occurrence probability necessarily differ from those identified on the basis of calculated ensemble forces.[17] The probability of peak occurrence, which reflects the probability that a specific interaction exists at the distinct moment, depends on the corresponding on-rate and off-rate. In contrast, the measured forces depend on the off-rate and the width of the binding potential and thus reflect different characteristics of molecular interactions.

To address the molecular changes upon light activation, we compare the light-induced stabilisation or destabilisation of the protein depending on the presence and the absence of the transducer. We find changes in stability that are independent of transducer binding, as well as those that are dependent on it.

Independent of *Np*HtrII binding, light activation always decreases the molecular stability in region 2 in the middle of helix G. This region harbours the retinal-binding site and includes amino acids Lys205 and Asp201, which form hydrogen bonds with the central water cluster, as shown by the crystal structure of the *Np*SRII/*Np*HtrII complex.[29] The structure of the M state revealed that these bonds are broken upon light excitation. This is in good agreement with the decrease in stability observed for this region.

In contrast, in all other regions, conformational changes upon light activation are modulated by the binding of the transducer. In the cytoplasmic half of helix G (region 1), light activation induces destabilisation of *Np*SRII alone, while no change is observed in the *Np*SRII/*Np*HtrII complex. Considering the literature, quite contradictory results are presented for this region. EPR measurements have shown an increase in the mobilisation of a spin-labelled side

Table 1. Overview of changes in interactions in helices G and F upon light activation

Region	Helix	Number of amino acids from the C-terminus	Number of amino acids from the N-terminus	Transducer binding	Light activation in receptor	Light activation in complex
1	G	31–37	208–214	−	−	
2	G	38–43	202–207	+	−	−
3	G	44–55	190–201	+		
4	G-F loop	56–67	178–189	+	+	−
5	F	68–93	177–152	+	+	
5A	F	71–77	168–174	+	+	−
5B	F	88–93	152–157	+	+	−

An increase in a region with interactions is indicated with (+), whereas a decrease in a region with interactions is indicated with (−).

chain between helices F and G upon light activation for *Np*SRII alone and in complex,[30] indicating an increase in the distance of helices G and F. In contradiction, the crystal structure of the light-activated receptor in its M state shows that helices F and G are stabilised by a hydrogen bond between Asp214 (helix G) and Arg162 (helix F).[29]

In all other regions in which light activation shows an effect on stability (regions 4, 5A and 5B), transducer binding causes the inversion of the observed effect. Light activation and transducer binding alone lead to an increase in stabilisation. Interestingly, light activation in the presence of the transducer reduces the strong stabilisation that has been induced by transducer binding. However, results from FRET and EPR measurements show a close proximity of the EF loop and transducer helix TM2, which is increased upon light activation.[26,28]

Force spectroscopy data reveal new locations of structural changes upon light excitation

The mechanism of signal transduction upon light activation, as generally discussed, includes isomerisation of the retinal, outward movement of the cytoplasmic half of helix F and clockwise rotation of the transducer helix TM2.[2] This model is based on FRET,[28] Fourier transform infrared[31] spectroscopy, EPR[26,30] spectroscopy, isothermal titration calorimetry[27] and molecular dynamics simulations.[32] However, a different structural rearrangement was found in the crystal structure of the excited state.[29]

After light absorption, the retinal isomerises, and the water cluster next to the retinal binding in the extracellular part of the channel is reorganised. This is likely to be the reason for the reduced stability observed in region 2; as expected, it is found both, in the presence and in the absence of the transducer.

The crystal structure revealed a hydrogen bond between Thr204 in region 2 and Tyr174 in helix F in region 5A that is described to be crucial for signalling.[33] Interestingly, in the complex, light activation strongly decreases the stability in region 5A, which harbours the retinal-binding pocket and is adjacent to region 2 (Fig. 3c). However, this decrease is not due to a loss of interaction with helix G, as this helix is already unfolded at this point of the measurement. While hardly any stable unfolding intermediates are observed in region 5 in *Np*SRII alone, transducer binding strongly stabilises this region. Thus, it is likely that the decrease observed in region 5A upon light activation is due to a weaker binding between this region of helix F and the transducer helix TM2. Other measurements revealed an increased dissociation constant of the light-activated protein complex,[34] which our data might assign to a weakening of binding in this region. We observe a similar decrease in stability in the loop regions of helix F (regions 4 and 5B). Since the crystal structure does not resolve any interactions between the cytoplasmic end of helix F and TM2, it is likely that the stabilisation we have observed upon complex formation is a result of intramolecular interactions that are induced by transducer binding. Intramolecular rearrangements upon light activation, as revealed by EPR measurements, might explain the decrease in interactions in region 5B, as observed in our experiment. Interestingly, in regions 4, 5A and 5B, we observe an inverse behaviour upon light activation when the transducer is absent; here, a slight increase indicating intramolecular stabilisation is found upon light activation. Destabilising effects are observed at the cytoplasmic half of helix G upon light activation (region 1) only in the absence of the transducer, but not in the complex. This might be responsible for the opening of the cytoplasmic cleft, which allows the proton-pumping activity of this protein.[35] That this effect is not observed when *Np*HtrII is bound might be another indication to explain its proton-pumping inhibition.[6,7,27]

The presented differences in intermolecular and intramolecular interactions, which depend on the presence of the transducer, highlight important regions in the protein that are responsible for the completely different response after light activation. Due to the analysed distributions being multimodal, standard histogram would give a low accuracy on the localisation of these differences. Only the application of average shifted histograms to force spectroscopic data allows us to increase the accuracy to a resolution of about six amino acids. However, some changes in peak occurrence probability are close to the estimated 1σ error limit of 68%. Interestingly, regions that have not been described before to show conformational changes upon light activation (regions 5A and 5B) are clearly above the error limits, while regions with changes close to the error limits point to conformational changes that have been described already with other biophysical methods. Most of the observed changes in stability are in good agreement with previously published results obtained with different biophysical methods. The additionally identified regions might be very interesting for further investigations using other techniques.

Experimental Procedures

Sample preparation

*Np*SRII and *Np*HtrII$_{114}$ from *N. pharaonis* were overexpressed as His-tagged proteins in *Escherichia coli* and purified by affinity chromatography using a Ni-NTA agarose column (QIAGEN, Hilden, Germany). *Np*SRII was then reconstituted into purple membrane lipids with a 1:35 (wt/wt) protein-to-lipid ratio.[36] *Np*SRII/*Np*HtrII$_{114}$ complexes were prepared by mixing *Np*SRII and *Np*HtrII$_{114}$ at a ratio of 1:1, followed by reconstitution into lipids.[14]

Force measurements

Force–distance measurements were performed in 20 mM Tris–HCl and 300 mM NaCl (pH 7.8) on membrane patches with reconstituted *Np*SRII or *Np*SRII/*Np*HtrII,

which were adsorbed on mica support. To activate the protein, we illuminated the sample with blue light using a high-intensity arc lamp with a filter of $\lambda = 460–500$ nm and 290 $\mu W/cm^2$.

The tip was pushed into the sample with a force of ~200 pN to allow coupling of the C-terminus of *Np*SRII (as previously described[15,18]) and was retracted with 400 nm/s. Cantilever deflection was recorded over the distance with a sampling rate of 33 kHz.

Si_3N_4 cantilevers (spring constant, 20 pN/nm; model OMCL TR400; Olympus) were used, and the spring constant was determined using the equipartition theorem.[37]

To couple the C-terminus to the tip, we took advantage of unspecific interactions. Since the C-terminus has 23 amino acids outside the membrane while the N-terminus is embedded in the membrane, the probability of attaching the tip to the N-terminal end is negligible. Thus, it is assured that we unfold only those *Np*SRII that are oriented with the C-terminus on the upper side.[17]

To include only those curves where *Np*SRII was attached with the terminus towards the tip, we selected the longest force curves (>60 nm) in accordance with the criteria described by Oesterhelt *et al.*[15] and Cisneros *et al.*[17] Under each condition (light/dark, presence/absence of HtrII), ~100 curves were taken into account for further analysis.

Data analysis

Selected force curves were analysed by fitting each force peak to the WLC model with a monomer length of 3.6 Å and a persistence length of 4.0 Å[15,38] using self-written procedures in IGOR.

The WLC model with a persistence length of 4 Å fits unfolded amino acid chains best above forces of 50 pN. At lower forces, as measured for the unfolding of the last helix, this model overestimates the chain length. However, this effect is negligible at the unfolding of helices G and F. To eliminate chain length variations that originate from a randomly varying anchoring point within the C-terminus, we aligned all curves by superposing on the second and third force peaks.

Acknowledgements

L.O. is a fellow of the North Rhine-Westphalia Research School BioStruct. This work was supported by grants from the Ministry of Innovation, Science, Research and Technology of the German Federal State North Rhine-Westphalia and from the Entrepreneur Foundation at the Heinrich-Heine-Universität Düsseldorf.

References

1. Sharma, A. K., Spudich, J. L. & Doolittle, W. F. (2006). Microbial rhodopsins: functional versatility and genetic mobility. *Trends Microbiol.* **14**, 463–469.
2. Klare, J. P., Chizhov, I. & Engelhard, M. (2008). Microbial rhodopsins: scaffolds for ion pumps, channels, and sensors. *Results Probl. Cell Differ.* **45**, 73–122.
3. Klare, J. P., Gordeliy, V. I., Labahn, J., Buldt, G., Steinhoff, H. -J. & Engelhard, M. (2004). The archaeal sensory rhodopsin II/transducer complex: a model for transmembrane signal transfer. *FEBS Lett.* **564**, 219–224.
4. Haupts, U., Tittor, J., Bamberg, E. & Oesterhelt, D. (1997). General concept for ion translocation by halobacterial retinal proteins: the isomerization/switch/transfer (IST) model. *Biochemistry*, **7**, 2–7.
5. Haupts, U., Tittor, J. & Oesterhelt, D. (1999). Closing in on bacteriorhodopsin: progress in understanding the molecule. *Annu. Rev. Biophys. Biomol. Struct.* **28**, 367–399.
6. Spudich, J. L. (1998). Variations on a molecular switch: transport and sensory signalling by archaeal rhodopsins. *Mol. Microbiol.* **28**, 1051–1058.
7. Schmies, G., Engelhard, M., Wood, P. G., Nagel, G. & Bamberg, E. (2001). Electrophysiological characterization of specific interactions between bacterial sensory rhodopsins and their transducers. *Proc. Natl Acad. Sci. USA*, **98**, 1555–1559.
8. Sudo, Y., Iwamoto, M., Shimono, K., Sumi, M. & Kamo, N. (2001). Photo-induced proton transport of pharaonis phoborhodopsin (sensory rhodopsin II) is ceased by association with the transducer. *Biophys. J.* **80**, 916–922.
9. Rudolph, J. & Oesterhelt, D. (1995). Chemotaxis and phototaxis require a CheA histidine kinase in the archaeon *Halobacterium salinarium*. *EMBO J.* **14**, 667–673.
10. Rudolph, J. & Oesterhelt, D. (1996). Deletion analysis of the che operon in the archaeon *Halobacterium salinarium*. *J. Mol. Biol.* **258**, 548–554.
11. Spudich, J. L. (2006). The multitalented microbial sensory rhodopsins. *Trends Microbiol.* **14**, 480–487.
12. Sudo, Y. & Spudich, J. L. (2006). Three strategically placed hydrogen-bonding residues convert a proton pump into a sensory receptor. *Proc. Natl Acad. Sci.* **103**, 16129–16134.
13. Spudich, J. L. & Luecke, H. (2002). Sensory rhodopsin II: functional insights from structure. *Curr. Opin. Struct. Biol.* **12**, 540–546.
14. Wegener, A. A., Klare, J. P., Engelhard, M. & Steinhoff, H. J. (2001). Structural insights into the early steps of receptor–transducer signal transfer in archaeal phototaxis. *EMBO J.* **20**, 5312–5319.
15. Oesterhelt, F., Oesterhelt, D., Pfeiffer, M., Engel, A., Gaub, H. E. & Müller, D. J. (2000). Unfolding pathways of individual bacteriorhodopsins. *Science*, **288**, 143–146.
16. Kedrov, A., Janovjak, H., Sapra, K. T. & Muller, D. J. (2007). Deciphering molecular interactions of native membrane proteins by single-molecule force spectroscopy. *Annu. Rev. Biophys. Biomol. Struct.* **36**, 233–260.
17. Cisneros, D. A., Oberbarnscheidt, L., Pannier, A., Klare, J. P., Helenius, J., Engelhard, M. *et al.* (2008). Transducer binding establishes localized interactions to tune sensory rhodopsin II. *Structure*, **16**, 1206–1213.
18. Muller, D. J., Kessler, M., Oesterhelt, F., Moller, C., Oesterhelt, D. & Gaub, H. (2002). Stability of bacteriorhodopsin alpha-helices and loops analyzed by single-molecule force spectroscopy. *Biophys. J.* **83**, 3578–3588.
19. Janovjak, H., Kedrov, A., Cisneros, D. A., Sapra, K. T., Struckmeier, J. & Muller, D. J. (2006). Imaging and detecting molecular interactions of single transmembrane proteins. *Neurobiol. Aging*, **27**, 546–561.
20. Gordeliy, V. I., Labahn, J., Moukhametzianov, R., Efremov, R., Granzin, J., Schlesinger, R. *et al.* (2002).

Molecular basis of transmembrane signalling by sensory rhodopsin II–transducer complex. *Nature*, **419**, 484–487.
21. Scott, D. (1992). *Multivariate Density Estimation.* John Wiley, New York.
22. Scott, D. W. (1979). On optimal and data-based histograms. *Biometrika*, **66**, 605–610.
23. Freedman, D. & Diaconis, P. (1981). On the histogram as a density estimator: L2 theory. *Z. Wahrscheinlichkeitstheor. Verw. Geb.* **57**, 453–476.
24. Izenman, A. J. (1991). Recent development in nonparametric density estimation. *J. Am. Stat. Assoc.* **86**, 205–224.
25. Klare, J. P., Bordignon, E., Doebber, M., Fitter, J., Kriegsmann, J., Chizhov, I. *et al.* (2006). Effects of solubilization on the structure and function of the sensory rhodopsin II/transducer complex. *J. Mol. Biol.* **356**, 1207–1221.
26. Wegener, A. -A., Chizhov, I., Engelhard, M. & Steinhoff, H. -J. (2000). Time-resolved detection of transient movement of helix F in spin-labelled pharaonis sensory rhodopsin II. *J. Mol. Biol.* **301**, 881–891.
27. Hippler-Mreyen, S., Klare, J. P., Wegener, A. A., Seidel, R., Herrmann, C., Schmies, G. *et al.* (2003). Probing the sensory rhodopsin II binding domain of its cognate transducer by calorimetry and electrophysiology. *J. Mol. Biol.* **330**, 1203–1213.
28. Yang, C. -S., Sineshchekov, O., Spudich, E. N. & Spudich, J. L. (2004). The cytoplasmic membrane-proximal domain of the HtrII transducer interacts with the E-F loop of photoactivated *Natronomonas pharaonis* sensory rhodopsin II. *J. Biol. Chem.* **279**, 42970–42976.
29. Moukhametzianov, R., Klare, J. P., Efremov, R., Baeken, C., Göppner, A., Labahn, J. *et al.* (2006). Development of the signal in sensory rhodopsin and its transfer to the cognate transducer. *Nature*, **440**, 115–119.
30. Bordignon, E., Klare, J. P., Holterhues, J., Martell, S., Krasnaberski, A., Engelhard, M. & Steinhoff, H. -J. (2007). Analysis of light-induced conformational changes of *Natronomonas pharaonis* sensory rhodopsin II by time resolved electron paramagnetic resonance spectroscopy. *Photochem. Photobiol.* **83**, 263–272.
31. Kamada, K., Furutani, Y., Sudo, Y., Kamo, N. & Kandori, H. (2006). Temperature-dependent interactions between photoactivated pharaonis phoborhodopsin and its transducer. *Biochemistry*, **45**, 4859–4866.
32. Inoue, K., Sasaki, J., Spudich, J. L. & Terazima, M. (2008). Signal transmission through the HtrII transducer alters the interaction of two alpha-helices in the HAMP domain. *J. Mol. Biol.* **29**, 963–970.
33. Sudo, Y., Furutani, Y., Kandori, H. & Spudich, J. L. (2006). Functional importance of the interhelical hydrogen bond between Thr204 and Tyr174 of sensory rhodopsin II and its alteration during the signaling process. *J. Biol. Chem.* **281**, 34239–34245.
34. Sudo, Y., Iwamoto, M., Shimono, K. & Kamo, N. (2001). Pharaonis phoborhodopsin binds to its cognate truncated transducer even in the presence of a detergent with a 1:1 stoichiometry. *Photochem. Photobiol.* **74**, 489–494.
35. Schmies, G., Luttenberg, B., Chizhov, I., Engelhard, M., Becker, A. & Bamberg, E. (2000). Sensory rhodopsin II from the haloalkaliphilic *Natronobacterium pharaonis*: light-activated proton transfer reactions. *Biophys. J.* **78**, 967–976.
36. Hohenfeld, I. P., Wegener, A. A. & Engelhard, M. (1999). Purification of histidine tagged bacteriorhodopsin, pharaonis halorhodopsin and pharaonis sensory rhodopsin II functionally expressed in *Escherichia coli*. *FEBS Lett.* **442**, 198–202.
37. Butt, H. J., Jaschke, M. & Ducker, W. (1995). Measuring surface forces in aqueous electrolyte solution with the atomic force microscope. *Bioelectrochem. Bioenerg.* **38**, 191–201.
38. Rief, M., Gautel, M., Oesterhelt, F., Fernandez, J. M. & Gaub, H. E. (1997). Reversible unfolding of individual titin immunoglobulin domains by AFM. *Science*, **276**, 1109–1112.

Colloids and Surfaces B: Biointerfaces 71 (2009) 200–207

Contents lists available at ScienceDirect

Colloids and Surfaces B: Biointerfaces

journal homepage: www.elsevier.com/locate/colsurfb

Optimized straight forward procedure for covalent surface immobilization of different biomolecules for single molecule applications

Richard Janissen, Leoni Oberbarnscheidt, Filipp Oesterhelt*

Institute of Physical Chemistry II, Heinrich-Heine University, Universitätsstrasse 1, 40225 Düsseldorf, Germany

ARTICLE INFO

Article history:
Received 29 October 2008
Received in revised form 5 February 2009
Accepted 10 February 2009
Available online 21 February 2009

Keywords:
Surface chemistry
Protein immobilization
DNA immobilization
Peptide immobilization
Atomic force microscopy

ABSTRACT

Covalent chemisorption of biomolecules to surfaces with high density and low unspecific background is prerequisite for most optical and mechanical single molecule experiments and accordingly, many recipes have been developed. However, new establishment of the surface functionalization process in the lab usually is still difficult and time consuming due to the complex procedures containing many pitfalls. Therefore, based on the known recipes, we developed and optimized a simple straight forward protocol. We demonstrated it resulting in a high density of the coupled biomolecules, homogeneous surfaces and a low unspecific background when binding nucleic acids, peptides and proteins.

The protocol was optimized for borosilicate cover glasses and silicon nitride atomic force microscope cantilevers commonly used in single molecule experiments and takes advantage of commonly used chemicals. It consists of only four steps, silanol group generation, amination, grafting of poly(ethylene glycol) to the surface and biomolecule coupling. All individual steps were optimized comparing different variations partially described in the literature. Finally, a detailed description is provided which allows avoiding most sources of contamination, often being a main hurdle on the way to single molecule experiments.

1. Introduction

Due to the exceptional sensitivity of single molecule detection and its ability to detect unique events in an ensemble of molecules it presents a huge potential for the study of biorecognition processes. The development of biosensors and supports with conjugated biomolecules has important applications in areas such as environmental science and biomedical research.

However, due to problems associated with the sensitivity, reproducibility, long-term stability, and non-specific binding of biomolecules to surfaces, biosensors for DNA, peptides and proteins are not widely available from commercial sources. In order to circumvent these problems new approaches have to be developed to create biosensors with high chemical stability, high reproducibility and fewer non-specific surface adsorption artefacts.

Attachment of DNA, peptides and proteins to a solid support is of great interest for biotechnological, molecular biological and sensitive diagnostic applications. Different solid supports, such as glass, silicon, silicon nitride, magnetic beads and polymers are used for single molecule application studies. Different immobilization methods, including entrapment, adsorption and chemical binding are applied to couple different biomolecules both covalently and non-covalently to surfaces. Due to the high background resulting from non-specific adsorption with non-covalent immobilization methods, covalent immobilization which selectively links biomolecule probes to solid supports is the method of choice for single molecule applications.

To allow easy access to bio-functionalized surfaces we developed a simple straight forward protocol for coupling different biomolecules (DNA, peptides and proteins) to silicon nitride AFM tips and borosilicate glasses with different biomolecules (DNA, peptides and proteins) in only three steps (Fig. 1): (i) generation of amino groups as grafting sites on the surface, (ii) attachment of a heterobifunctional PEG linker with its one end using a pre-activated carboxylic group, and (iii) coupling of biomolecules via a peptide bond formation. These three steps and the pre-activation of glass and silicon nitride surfaces to generate silanol groups before amination have been analyzed and optimized to gain a reproducible and high coupling efficiency and homogenous surface functionalization.

A comparison of surface amination through amino silane (APTES) and silanol group esterification with ethanolamine hydrochloride is described in the literature [1] and both methods

Abbreviations: AFM, atomic force microscope (or microscopy); BSA, bovine serum albumin; DMSO, dimethylsulfoxide; EDC, 1-ethyl-3-(3-dimethylaminopropyl)carbodiimide; H_2O_2, hydrogen peroxide; H_2SO_4, sulphuric acid; HCl, hydrogen chloride; HEPES, 4-(2-hydroxyethyl)-1-piperazineethanesulfonic acid; MeOH, methanol; NHS, N-succinimidyll; PBS, phosphate buffered saline; PEG, poly(ethylene glycol); SSC, saline-sodium citrate.

* Corresponding author. Tel.: +49 211 81 14387; fax: +49 211 81 14623.
E-mail address: filipp.oesterhelt@uni-duesseldorf.de (F. Oesterhelt).

0927-7765/$ – see front matter © 2009 Elsevier B.V. All rights reserved.
doi:10.1016/j.colsurfb.2009.02.011

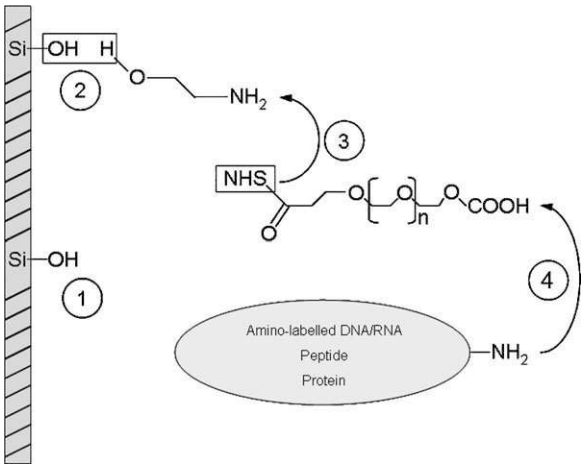

Fig. 1. Scheme of the immobilization procedure. Freshly cleaned and pre-activated support was incubated for 24 h in solution of 5 M ethanolamine hydrochloride in water-free DMSO at room temperature (1). After the esterification reaction of ethanolamine hydrochloride to the surface silanol groups, the supports were washed in DMSO, pure ethanol and water and then dried in a nitrogen stream (2). Aminated supports were immersed for 1 h in a dry DMSO solution containing 2 mM of heterobifunctional poly(ethylene glycol)-linker (NHS-PEG-$COOH_{MW3400}$) and 0.5% (v/v) triethylamine. The supports were washed afterwards in chloroform and water (3). Covalent immobilization of different biomolecules with free accessible amino groups was achieved via peptide bond formation. Here one-step direct coupling with EDC or a two-step indirect coupling with pre-activated carboxylic groups through EDC/NHS-activation was performed, which depends on the desired biomolecule for immobilization. After immobilization, the surfaces were washed stringent with an adequate washing procedure, dependent on the attached biomolecule (4).

were proven to be equally suitable to create an acceptable number of amino grafting sites for poly(ethylene glycol) attachment. However, ethanolamine hydrochloride serves better as amination substance in respect to the overall binding rate and has shown homogeneous coating compared to silanization in our observations. Generally, alkoxysilane molecules hydrolyze rapidly in water forming isolated monomers, cyclic oligomers and large intramolecular cycles [2,3], whereas the dominating species is dependent on the silane type, concentration, pH, temperature and reaction time as well as storage conditions. It has been shown, that silanizing with amino ethoxy silane on solid surfaces produces no homogeneous surfaces, but "islands" with large dimensions [4]. The polysiloxane structure inside such islands is also non-uniform and is composed of a 3D network of polysilane [5,6]. However, most single molecule applications and ligand–receptor investigations with AFM, optical tweezers and magnetic tweezers require a well-defined linker length, which is difficult to achieve using silanes because of their high tendency of self-polymerization. Instead we used ethanolamine hydrochloride, which creates homogeneous monolayers, an important prerequisite for homogeneous functionalization procedures.

To allow the immobilized biomolecules to interact with other molecules in their native way a distance of several nanometres between the biomolecule and the surface through flexible linkers is needed. Linear PEG chains have been commonly used to attach single biomolecules to glass surfaces, beads and AFM tips [7–12]. In comparison to other linker molecules, such as carboxyamylose [13] or dextran [14], poly(ethylene glycol) is simpler in handling, well characterized and chemically and physically inert. Additionally, it allows a rapid and free re-orientation of the attached biomolecule and also shields the surface due to non-specific interactions between biomolecules and surface [15,16]. The carboxylic group of the custom-synthesized heterobifunctional NHS-PEG-COOH applied here can be used for biomolecule immobilization and reacts less often non-specifically compared to the more commonly used amino and aldehyde end groups [11,17–19]. In this study, the binding capacity of three different PEG linkers (NHS-PEG-$COOH_{MW3400}$, NHS-PEG-$Aldehyde_{MW800}$ and NHS-PEG-$Maleimide_{MW3400}$) was compared with different immobilization strategies.

The final step in the immobilization process was also analyzed and optimized depending on the desired biomolecule to be attached. In this study an NH_2-labelled ssDNA oligonucleotide, a His_{10} containing peptide as His-tag and the prion–protein antibody IgG_{saf32} were tested to establish a general functionalization method for all kinds of biomolecules. For the final biomolecule attachment, the known method of peptide binding [20] including the use of EDC and sulfo-NHS with a high covalent binding rate [7] was applied reproducibly, without damaging the biomolecules or affecting their native behavior.

In this study a general "easy-to-use-protocol" for reliable and improved surface functionalization with ssDNA oligonucleotides was developed and evaluated by quantitative comparison to existing protocols. Finally, the applicability of the optimized method was demonstrated also for the immobilization of peptides and proteins.

2. Experimental procedures

2.1. Materials

Super pure-grade materials were used, when commercially available. Si_3N_4 AFM tips (MLCT series) were bought from Veeco Instruments (Dourdan, France). NHS-PEG-$COOH_{MW3400}$ was custom-synthesized by LaysanBio (AL, USA). Epoxy-PEG-$COOH_{MW3400}$ was purchased from Iris Biotech (Marktredwitz, Germany). NHS-PEG-$Aldehyde_{MW800}$ was synthesized by Hermann Gruber (Keppler-University Linz, Austria). NHS-PEG-$Maleimide_{MW3400}$ was purchased from Rapp Polymere (Tübingern, Germany). Borosilicate glass slides were purchased from Schott (Jena, Germany). Used DNA oligonucleotides (sequence of binding-ssDNA: 5′-NH_2-CCACTCGTGACGCATTCACCTCAGC-AGCACTCCTCCTCGG-3′; complementary fluorophor labelled ssDNA: 5′-CCGAGGAGGAGTGCTGCTGAGGTGAATGCGTCACGAGTGG-Atto647N-3′) were synthesized by PURIMEX (Grebenstein, Germany). Antibody IgG_{saf32} were purchased from SpiBio (Montigny-le-Bretonneux, France). His_{10} containing peptide (sequence: N-GGSGSGHHHHHHHHHH-C) was synthesized at the BMFZ (Heinrich-Heine University, Germany). SybrGreenII was bought from Sigma–Aldrich (Hamburg, Germany). Hellmanex cleaning detergent was purchased from Hellma (Mühlheim, Germany). Labelled Penta-His antibody labelled with Alexa488 was bought from Qiagen (Hilden, Germany). Alexa Fluor 633 F(ab′)-fragment of goat anti-mouse IgG (H + L) was purchased from Invitrogen (Karlsruhe, Germany). Ultra pure water was gained from the water processing apparatus Arium 611 from Sartorius (Goettingen, Germany).

2.2. Glass supports

The experiments in this study were done with glass slides due to their simpler handling compared to cover slips commonly used in single molecule experiments. Since cover glasses are generally made of borosilicate, the experiments were consequently done on borosilicate cover slides. Furthermore, an approximately 15% higher immobilization density on borosilicate glass slides was achieved compared to common used soda-lime glass slides (data not shown).

2.3. General cleaning procedure of borosilicate glass supports and silicon nitride AFM tips

Cleaning before pre-activation and amination with ethanolamine hydrochloride is important for glass and silicon

nitride surfaces. The glass cleaning procedure was developed in the Institute of Physical Chemistry (Heinrich-Heine University) for both, cleaning and reducing fluorescence background and controlled via TIRF measurements. Glass surfaces were covered in 5% (v/v) Hellmanex solution and sonicated for 20 min at 37 °C. After washing 10 times with water, the surfaces were covered in pure acetone and sonicated for further 20 min. After an additional washing step in water a 20 min ultrasonication in pure ethanol was performed. The plate was washed again with water before a final 20 min ultrasonication step in pure water. After cleaning, the surfaces were dried in a nitrogen flow. The silicon nitride AFM tips were just washed twice in dry chloroform and dried in a nitrogen stream before further functionalization.

2.4. Working protocol for surface functionalization and immobilization of ssDNA oligonucleotides

This easy to use surface functionalization and amino-labelled oligonucleotide immobilization protocol is based on different published protocols and is used in the following as a starting point in the detailed protocol optimization process (Fig. 1).

Pre-activation of a cleaned surface is important in order to generate a high density of silanol groups on the surfaces, which allows surface amination through an esterification reaction. The borosilicate glass and silicon nitride supports were pre-activated in piranha solution (3:1 (v/v), H_2SO_4:H_2O_2) for 30 min at room temperature. After washing shortly in pure water and drying in a nitrogen flow, the supports were immersed in 5 M ethanolamine hydrochloride in water-free DMSO for 24 h at room temperature for homogeneous amination. This procedure was based on studies where ethanolamine amination was tested with different molarities and temperatures [1]. After amination, the supports were washed in dry DMSO, in pure ethanol and finally 5 times with ultra pure water and dried again in a nitrogen flow. In the second step of functionalization, the amino-reactive heterobifunctional poly(ethylene glycol) NHS-PEG-$COOH_{MW3400}$ was immobilized on the supports which serves as a linker between the surface and the amino-labelled ssDNA oligonucleotide. 2 mM of the PEG linker was dissolved in water-free chloroform with 0.5% (v/v) triethylamine and the supports were incubated for 1 h at room temperature in this PEGylation solution. The supports were washed several times in ultra pure water after the PEGylation process. As our standard process, amino-labelled ssDNA oligonucleotides were immobilized to the free accessible carboxylic groups of the PEG linker via peptide binding. The peptide binding method is based on the one-step method with EDC in acidic buffer as carboxyl activation substance [7] to achieve the highest possible ssDNA immobilization rate. 10 μM amino-labelled ssDNA oligonucleotide was dissolved in 100 mM MES buffer (pH 4.75) with 50 mM EDC and added to the PEGylated supports. After 1 h reaction time at room temperature, the supports were washed for 5 min with ultra pure water, 10 min in a 100 mM KCl solution and finally again 5 min with ultra pure water.

2.5. Sample preparation and specific ligand binding

For the sample preparation and the optimization of the protocol in this study, the following sample configuration was used.

The 40b ssDNA oligonucleotide was covalently bound to the surface according to the working protocol (Fig. 2A and C) as a volume defined droplet of 0.5 μl. To test non-specific binding of ssDNA to the PEGylated surface, complementary 40b fluorophor labelled ssDNA was given on the support with a drop of about 20 μl volume in a wet atmosphere which covered a wider area around the previously immobilized ssDNA to allow simultaneous control of unspecific background interactions. The hybridization was done with a concentration of about 10 μM on the prepared surface in

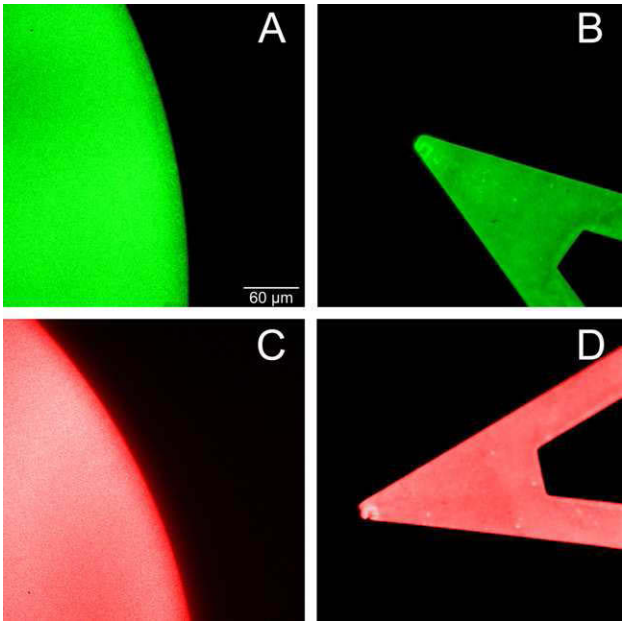

Fig. 2. Immobilization of 40b ssDNA oligonucleotide on borosilicate glass slides and silicon nitride AFM tips. On glass slides (A and C), 40b amino-labelled oligonucleotide was covalently bound to the PEG-modified surface in a round spot (approximately 200 μm). On silicon nitride supports (B and D), 40b amino-labelled ssDNA was covalently bound to the entire PEG-modified cantilever. (A and B) Fluorescence control was done via 0.02× single strand DNA staining SybrGreen. (C and D) A complementary 40b ssDNA oligonucleotide, labelled with Atto647N fluorophor was given to the supports.

20 mM TRIS/HCl hybridization buffer (pH 8.4) containing 100 mM NaCl and washed afterwards to remove non-specific ssDNA surface adsorptions in 2× SSC buffer at 65 °C (10°C below the melting temperature) for 5 min, in 0.01× SSC buffer at room temperature for another 5 min and finally stored in the hybridization buffer for further measurement.

The silicon nitride AFM tips were completely covered in the ssDNA binding and hybridization solutions because of their small dimensions (Fig. 2B and D).

To analyse the peptide immobilization quality, the immobilized His_{10} containing peptide was detected via the fluorophor labelled His-tag specific Penta-His-antibody labelled with an Alexa488 fluorophor.

The IgG_{saf32} antibody immobilization was verified through an Alexa633-labelled second antibody of goat anti-mouse IgG. The experimental procedure is described in detail in the respective description.

2.6. Experimental evaluation procedure

To evaluate the successful immobilization, the overall binding efficiency and the homogeneity of the functionalization procedure, the surfaces and AFM tips were analyzed via fluorescence detection of fluorophor labelled specific ligands binding to the immobilized biomolecules.

The samples were measured using an inverted microscope (Olympus IX71, Hamburg, Germany) with a peltier-cooled ECCD camera (Andor IXON, 512 × 512 pixels, Belfast, Ireland). Fluorophor excitation was achieved by a 150 W Xenon-lamp with the specific filter sets (AHF, Tübingen, Germany) due to the different fluorophores of the counter molecules (F41-054 for Alexa488, F41-008 for Alexa633 and Atto647N). On each sample the fluorescence intensity (in counts/s) was measured by taking the average over five areas of 10 × 10 pixels. Each experiment was performed five times to test the reproducibility.

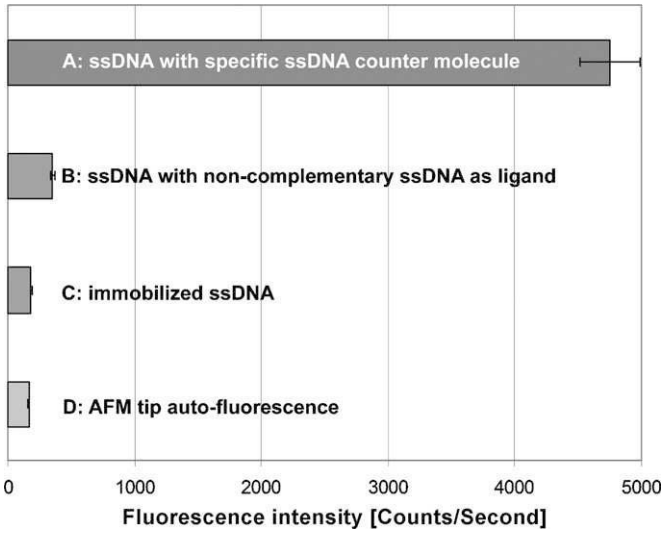

Fig. 3. DNA immobilization on silicon nitride AFM tips. (A) Immobilized 40b amino-labelled ssDNA, hybridized with complementary Atto647N-labelled oligonucleotide. (B) Same functionalization as in (A), but hybridized with non-complementary Atto647N-labelled ssDNA. (C) Immobilized ssDNA as in (A) and (B), but without further treatment with fluorescent counter molecule. (D) Auto-fluorescence of cleaned silicon nitride AFM tips.

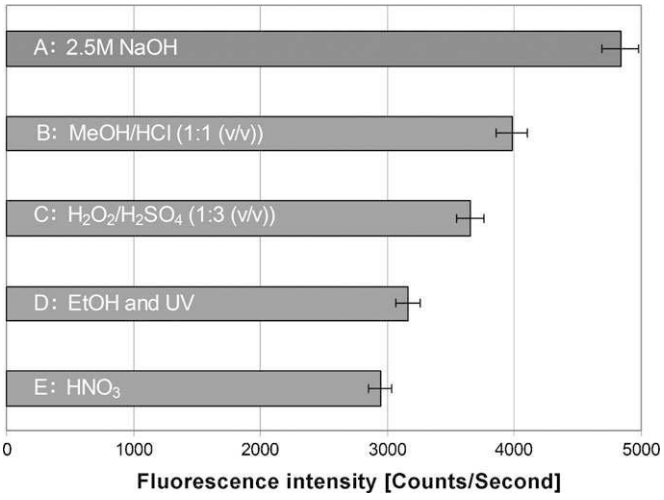

Fig. 4. Comparison of different methods to generate silanol groups on borosilicate glass surface. Solutions and treatment prior to the amination step were varied. (A) 24 h in 2.5 M NaOH at room temperature. (B) 1 h in 1:1 (v/v) MeOH:HCl at room temperature. (C) 30 min in piranha solution (1:3 (v/v) H_2O_2/H_2SO_4). (D) 30 min in ethanol, dried with N_2, and 1 h exposed to UV. (E) 1 h in nitric acid in boiling water bath. All surfaces were washed afterwards shortly in ultra pure water and dried with N_2 before further functionalization.

2.7. Verification via atomic force microscopy measurements

We used combined TIR (total internal reflection) fluorescence microscopy with an atomic force microscope (MFP3D, Asylum Research, USA) to verify the immobilization of biomolecules on surface and the topography change of glass supports due to different pre-activation substances.

2.8. Supplemental information

A brief flowchart with the functionalization and biomolecule immobilization strategy and a commented protocol for each step of the process can be found in the supplemental information.

3. Results and discussions

3.1. Covalent immobilization of ssDNA oligonucleotides to glass and silicon nitride supports

The amino-labelled 40b ssDNA oligonucleotide was successfully immobilized covalently to PEG-functionalized borosilicate glasses and silicon nitride supports with the described working protocol. The results from this preparation will be taken as reference data when varying the protocol in the further described optimization process. The immobilization on borosilicate glass and silicon nitride AFM cantilevers, which was analyzed by SybrGreenII ssDNA staining and by hybridization of complementary Atto647N labelled ssDNA as ligand, is shown in Fig. 2. The immobilization is homogeneous with low fluorescence background of about 3% on borosilicate glass by analysis via complementary fluorophor labelled ssDNA oligonucleotide. This low background ratio demonstrates that the used NHS-PEG-COOH linker also passivates the surface in respect to non-specific binding. The non-specific adsorption could occur from the complementary oligonucleotide itself or due to the attached Atto647N fluorophor, adsorbing to the PEG chain or the carboxylic end groups of the PEG linker.

The ssDNA immobilization with NHS-PEG-$COOH_{MW3400}$ as linker molecule was applied to silicon nitride AFM cantilevers in the same way (Fig. 3) as to borosilicate glass slides. For detailed analysis of the immobilization and detection quality, the ssDNA immobilization experiments were repeated five times. To determine the amount of non-specific ssDNA and linked fluorophor interaction with the functionalized silicon nitride surface, three negative tests were simultaneously performed. In the first negative test ssDNA functionalized silicon nitride AFM tips were incubated in a solution with non-complementary Atto647N-labelled ssDNA, in a second, ssDNA functionalized cantilevers were measured without further treatment and finally, the auto-fluorescence of cleaned cantilevers was determined.

The auto-fluorescence of the silicon nitride support and the immobilization without fluorescent ligand molecule shows an equal non-specific adsorption amount of 3% in respect to the immobilization on borosilicate glass slides. The successful and reproducible immobilization on silicon nitride AFM cantilevers agrees with the binding characteristics observed on borosilicate glass surfaces (Fig. 4C).

3.2. Optimizing the single functionalization steps to achieve higher immobilization efficiency

For optimizing the surface functionalization protocol, all individual steps in the entire functionalization process were varied systematically with respect to the working protocol, detecting the density and homogeneity via the complementary fluorophor labelled DNA oligonucleotides hybridized to the immobilized ssDNA. The images were taken with the IXON EMDDC camera and results are given in camera counts/s.

3.3. Pre-activation of supports

Already the pre-activation, which aims for silanol group generation on the substrate, is a very important step with respect to the amount of biomolecules finally bound to the surface. Thus, we compared four different protocols described in the literature to pre-activate borosilicate glass supports (Fig. 4) with our approach of using sodium hydroxide as pre-activation substance. Freshly cleaned borosilicate glass slides (see methodical part) were (i) covered in nitric acid (65%) in a boiled water bath for 1 h [7]; (ii) treated in pure ethanol for 10 min, dried in nitrogen stream and exposed to UV-light (UVO-Cleaner 42-220, Jelight Company Inc.,

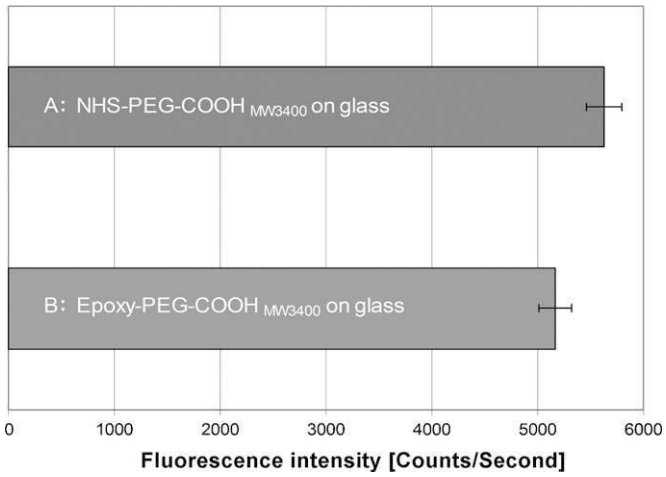

Fig. 5. Comparison between direct coupling of Epoxy-PEG-$COOH_{MW3400}$ to clean, pre-activated glass surface and the use of NHS-PEG-$COOH_{MW3400}$ with ethanolamine hydrochloride aminated surface. (A) Indirect coupling of NHS-PEG-$COOH_{MW3400}$ to prior aminated surface in dry DMSO solvent with 0.5% (v/v) triethylamine. (B) Direct coupling of Epoxy-PEG-$COOH_{MW3400}$ in dry $CHCl_3$ solvent with 0.5% (v/v) triethylamine.

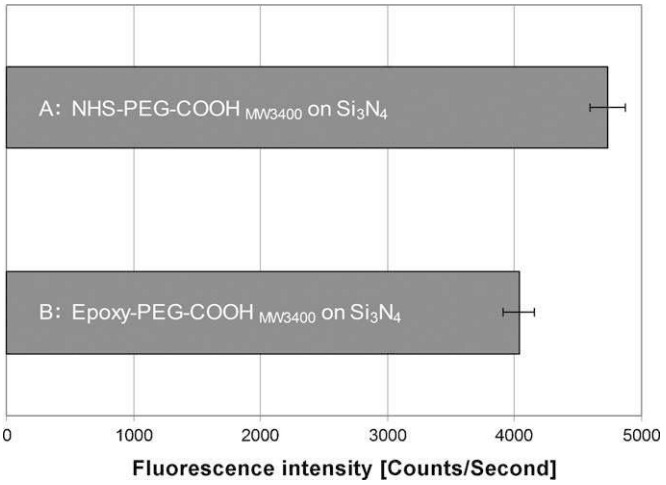

Fig. 6. Comparison between direct coupling of Epoxy-PEG-$COOH_{MW3400}$ to clean, pre-activated silicon nitride AFM tips and the use of NHS-PEG-$COOH_{MW3400}$ with ethanolamine aminated surface. (A) Indirect coupling of NHS-PEG-$COOH_{MW3400}$ to prior aminated AFM tip in dry DMSO solvent with 0.5% (v/v) triethylamine. (B) Direct coupling of Epoxy-PEG-$COOH_{MW3400}$ in dry $CHCl_3$ solvent with 0.5% (v/v) triethylamine.

Irvine, USA) for 1 h [11]; (iii) deposited in fresh piranha solution for 30 min at room temperature [8,17]; (iv) incubated for 1 h in 1:1 (v/v) MeOH:HCl [14] and (v) stored for 24 h in 2.5 M NaOH at room temperature. After treatment, the pre-activated glass supports were rinsed quickly with ultra pure water and dried in a nitrogen flow. Further treatment was performed as described in Section 2.4.

The comparison showed that the use of 2.5 M NaOH over 24 h was the best method to generate a high number of silanol groups on borosilicate glass supports, which allows a high density of amination and further covalent biomolecule immobilization. The commonly used piranha solution, which was also applied in our standard functionalization procedure, results in 24% less fluorescence intensity compared to the NaOH pre-activation.

Additionally, the surface roughness of cleaned and NaOH-activated glass was investigated with an AFM to determine, if the strong alkalise treatment significantly changes the surface topography, which would be a disadvantage of this pre-activation method. However, the AFM measurements showed no difference in the surface topography and the roughness of about 1.0 ± 0.2 nm in average was equal to non-treated cleaned glass.

3.4. Direct coupling of silanol-reactive PEG linker to glass and silicon nitride supports

We took advantage of the general property of epoxy rings to bind covalently to amino groups and hydroxyl groups, and also tested the direct coupling of a heterobifunctional PEG linker which bears an active epoxy ring to the silanol groups of the pre-activated glass surfaces and silicon nitride AFM tips. This alternative functionalization procedure saves preparation time and possible contamination in respect to the used substances and solvents for the additional functionalization and washing steps.

2 mM Epoxy-PEG-$COOH_{MW3400}$ was dissolved in dry $CHCl_3$ with 0.5% (v/v) triethylamine and was let to react with the pre-activated glass (Fig. 5) and silicon nitride supports (Fig. 6) for 1 h at room temperature. Here, all supports were pre-cleaned as described before, pre-activated with 2.5 M NaOH for 24 h, washed shortly with ultra pure water and were then either directly used for PEGylation with Epoxy-PEG-$COOH_{MW3400}$ or functionalized with ethanolamine hydrochloride and NHS-PEG-$COOH_{MW3400}$. Further treatment was performed as described in Section 2.4.

The direct binding of the Epoxy-PEG-$COOH_{MW3400}$ linker to the pre-activated silanol groups showed successful oligonucleotide immobilization. Compared to the three-step procedure immobilization yielded approximately 91% on the borosilicate glass supports (Fig. 5) and 85% on silicone nitride AFM tips (Fig. 6). Thus, this two-step functionalization procedure serves as a suitable alternative depending on the desired density of immobilized biomolecules for both supports. The loss in binding yield may be explained by hydroxylation of the epoxy group during binding and the use of non-modified or non-reactive PEG linkers during synthesis. These unmodified or abreacted PEG molecules could adsorb to the surface during the binding process and hinder other PEG linkers to bind.

3.5. Effect of solvent for NHS-PEG-COOH linker attachment

The use of the polymeric linkers plays also an important role with respect to the passivation against non-specific interactions of the biomolecules with the surface. At this point, the density of the used linkers is a crucial factor. Thus, beside the coupling chemistry also the reaction condition, especially the solvent is important for covalent surface coupling of the used polymeric linkers. Therefore, after cleaning, pre-activation and amination of the borosilicate glasses according to the working protocol given above, the NHS-PEG-$COOH_{MW3400}$ linker was dissolved in either water-free chloroform or water-free DMSO containing 0.5% (v/v) triethylamine and was given to the fresh, aminated supports for 1 h at room temperature for covalent attachment (Fig. 7). Further treatment was performed as described in Section 2.4.

Generally, using dry solvents is crucial for obtaining high binding yields of the PEG linker. However, the comparison of dry chloroform and dry DMSO (Fig. 7) shows, that DMSO as reaction solvent leads to an approximately 42% higher number of successfully bound heterobifunctional PEG linkers on aminated borosilicate glass. The PEG itself is less soluble in DMSO as in chloroform and accordingly for larger NHS-PEG-COOH chains (MW 35,000) it was observed, that DMSO was not a suitable solvent any more. Short PEG linkers lead to a less extended coil of the solvated polymer and thus enable a more tight packing on the surface.

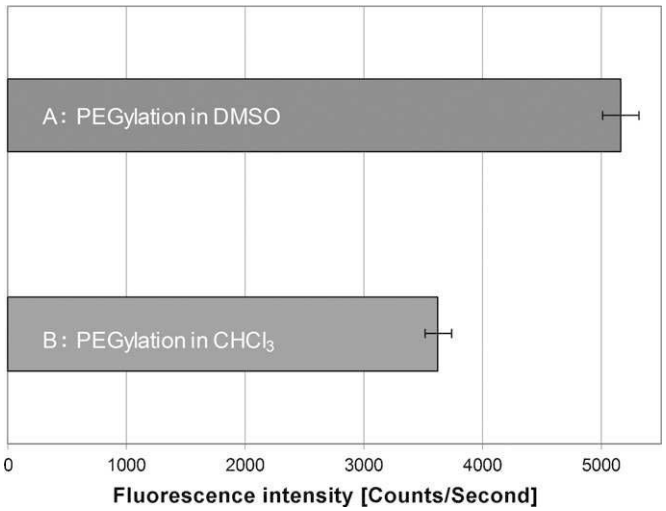

Fig. 7. Comparison of two solvents for the covalent PEG linker coupling on aminated surfaces. The surfaces were functionalized with amino-labelled 40b ssDNA and hybridized with complementary fluorescent Atto647N-labelled ssDNA as counter molecule. (A) NHS-PEG-$COOH_{MW3400}$ coupled in dry DMSO with 0.5% (v/v) triethylamine. (B) NHS-PEG-$COOH_{MW3400}$ bound in dry chloroform with 0.5% (v/v) triethylamine.

3.6. Biomolecular coupling chemistry

For the immobilization of biomolecules most commonly aldehyde and maleimide groups [11,17–19] are used. Thus, the use of the NHS-PEG-$COOH_{MW3400}$ linker was compared quantitatively with the two commonly used poly(ethylene glycol) linkers, NHS-PEG-$Aldehyde_{MW800}$ and NHS-PEG-$Maleimide_{MW3400}$. The cleaning, pre-activation, amination and PEGylation steps were done on borosilicate glass according to the working protocol given above.

For amino-labelled ssDNA coupling to the aldehyde end group of the NHS-PEG-$Aldehyde_{MW800}$ linker, the pegylated supports were treated with 10 μM of the same amino-labelled oligonucleotide which was used for the standard immobilization procedure in PBS buffer (pH 7.4). Additionally, 1 μl of chemical elimination solution, which contains 450 μl H_2O, 50 μl 100 mM NaOH and 32 mg $NaCNBH_3$, was added to the ssDNA coupling solution. After 1 h reaction time at room temperature, the washing of the surfaces was done by immersing in ultra pure water for 5 min, 10 min in a 100 mM KCl solution and finally again 5 min in ultra pure water.

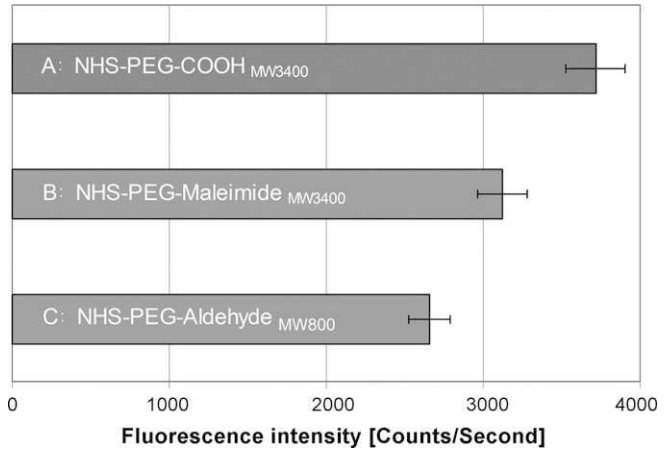

Fig. 8. Comparison between three immobilization strategies with different PEG linker molecules. (A) NHS-PEG-$COOH_{MW3400}$ as PEG linker with immobilized amino-labelled ssDNA oligonucleotide. (B) NHS-PEG-$Maleimide_{MW3400}$ as linker molecule with coupled thiol-labelled oligonucleotide with the same sequence as in (A). (C) NHS-PEG-$Aldehyde_{MW800}$ linker with same bound amino-labelled ssDNA as in (A). Fluorescence emission data results due to hybridized complementary ssDNA labelled with Atto647N as fluorophor.

For immobilization of ssDNA to the NHS-PEG-$Maleimide_{MW3400}$ linker, thiol-modified ssDNA oligonucleotides were given to the supports in PBS buffer at pH 7.4 at room temperature for 1 h reaction time. The surfaces were washed afterwards with the same procedure as described for aldehyde coupling.

Further hybridization with the complementary fluorescent ssDNA was done for all surfaces equally and measured as described in the methodical part.

Using a carboxyl end group for coupling the amino-labelled ssDNA oligonucleotides, an approximately 28% higher amount of coupled molecules compared to the binding via NHS-PEG-$Aldehyde_{MW800}$ (Fig. 8) was detected in spite of the fact, that the smaller molecular weight of the aldehyde linker in principle might favor a more dense packing on the surface. Compared to the use of NHS-PEG-$Maleimide_{MW3400}$, still a 16% higher amount was observed. Thus, the use of NHS-PEG-$COOH_{MW3400}$ appears as the best choice as reactive group for immobilization of biomolecules to the PEGylated surface with respect to a high immobilization efficiency and high reproducibility.

3.7. Optimized protocol for surface functionalization and DNA immobilization

On summary, the optimization process resulted in the following optimized protocol: The pre-activation has to be done with both, the borosilicate glass and silicon nitride supports in 2.5 M NaOH for 24 h at room temperature. After rinsing quickly with ultra pure water, the supports have to be incubated in 5 M ethanolamine hydrochloride solution with dry DMSO as solvent and containing 0.5% (v/v) triethylamine for another 24 h at room temperature. PEGylation with 2 mM NHS-PEG-$COOH_{MW3400}$ was performed in dry DMSO as solvent and 0.5% (v/v) triethylamine for 1 h reaction time at room temperature. Alternatively, the supports can be directly coated with 2 mM Epoxy-PEG-$COOH_{MW3400}$ linker in dry chloroform with 0.5% (v/v) triethylamine for 1 h at room temperature. The PEG coated surfaces should be washed several times with ultra pure water afterwards. Amino-labelled ssDNA, dissolved in 100 mM MES buffer (pH 4.75) with 50 mM EDC, should be given to the PEGylated supports for 1 h at room temperature. Finally, the supports have to be washed 5 min with ultra pure water, 10 min with 100 mM KCl and again 5 min with ultra pure water. The supports can be stored at this point in appropriate buffer or in dried state.

3.8. Surface functionalization and DNA immobilization validation via AFM imaging

Finally we applied an additional quality control via AFM imaging and manipulation. Therefore we functionalized a standard borosilicate cover slide commonly used in single molecule fluorescence and AFM experiments according to our optimized functionalization protocol. Subsequently, we immobilized 40b ssDNA oligonucleotides onto a spot with approximately 3 mm of diameter. AFM imaging of the edge of the spot revealed the height difference between the only PEG coated glass slide and the spot, originating from the additional layer thickness due to the immobilized ssDNA oligonucleotides (Fig. 9A).

In our total internal reflection fluorescence setup routinely used for single fluorophor detection and AFM based nano-manipulation experiments we imaged the spot after hybridizing the fluorophor labelled complementary 40b ssDNA oligonucleotides. Before imaging, we used the nano-manipulation setup to scratch out a rectangular area of about 5 μm × 3.5 μm with a force of about 7 nN. Fig. 9B clearly shows the removal of the fluorophor labelled

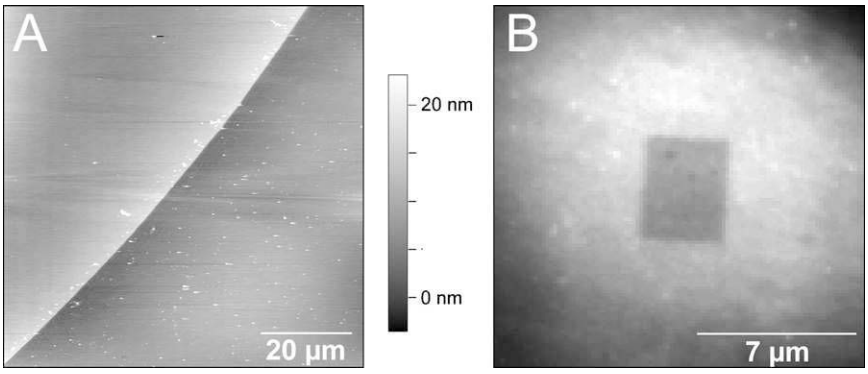

Fig. 9. (A) Topography image of dense immobilized 40b amino-labelled ssDNA oligonucleotides on a prepared PEGylated surface. (B) Fluorescence TIRF image of the same prepared surface as in (A), after hybridization of complementary fluorophor (Atto647N) labelled DNA oligonucleotide. A rectangular area with 5 μm × 3.5 μm in dimensions was scrapped free of DNA via the AFM tip with a contact force of 7 nN.

oligonucleotides as a dark rectangular area within the fluorescent surface.

3.9. Covalent peptide immobilization on PEG-functionalized supports

For immobilization of biomolecules via the peptide binding method, the carboxyl groups of the PEG linker on the surface were activated prior to immobilization. If the biomolecules to be immobilized bears no accessible carboxyl groups at the C-terminus, the activation can be done in one step with the immobilization by adding just EDC to the buffer. Otherwise carboxyl groups have to be activated in an additional previous step to avoid polymerization of the biomolecules. To demonstrate that the immobilization protocol developed here also serves for peptide coupling and to compare the two step pre-activation procedure with the one-step binding method, a 16 amino acids peptide containing 10 histidine (N-GGSGSGHHHHHHHHHH-C) was immobilized according to the optimized protocol. The C-terminus of the peptide was protected by an amide modification to prevent polymerization of the peptides during surface coupling. For comparison, the same peptide was immobilized with pre-activation of the surface bound carboxyl groups of the PEG linker, which may serve as an example for coupling peptides without inactivated C-terminus. Here, the carboxylic end group of the PEG linker was activated with NHS in presence of EDC in 100 mM MES buffer (pH 4.75) prior to the peptide binding in PBS buffer [7].

In the one-step method, analogue to the ssDNA immobilization, 10 mM of the peptide with protected C-terminus was let to react in 100 mM MES buffer (pH 4.75) with 50 mM EDC to the surface for 1 h at room temperature. In the two-step method, the carboxylic groups of the PEG linker were pre-activated with 50 mM EDC and 50 mM NHS in 100 mM MES buffer (pH 4.75) for 1 h. After washing shortly in ultra pure water, 10 μM of the peptide was given to the pre-activated surface in slight basic HEPES buffer (pH 8) at room temperature for 1 h reaction time.

The peptide immobilization was detected via binding of a histidine specific antibody (Penta-anti-HIS, Qiagen) labelled with Alexa488 and fluorescence imaging (Fig. 10).

The one-step immobilization procedure led to an approximately 29% higher number of immobilized peptides compared to the two-step procedure. This may happen due to hydrolyzation of NHS during the activation of the carboxylic groups and the washing procedure prior to peptide immobilization. While studying peptide immobilization, we also tried to immobilize a His_6 peptide without the additional N-GGSGS-C linker sequence. However, in that case the N-terminus of the His_6 was not accessible for coupling to the surface bound carboxyl groups. Only by adding the linker sequence N-GGSGS-C to the N-terminus the peptide could be bound covalently to the carboxylic groups of the NHS-PEG-$COOH_{MW3400}$ linker.

3.10. Covalent protein immobilization on PEG-functionalized supports

The optimized protocol for surface functionalization was also tested for the coupling of proteins by immobilizing the prion–protein antibody IgG_{saf32} (Fig. 11) analogue to the two-step immobilization procedure of peptides described before.

After pre-activation of the carboxyl groups of the PEG-functionalized glass surface through 50 mM EDC and 50 mM NHS in 100 mM MES buffer (pH 4.75) for 45 min, 1 mM IgG_{saf32} was given to the surface in PBS buffer with a moderate lower pH of about 6 for 1 h at room temperature and washed afterwards four times in PBS buffer (pH 7.4). For fluorescent analysis, 125 mM Alexa633-labelled second antibody of goat anti-mouse IgG fragment (H + L) in PBS buffer (pH 7.4) with 1.5% (v/v) BSA was given to the surface at room temperature for 1 h and washed again four times with PBSTT buffer (PBS (pH 7.4), 0.05% Tween 20, 0.2% Triton X100) and finally three times in PBS buffer (pH 7.4).

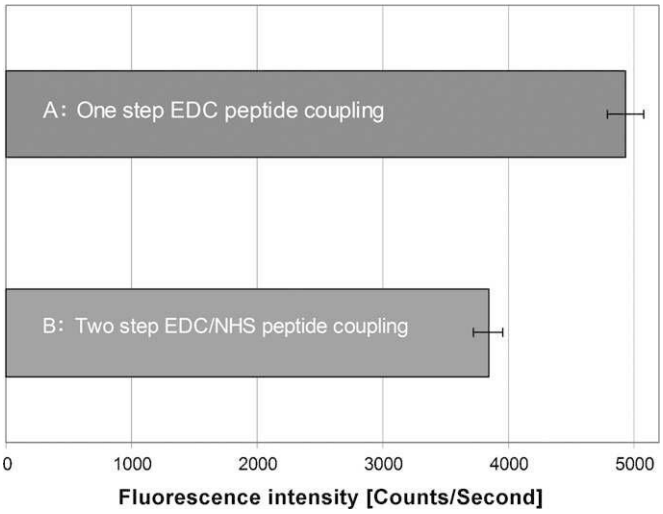

Fig. 10. Covalent immobilization of a 16 amino acid peptide containing 10 histidine and fluorescence analysis via a Penta-anti-His antibody labelled with Alexa488 fluorophor. Comparison between the direct and indirect coupling method. (A) Peptide with protected carboxylic group (amide modification) was immobilized directly in 100 mM MES buffer (pH 4.75) and 50 mM EDC for 1 h. (B) Carboxylic group of PEG linker was pre-activated with 50 mM EDC and 50 mM NHS in 100 mM MES buffer (pH 4.75). Peptide was immobilized in HEPES buffer (pH 8) for 1 h reaction time.

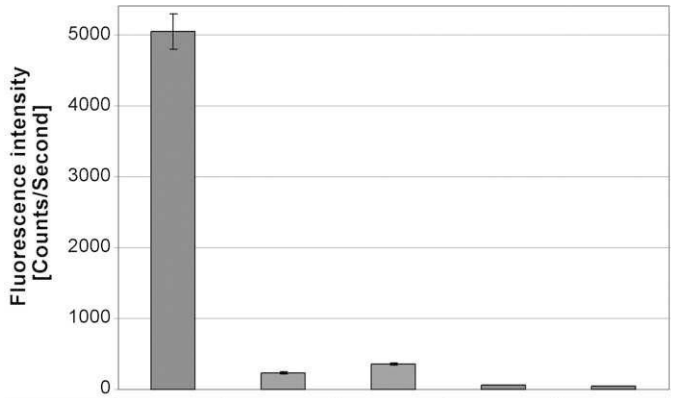

Sample	A	B	C	D	E
Ethanol amine	X	X	X	X	X
PEG linker	X	X	X		
First Antibody	X				
BSA Blocking	X	X			
Second Antibody	X	X	X	X	

Fig. 11. Prion-antibody IgG_{saf32} was immobilized through the two-step EDC/NHS-coupling method to PEGylated surface with NHS-PEG-$COOH_{MW3400}$. Fluorescence measurements were performed using fluorescent second antibody Alexa Fluor 633 F(ab′) fragment of goat anti-mouse IgG (H + L). (A–F) Different sample compositions with positive and negative controls. Sample conditions specified in table below.

To investigate the amount of non-specific interactions, the passivation characteristics of the NHS-PEG-$COOH_{MW3400}$ linker and the influence of additional BSA (3% in H_2O) in respect to surface blocking after protein immobilization, several additional negative tests were performed and compared (Fig. 11).

Similar to the two-step EDC/NHS binding method of peptides, the antibody IgG_{saf32} was successfully immobilized on the NHS-PEG-$COOH_{MW3400}$ modified glass support (Fig. 11A), where the different experimental compositions are also shown.

The negative tests show an overall low background signal (Fig. 11E) of ethanolamine hydrochloride as amination substance and low non-specific physisorbtion of the fluorescent second antibody (Fig. 11D) on the amine surface layer. A low, but still significant adsorption about 5.9% (Fig. 11C) of the fluorescent second antibody was observed on the PEGylated surface which can be explained through spontaneous low-rate peptide binding and non-specific adsorption to the carboxylic end groups of the PEG linker. However, it can be reduced down to approximately 3.4% by additional BSA (3%) blocking (Fig. 11B).

Additionally, previous experiments have shown (data not shown), that directly bound proteins using epoxy silane without a PEG linker in-between, were not accessible for second antibody counter molecules, which shows that a linker is important for the immobilized protein accessibility for applications in sensoring and interaction detection.

4. Conclusions

In this study, a ubiquitous, simple and straight forward coupling procedure of biomolecules (DNA, peptides and proteins) with a heterobifunctional poly(ethylene glycol) linker to borosilicate glass and silicon nitride supports was developed. In addition, the passivation character of the PEG linker which prevents the non-specific adsorption of the different biomolecules to the functionalized surfaces was proven. In respect to the commonly used functionalization methods which were compared in this study for each single step in the entire functionalization process, we yield an increase up to 3-fold in binding efficiency by optimizing each functionalization step and using a NaOH solution of high molarity for pre-activation and heterobifunctional NHS-PEG-$COOH_{MW3400}$ as biomolecule linker molecule. By applying a silanol-reactive PEG linker, which offers a faster and easier preparation effort, we still achieve a significant higher coupling density up to 173%, compared to the common methods, although the binding efficiency is slightly lower than our optimized three-step procedure with ethanolamine as surface linker molecule.

The reliable functionalization procedure is highly reproducible and leads to homogeneously modified surfaces, which is important for single molecule applications, biosensors and other sensitive ligand–receptor interaction studies. Especially for this kind of research, the demonstrated modification method does not influence or harm the native structure and behavior of the individual biomolecules. Also, the use of the PEG linker to depart the biomolecules from the surface is essential as it allows steric freedom and thus fully operating molecules and also leads to low non-specific adsorption. Taken together, the insights from this study provide a great approach to bio-functionalization of any probes with single molecules.

Acknowledgments

Franziska Henke is acknowledged for help in developing the protein immobilization. Peter Hinterdorfer is acknowledged for the synthesis of NHS-PEG-Aldehyde. This work was supported by the BMBF nanotechnology competition project no. 03N8714.

Appendix A. Supplementary data

Supplementary data associated with this article can be found, in the online version, at doi:10.1016/j.colsurfb.2009.02.011.

References

[1] A. Ebner, P. Hinterdorfer, H.J. Gruber, Ultramicroscopy 107 (2007) 922.
[2] E. Metwalli, D. Haines, O. Becker, S. Conzone, C.G. Pantano, Journal of Colloid and Interface Science 298 (2006) 825.
[3] H. Ishida, J.L. Koenig, Polymer Engineering and Science 18 (1978) 128.
[4] E.T. Vandenberg, L. Bertilsson, B. Liedberg, K. Uvdal, R. Erlandsson, H. Elwing, I. Lundström, Journal of Colloid and Interface Science 147 (1991) 103.
[5] D. Wang, F.R. Jones, P. Denison, Journal of Materials Science 27 (1992) 36.
[6] D. Wang, F.R. Jones, Journal of Materials Science 28 (1993) 2481.
[7] M.K. Walsh, X. Wang, B.C. Weimer, Journal of Biochemical and Biophysical Methods 47 (2001) 221.
[8] A.S.M. Kamruzzahan, A. Ebner, L. Wildling, F. Kienberger, C.K. Riener, C.D. Hahn, P.D. Pollheimer, P. Winklehner, M. Hölzl, B. Lackner, D.M. Schörkl, P. Hinterdorfer, H.J. Gruber, Bioconjugate Chemistry 17 (2006) 1473.
[9] C.K. Riener, C.M. Stroh, A. Ebner, C. Klampft, A.A. Gall, C. Romanin, Y.L. Lyubchenko, P. Hinterdorfer, H.J. Gruber, Analytica Chimica Acta 479 (2003) 59.
[10] P. Hinterdorfer, H.J. Gruber, F. Kienberger, G. Kada, C. Riener, C. Borken, H. Schindler, Colloids and Surfaces B: Biointerfaces 23 (2002) 115.
[11] T. Strunz, K. Orozland, R. Schäfer, H.J. Güntherodt, Proceedings of the National Academy of Sciences of the United States of America 9 (1999) 11277.
[12] C. Albrecht, M. Lalic-Mühltaler, S. Hirler, T. Bayer, H. Clausen-Schaumann, H.E. Gaub, Science 301 (2003).
[13] F. Kühner, L.T. Costa, P.M. Bisch, S. Thalhammer, W.M. Heckl, H.E. Gaub, Biophysical Journal 8 (2004) 2683.
[14] P. Vermette, T. Gengenbach, U. Divisekera, P.A. Kambouris, H.J. Griesser, L. Maegher, Journal of Colloid and Interface Science 259 (2003) 13.
[15] K. Blank, T. Mai, L. Gilbert, S. Schiffmann, J. Rankl, R. Zivin, C. Tackney, T. Nicolaus, K. Spinnler, F. Oesterhelt, M. Benoit, H. Clausen-Schaumann, H.E. Gaub, Proceedings of the National Academy of Science 100 (20) (2003) 11356.
[16] X. Yong-Mei, H. Zhi-Shan, S. Onnop, B. Ayse, G. Erdogan, Journal of Chemical Technology & Biotechnology 82 (2007) 33.
[17] N. Zammatteo, L. Jeanmart, S. Hamels, S. Courtois, P. Louette, L. Hevesi, J. Remacle, Analytical Biochemistry 280 (2000) 143.
[18] K. Lindroos, U. Liljedahl, M. Raitio, A. Syvanen, Nucleic Acids Research 29 (2001) e69.
[19] R. Krautbauer, M. Rief, H.E. Gaub, Nano Letters 3 (2003) 493.
[20] M. Grandbois, M. Beyer, M. Rief, H. Clausen-Schaumann, H.E. Gaub, Science 283 (1999) 1727.

Structure
Article

Transducer Binding Establishes Localized Interactions to Tune Sensory Rhodopsin II

David A. Cisneros,[1,4] Leoni Oberbarnscheidt,[2] Angela Pannier,[1] Johann P. Klare,[3,5] Jonne Helenius,[1] Martin Engelhard,[3] Filipp Oesterhelt,[2,*] and Daniel J. Muller[1,*]
[1]Biotechnology Center, University of Technology, Dresden, Germany
[2]Physikalische Chemie II, Heinrich-Heine-Universität, Düsseldorf, Germany
[3]Max-Planck-Institute for Molecular Physiology, Dortmund, Germany
[4]Present address: Molecular Genetics Unit and CNRS URA2172, Institut Pasteur, Paris, France
[5]Present address: Fachbereich Physik, Universität Osnabrück, Germany
*Correspondence: filipp.oesterhelt@uni-duesseldorf.de (F.O.), mueller@biotec.tu-dresden.de (D.J.M.)
DOI 10.1016/j.str.2008.04.014

SUMMARY

In haloarchaea, sensory rhodopsin II (SRII) mediates a photophobic response to avoid photo-oxidative damage in bright light. Upon light activation the receptor undergoes a conformational change that activates a tightly bound transducer molecule (HtrII), which in turn by a chain of homologous reactions transmits the signal to the chemotactic eubacterial two-component system. Here, using single-molecule force spectroscopy, we localize and quantify changes to the intramolecular interactions within SRII of *Natronomonas pharaonis* (NpSRII) upon NpHtrII binding. Transducer binding affected the interactions at transmembrane α helices F and G of NpSRII to which the transducer was in contact. Remarkably, the interactions were distributed asymmetrically and significantly stabilized α helix G entirely but α helix F only at its extracellular tip. These findings provide unique insights into molecular mechanisms that "prime" the complex for signaling, and guide the receptor toward transmitting light-activated structural changes to its cognate transducer.

INTRODUCTION

Microbial rhodopsins absorb light energy for ion transport or photosensation (Sharma et al., 2006). These photoreceptors are membrane proteins that share a common structural motif consisting of seven transmembrane α helices, A–G. A Schiff base located at the middle of the seventh α helix G covalently links the all-*trans* retinal chromophore to the protein. In haloarchaea, four different classes of microbial rhodopsins have been identified. Two of these, bacteriorhodopsin and halorhodopsin, use light to transport ions across the membrane and to establish ion gradients used as an energy source by other proteins. The other two retinal proteins, sensory rhodopsin I (SRI) and sensory rhodopsin II (SRII), mediate phototactic and photophobic responses, respectively. In addition, SRI mediates a repellent response after being activated by two sequential photons (Spudich and Bogomolni, 1984). SRI and SRII bind tightly to their cognate transducers, HtrI and HtrII, which upon activation by the receptor elicit a response via a cascade homologous to the chemotactic eubacterial two-component system. Both transducers contain two transmembrane α helices (TM1 and TM2) and a large cytoplasmic domain. Whereas the transmembrane domains of the transducer bind to the receptor and receive the light-activated signal, the two cytoplasmic subdomains transfer this signal to histidine kinase (CheA) (for reviews, see Klare et al., 2004, 2008; Spudich, 2006).

A model describing how the signal is transferred from SRII to its cognate transducer (HtrII) was proposed based on biochemical (Bergo et al., 2003; Wegener et al., 2000) and structural (Luecke et al., 2001; Wegener et al., 2001; Gordeliy et al., 2002; Moukhametzianov et al., 2006) data. Light excitation leads to the isomerization of the retinal chromophore from the all-*trans* to the 13-*cis* conformation, which due to thermal relaxation is followed by conformational changes in SRII. The protein passes through a series of spectroscopically detectable intermediates (Chizhov et al., 1998) denoted K, L, M, N, and O (named after BR intermediates). A spectroscopically silent irreversible reaction occurs between two M-states, M_1 and M_2, which has been correlated with the signaling state (Chizhov et al., 1998). In vivo experiments support this conclusion (Yan et al., 1991). Likely, signal transfer occurs when α helices F and G in SRII change conformations. These tilt and rotate the cytoplasmic side of the transmembrane α helix 2 of the bound HtrII (Moukhametzianov et al., 2006; Spudich, 2006).

In this study, we used single-molecule force spectroscopy (SMFS) to measure the interactions of SRII in the absence and in the presence of its transducer, HtrII (for a review on this technique, see Kedrov et al., 2007). SRII from *Natronomonas pharaonis* (NpSRII) was chosen because it represents the best characterized haloarchaeal photophobic rhodopsin receptor (Gordeliy et al., 2002; Klare et al., 2008; Spudich, 2006). Single-molecule force-distance (F-D) spectra for the mechanical unfolding of NpSRII and of NpSRII + NpHtrII complexes reconstituted in purple membrane lipids were obtained. The unfolding pattern, reflecting the interactions that stabilize structures within the receptors, was similar to that obtained previously of other archaeal rhodopsins (Cisneros et al., 2005; Muller et al., 2002). Introducing a simple method to analyze the membrane protein unfolding spectra, we could structurally map the interactions that have been established within the average NpSRII molecule. This

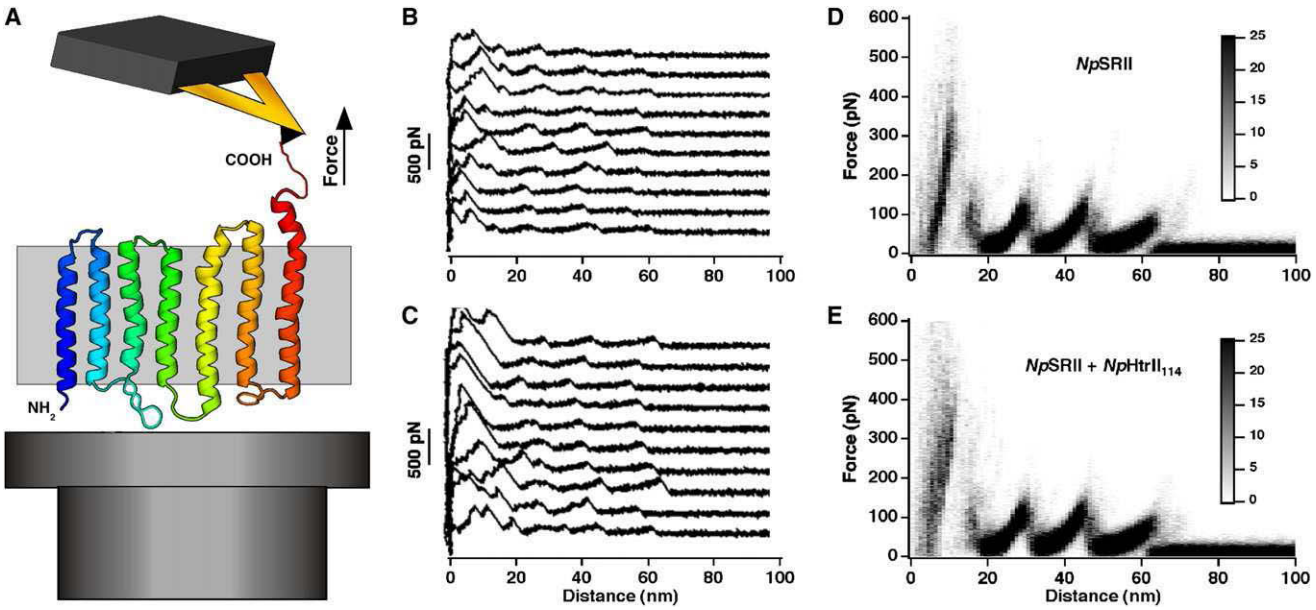

Figure 1. SMFS of NpSRII Alone and of NpSRII in a Complex with NpHtrII$_{114}$

(A) Contacting the terminal end of a single NpSRII with a molecularly sharp AFM tip forces the attachment of both. This molecular link allows exertion of a mechanical pulling force that initiates the stepwise unfolding of the receptor (here shown without transducer). (B) F-D curves recorded while unfolding single NpSRII molecules and (C) in complex with NpHtrII$_{114}$ by pulling from the C-terminal end. Superimpositions of F-D curves recorded from unfolding of (D) NpSRII alone and (E) NpSRII + NpHtrII$_{114}$ complexes. Superimpositions are represented as a density plots. F-D curves were obtained at room temperature at a pulling speed of ~300 nm/s in buffer solution (pH 7.8, Tris-HCl 20 mM, 300 mM KCl).

approach allows single-molecule experiments to describe the interactions common to all NpSRII molecules, normally revealed by conventional bulk experiments. The comparison of structural interaction maps revealed from SMFS disclosed the interactions of NpSRII that changed upon NpHtrII binding. Detectable changes were restricted to α helices F and G. Functional consequences are discussed in detail.

RESULTS

SMFS of NpSRII with and without Bound Transducer

To determine the interactions that stabilize structural regions of NpSRII and NpSRII bound to a truncated form of its transducer (NpHtrII$_{114}$), we applied SMFS as previously established for other archaeal rhodopsins and membrane proteins (Kedrov et al., 2007). Briefly, NpSRII and NpSRII bound to NpHtrII$_{114}$ were reconstituted in purple membrane lipids (Wegener et al., 2001). Subsequently, each sample was adsorbed to freshly cleaved mica supports (Muller et al., 1997). Resulting membrane patches were imaged using AFM (data not shown) and selected for SMFS analysis. After switching the AFM to the SMFS mode, single NpSRII molecules in the absence (NpSRII) or presence of their transducer (NpSRII + NpHtrII$_{114}$ complex) were attached nonspecifically to the AFM tip (Figure 1A; Oesterhelt et al., 2000). Retracting the AFM tip from the membrane induced the unfolding of single NpSRIIs. F-D curves recorded showed characteristic patterns of unfolding events (Cisneros et al., 2005; Muller et al., 2002). F-D curves of single NpSRII molecules attached by their C-terminal end to the AFM tip (see Experimental Procedures) were selected for further analysis. A total of 164 F-D curves were collected for NpSRII alone and 125 for the NpSRII + NpHtrII$_{114}$ complex. Every peak of an F-D curve represented the unfolding of one stable segment of the membrane protein (Janovjak et al., 2006; Kedrov et al., 2007). At first glance, the F-D curves tracing the unfolding process of NpSRII (Figure 1B) and NpSRII in presence of NpHtrII$_{114}$ (Figure 1C) were similar. However, individual F-D traces differed slightly from each other, lacking some force peaks or presenting force peaks at slightly different positions or of different strengths. To observe common features, the F-D traces were superimposed and displayed as density plots (Figures 1D and 1E). Such superimpositions represent the average F-D spectrum recorded. The superimpositions highlighted the same five major force peaks recorded for NpSRII alone (Figure 1D) and the NpSRII + NpHtrII$_{114}$ complex (Figure 1E). Comparing single F-D curves and the superimposed spectrum for the NpSRII alone (Figures 1B and 1D) with those for the NpSRII + NpHtrII$_{114}$ complex (Figures 1C and 1E) revealed differences within the first 20 nm of pulling. In this region the NpSRII + NpHtrII$_{114}$ complex showed larger forces and a higher density of force peaks.

Mapping the Probability at Which Force Peaks Occurred

While SMFS unfolding of bovine rhodopsin (Sapra et al., 2006b), bacteriorhodopsin (Muller et al., 2002), and halorhodopsin (Cisneros et al., 2005), we observed that each force peak within a F-D curve had a certain probability of occurring. To quantify the differences in peak appearance probability between F-D curves obtained from NpSRII alone and from the NpSRII + NpHtrII$_{114}$ complex, we fitted each force peak detected in individual F-D curves using the WLC model. As derived from the WLC fit, we

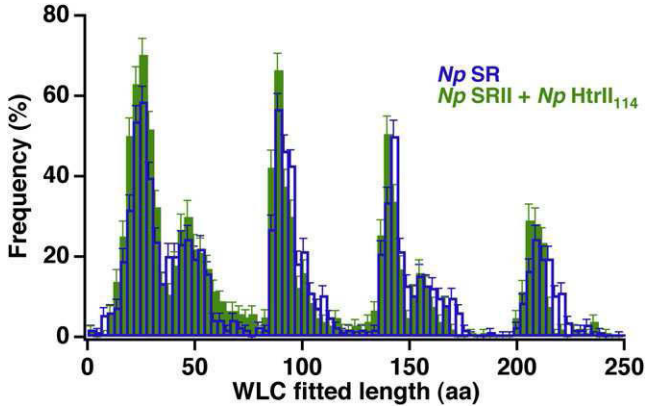

Figure 2. Frequency of Force Peaks Detected at Different Portions of the Stretched Polypeptide

Every force peak detected in individual F-D curves (Figure 1) was fitted using the WLC model, using the contour length of the polypeptide (L) as the only fitting parameter. The frequency at which the force peaks occurred is plotted in a histogram. NpSRII (blue, n = 164) and NpSRII + NpHtrII$_{114}$ complex (green, n = 125). Error bars represent the standard error of the mean (SEM). The length of the polypeptide is given in amino acids (aa). The bin size of the histogram is 3 aa and corresponds to the average precision at which individual force peaks could be fitted using the WLC model (Bustamante et al., 1994).

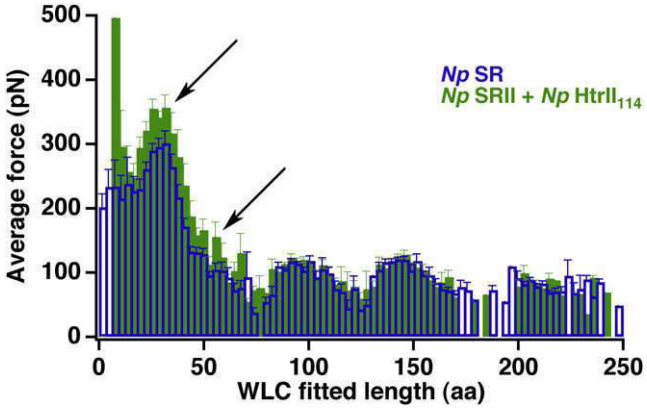

Figure 3. Average Force Detected at Different Positions of the Stretched Polypeptide

The force of every peak detected in an F-D curve was measured. The average force of force peaks are plotted at the WLC fitted lengths at which they were detected. Error bars represent the SEM. For each length of the stretched polypeptide, force peaks detected within 3 aa were pooled and averaged. Blue bars represent the average forces detected for NpSRII alone, the green bars the average forces detected for the NpSRII + NpHtrII$_{114}$ complex. Arrows indicate large changes in the interaction forces (see text for details).

converted the peak position measured in nanometers into the amino acid length of the stretched portion of the polypeptide (Muller et al., 2002; Oesterhelt et al., 2000). The frequency at which each force peak was detected at a certain position was plotted over the length of the stretched polypeptide (Figure 2). The findings showed a remarkable similarity of the occurrence of interactions detected between NpSRII alone (Figure 2, blue bars) and of NpSRII in complex with NpHtrII$_{114}$ (Figure 2, green bars). However, small differences were observed. These differences were distributed over most of the polypeptide lengths ranging from 15–25 aa, 60–80 aa, 140–170 aa, and 210–240 aa.

Determining the Average Interaction Strength of Force Peaks

Interactions within bacteriorhodopsin and other rhodopsins depend on boundary conditions such as pH, electrolyte (Kessler and Gaub, 2006; Park et al., 2007), temperature (Janovjak et al., 2003), point mutations (Sapra et al., 2008), and the oligomeric assembly (Sapra et al., 2006a). To quantify the interaction forces that changed within NpSRII upon formation of the NpSRII + NpHtrII$_{114}$ complex, we measured the strength of each force peak detected in the absence and in the presence of the transducer. The forces of all peaks occurring within a window of 3 aa were averaged and plotted over the stretched polypeptide length (Figure 3). Unlike the histogram of peak appearance frequency (Figure 2), the average forces plotted over the polypeptide length showed some pronounced changes occurring within the first 80 aa (Figure 3). At higher polypeptide lengths, the average forces were not significantly different. Within the first 50 aa of the polypeptide, the NpSRII + NpHtrII$_{114}$ complexes (Figure 3, blue bars) displayed higher forces compared with the NpSRII characterized in absence of the transducer (Figure 3, green bars).

Normalizing the Average Interaction Strengths of NpSRII

As calculated, the average peak force does not fully represent the interaction strength of a given structure. This is because the average force (Figure 3) did not take into account interactions (peaks) too weak to be detected. To normalize the average force, we multiplied the probability at which a force peak occurred (Figure 2) by the average force of the peak (Figure 3). The normalized average force reflects the average interaction strength established within a randomly picked NpSRII molecule. Or, seen from the bulk behavior, the normalized average force corresponds to that of all NpSRII molecules. Displaying the normalized average forces over the polypeptide length of NpSRII (Figure 4A) enhanced the differences in the interaction strengths between NpSRII with and without NpHtrII$_{114}$ bound. The distribution of these structural changes is highlighted when the differences between the normalized interactions strengths for each of the NpSRII molecule states is plotted (Figure 4B). In Figure 4A, the SEM shown in Figures 2 and 3 were used to calculate the SEM according to the following formula: $(SEM_{FP}/(F \cdot P))^2 = (SEM_{force}/F)^2 + (SEM_{prob}/P)^2$, where F is the mean force (Figure 2) and P is the probability (Figure 3) of a peak. For Figure 4B, the SEM was calculated as $SEM_{\Delta FP}{}^2 = SEM_{FP2}{}^2 + SEM_{FP1}{}^2$, where SEM_{FP2} and SEM_{FP1} are the normalized forces, F·N, calculated in Figure 4A for NpSRII bound or unbound to NpHtrII.

Mapping the Normalized Interactions onto the NpSRII Sequence

A force peak detected in the F-D spectrum denotes an interaction detected at a certain distance from the AFM tip (Kedrov et al., 2007). This distance is the length of the stretched polypeptide and can be used to locate the structural region of the membrane protein at which an interaction established a sufficient strength to be detected by SFMS. However, to correctly locate the interactions detected upon unfolding of NpSRII, it must be considered that some of the interactions establishing the

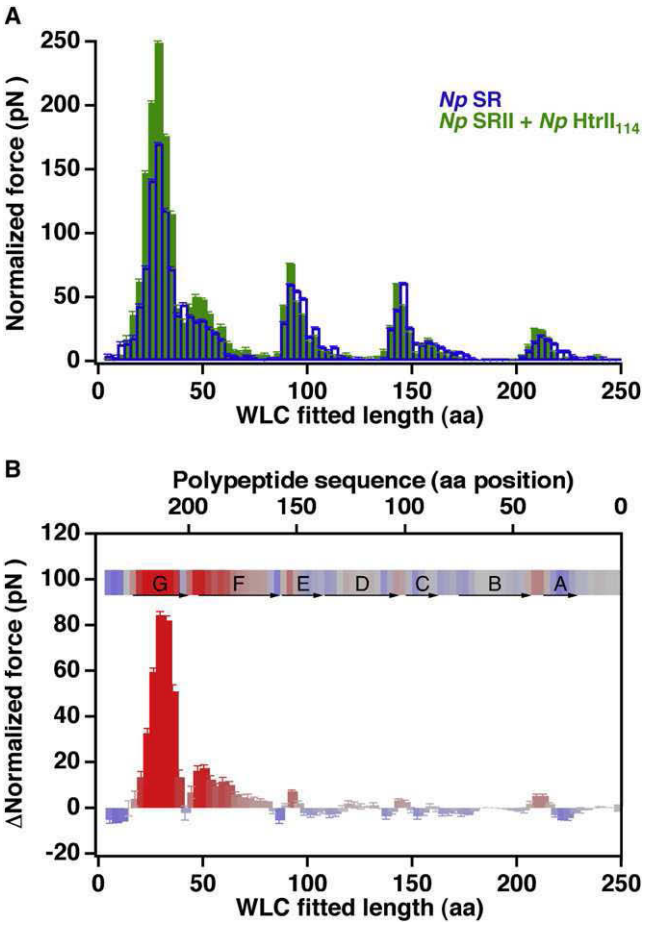

Figure 4. Normalizing and Mapping the Interactions Established within NpSRII upon Binding the Transducer (NpHtrII$_{114}$)

To combine force and probability (Figure 1), the average force (Figure 3) was multiplied with the frequency of force-peak appearance (Figure 2). (A) Normalized forces measured for NpSRII alone (blue) and for NpSRII complexed with NpHtrII$_{114}$ (green) are plotted. Error bars represent SEM. (B) Difference calculated between normalized interaction strengths detected for NpSRII without and with transducer (A) shows the interactions established upon NpHtrII$_{114}$ binding to NpSRII. The color scale (inset bar, saturated at 20 pN) indicates changes of the normalized force (positive = red, negative = blue). The bar above the force difference histogram (B) maps the interaction differences onto the loops and helices (lettered A–G) of the NpSRII structure. The lower x axis of the histogram shows the length of the stretched polypeptide as revealed from WLC fitting individual force peaks in the F-D spectra. The upper x axis reflects the amino acid position of structures holding the stretched NpSRII polypeptide chain. Small shifts in the positions of the force differences mapped onto the length of the stretched polypeptide (lower x axis) and onto the NpSRII polypeptide (upper x axis and scale bar above histogram) occur because systematic errors in the position of structural interactions lying within the membranes are corrected (see Experimental Procedures).

anchoring points of the polypeptide were located inside the membrane (Muller et al., 2002). Because the pulling distance is referred to the membrane surface, the position of unfolding barriers located inside the membrane had to be corrected. Thus, each polypeptide region at which the interaction occurred was located (Figure 4B). This correlation, shown in Figure 4B, highlights major differences in interactions detected within the first 70 C-terminal amino acids of NpSRII. Notably, the other NpSRII structures showed only minor variations (>70 aa; Figure 4B). The highest force difference of ~80 pN (Figure 4B) was centered at amino acid 34 of the stretched polypeptide, which corresponds to amino acid position ~211 (α helix G) as counted from the N-terminal end. A second maximum of ~18 pN was observed at a stretched polypeptide length of ~45 aa, or approximately amino acid position 174 (α helix F).

DISCUSSION

In recent years, SMFS has been applied to elucidate the unfolding pathways of bacteriorhodopsin (Muller et al., 2002), halorhodopsin (Cisneros et al., 2005), proteorhodopsin (Klyszejko et al., 2008), bovine rhodopsin (Sapra et al., 2006b), and several other membrane proteins (Kedrov et al., 2004, 2007). As expected, the unfolding pattern of NpSRII (Figures 1D and 1E) is similar to those observed of other archaeal rhodopsins, and different to that of bovine rhodospin. In bovine rhodopsin, the tendency of individual structural segments to unfold together in cooperative events is much more pronounced (Sapra et al., 2006b). In addition, the interactions detected by SMFS and mapped onto rhodopsin show less correlation to the secondary structures. Differences in the unfolding behavior may indicate that these proteins are nonhomologous (Sharma et al., 2006). However, the similarity of unfolding patterns of different archeal rhodopsins indicate that they are not only structurally and functionally similar (Sharma et al., 2006) but also that their intramolecular interactions have been conserved.

Applying a New Procedure to Analyze F-D Spectra

In previous work, we have introduced the superimposition of F-D curves to highlight common features (Kedrov et al., 2007; Oesterhelt et al., 2000). However, superimpositions do not allow force and probability to be determined. In addition, distances in F-D curves are given in metric units, making it difficult to correlate force peaks with portions of the stretched peptide. To directly correlate the force peaks to the stretched polypeptide lengths, we introduce a new procedure to analyze the F-D spectra. First, we fit every force peak detected in a single F-D curve using the WLC model (Muller et al., 2002). From each fit we obtain the length of the stretched polypeptide and the rupture force of each peak. Analyzing every F-D curve provides the probability and the average force at which a certain force peak is detected. Replacing the WLC fitted pulling distance with the polypeptide length allows mapping interaction force and probability onto the unfolded polypeptide (Figures 2 and 3). As noted previously, the average force includes only data from detected force peaks. To be able to determine the true average strength of interactions established within all NpSRII molecules, the average force had to be normalized. Therefore, we multiplied the peak probability and average force for every stretched length of the polypeptide (Figure 4A). This normalized average force presents the interaction strength that can be expected in a randomly picked NpSRII molecule, or in other words, the average interaction strength in NpSRII.

Interactions Occurring upon Transducer Binding Are Localized

The histograms shown in Figures 2 and 3 allow a coarse correlation of interactions measured for the stretched polypeptide

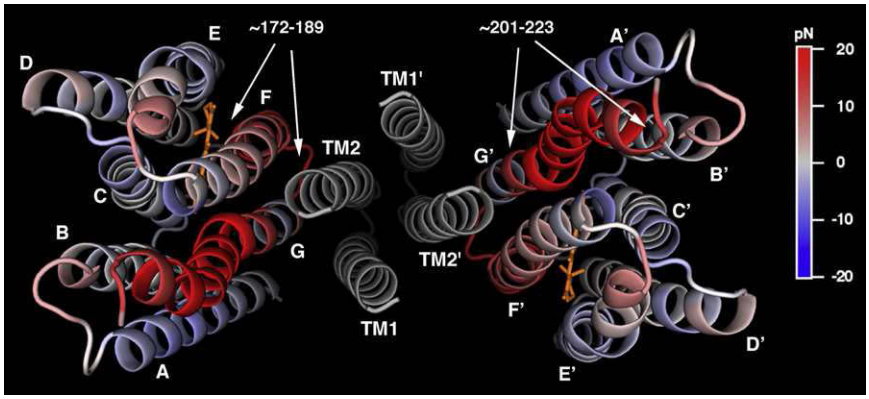

Figure 5. Structural Map of Interactions That Change upon NpHtrII$_{114}$ to NpSRII Binding

The X-ray structure of the NpSRII + NpHtrII$_{114}$ heterodimeric complex (Gordeliy et al., 2002) was color scaled to visualize changes in normalized average interaction forces. To visualize subtle changes in the interaction force, the color scale ranges from −20 to 20 pN (note that interaction forces detected at helix G can scale up to ~80 pN; see Figure 4B). Positive changes (red) indicate interactions strengths increasing upon NpHtrII$_{114}$ binding. Transmembrane α helices of NpSRII are named from A to G. Transmembrane α helices TM1 and TM2 belong to the truncated transducer (NpHtrII$_{114}$).

lengths to positions at which these interactions occur in the NpSRII polypeptide. After correcting the location of the interactions that are within the membrane bilayer or on the side of the membrane opposite to the pulling AFM tip (see Experimental Procedures), the peaks are more accurately mapped onto the NpSRII polypeptide (Figure 4). The map calculated by finding the difference between the normalized average interactions of NpSRII alone and of NpSRII in complex with the transducer (Figure 4A) locates the polypeptide regions at which intramolecular interactions changed upon transducer binding (Figure 4B). The predominant changes were at WLC fitted polypeptide lengths of ~34 aa and ~45 aa (Figure 4B, lower x axis of histogram), which correlate to amino acid positions ~211 and ~174 as counted from the N-terminal end (Figure 4B, upper x axis of histogram), respectively. These maxima locate to structural regions of transmembrane α helices F and G. Whereas transducer binding enhances the normalized interaction strength at transmembrane α helix G by ~80 pN, that established at α helix F is enhanced by only ~18 pN.

The force histograms (Figures 2 and 4A) show that the peaks at ~34 aa and ~45 aa were detected in NpSRII independent of the transducer binding. In the case of bacteriorhodopsin (Muller et al., 2002) and halorhodopsin (Cisneros et al., 2005), SMFS detects interactions at the same positions. Thus, interactions and locations appear to be conserved among all three archaeal rhodopsins. Upon transducer binding, both interactions are strengthened. This leads to several conclusions. First, transducer binding specifically influences certain interactions within the NpSRII molecule. Two transmembrane α helices, F and G, are affected, whereas the other five α helices show no changes in their interaction strengths. Second, the transducer binding does not alter the NpSRII molecule enough to establish interactions at new positions. Third, the magnitude of changes to the interactions introduced upon transducer binding at helices F and G scale differently (Figure 4). The strengthening at α helix G appears to be more than four times stronger then at α helix F, suggesting a tighter interaction with the transducer.

NpSRII Interactions in the Vicinity of Transducer Binding Are Strengthened

To visualize the location of interaction differences we mapped these onto the 3D structure of the NpSRII + NpHtrII complex (Figure 5). In good agreement, the regions most affected—α helices G and F—form the NpHtrII binding site (Gordeliy et al., 2002). Alpha helices F and G also shield the remaining helices, A–E, from direct interactions with the transducer. This may explain why we did not detect any changes to interactions in these structures, neither in probability (Figure 2) nor in force (Figure 3). This finding indicates the absence of long-range interactions (Sapra et al., 2008) introduced by the transducer and bridging to structures different from α helices F and G. Thus, we assume that α helices F and G interact with the transducer independently of the other NpSRII structural regions. This is consistent with the receptor structure being almost identical with and without transducer (Luecke et al., 2001; Gordeliy et al., 2002).

It may be argued that the structure of NpSRII relaxes after the first α helices have been unfolded by SMFS. Such a relaxation would disfavor detecting changes to the α helices remaining folded in the membrane. Though membrane proteins typically fold into a membrane bilayer in seconds, SMFS, as applied here, forces transmembrane helices to unfold in 10–20 microseconds. Although quick, the microsecond time range may allow small structural rearrangements within the folded part of the protein. Thus, it may be that SMFS does not probe the native structures within a membrane protein. Molecular dynamics (MD) simulations investigating the SMFS-induced unfolding process of bacteriorhodopsin indicate that membrane protein structures remain unchanged during the mechanical unfolding process (Cieplak et al., 2006; Seeber et al., 2006). However, these MD simulations were done at much faster pulling speed than experimentally used (Kedrov et al., 2007). Nevertheless, MD simulations and experiments suggest that unpulled structures of an unfolding membrane protein remain largely unchanged. Findings in accordance with this observation are provided by experiments on the H^+/Na^+ antiporter NhaA. While unfolding NhaA by SMFS, it was possible to observe the binding of a ligand to a transmembrane α helix residing in the middle of the structure (Kedrov et al., 2005). Furthermore, from the F-D data it was possible to distinguish whether a ligand or an inhibitor was bound to the antiporter (Kedrov et al., 2006, 2008). Independent of small rearrangements to structural elements that may occur while unfolding the protein, SMFS allows comparative measurements. Here we compared the interactions established in free NpSRII molecules with those in NpSRII bound to NpHtrII$_{114}$ and determined where and to which extent transducer binding induced changes to NpSRII. To what extent our comparative experiments reflect the absolute interaction strengths established within native proteins needs to be shown.

Binding of NpHtrII to NpSRII Helices F and G May Have Possible Functional Consequences

NpSRII function as a light-driven proton pump (Schmies et al., 2000, is suppressed by the binding of the transducer NpHtrII (Schmies et al., 2001). Proton transport has been thoroughly studied in the structurally and functionally related bacteriorhodopsin (Haupts et al., 1999; Oesterhelt and Stoeckenius, 1973; Subramaniam and Henderson, 2000). A key event is the opening of the proton channel on the cytoplasmic side of the membrane, which is accompanied by tilting transmembrane α helix F (Koch et al., 1991; Moukhametzianov et al., 2006; Yoshida et al., 2004). This conformational change provides the basis for reprotonation of the Schiff base. Binding of NpHtrII to NpSRII is aided by hydrogen bonds between Thr189 and Tyr199 of α helix G with transmembrane α helix TM2 of the transducer (Klare et al., 2004). Signal transduction is controlled by the receptor, in particular by Thr204 (α helix G) and its hydrogen-bonded partner Tyr174 (α helix F). These two residues are essential for phototaxis (Sudo et al., 2006), and their introduction into bacteriorhodopsin converts the proton pump to, like SRII, activate HtrII (Sudo and Spudich, 2006). This demonstrates the key role of residues and hosting α helices F and G.

In recent years, several biophysical techniques have been applied to investigate possible structural rearrangements occurring at the interface between receptor and transducer. The interactions between NpSRII and NpHtrII appear to couple the light-induced conformational change of α helix F to signal transduction (Wegener et al., 2000; Klare et al., 2004). FTIR, FRET, molecular dynamics simulations, and EPR spectroscopy yielded partly contradictory results on light-induced structural rearrangements of transmembrane α helices F and G of the receptor and α helix TM2 of the transducer (Bordignon et al., 2007). In absence of the transducer, α helix F bends outward, allowing uptake and pumping of the proton from the cytoplasmic side of the membrane. In the presence of the transducer, this proton pumping mechanism is impaired. FTIR measurements by the Spudich group suggested that the reconstituted NpSRII + $NpHtrII_{147}$ fusion complex undergoes conformational changes consistent with an outward tilting of α helix F (Bergo et al., 2003). In apparent contrast, FTIR measurements (Kamada et al., 2006) suggested that the opening of the cytoplasmic cleft required for the proton uptake does not occur in phosphatidylcholine reconstituted NpSRII in the presence of the transducer. However, EPR measurements of the NpSRII + $NpHtrII_{114}$ complex reconstituted into purple membrane lipids, such as investigated in our study, suggest that during receptor activation, α helix F undergoes conformational changes both in the presence and absence of the transducer (Bordignon et al., 2007; Wegener et al., 2000). Light-induced isomerization of the retinal is proposed to induce specific conformational changes to the receptor that triggers an outward motion of transmembrane α helix F. In this motion, α helix F slides along α helix G, whose structure remains unchanged, and induces a clockwise rotary motion of transmembrane α helix TM2 to activate the transducer. The evidence of a conformational change is contradicted by the X-ray structures of the inactivated and illuminated NpSRII + NpHtrII complex (Moukhametzianov et al., 2006). Here, the light-induced isomerization of the retinal does not cause conformational changes in α helix F. This finding is surprising because the transducer appears to be structurally altered in α helix TM2. It is assumed that the interactions with the transducer inhibit conformational changes of α helix F. However, loop EF of the receptor in the 3D crystal forms contacts with other proteins. Because the flexibility of the EF loop is important for the outward tilting of helix F (Koch et al., 1991; Subramaniam and Henderson, 2000), the crystal-specific contact of the EF loop may inhibit this motion.

Our SMFS measurements reveal that the binding of $NpHtrII_{114}$ to NpSRII significantly increases the interactions established at transmembrane α helices F and G (Figure 4B). Compared with transmembrane α helix F, α helix G exhibited an almost 4-fold higher increase of interactions strength. In α helix G these interactions induced by the transducer are distributed over nearly the entire helix, whereas α helix F is stabilized only at its extracellular end (Figure 5). Previously, in the case of the H^+/Na^+ antiporter NhaA, we showed that inhibitor binding enhances the interactions at transmembrane α helix IX and reduces its structural flexibility (Kedrov et al., 2006, 2008). Analogous to this finding, we speculate that the strengthening of the existing interactions at transmembrane α helix G of NpSRII further stabilizes this helix and reduces its flexibility. Similarly, transducer binding enhances the stability and thus may reduce the flexibility at the extracellular end of α helix F. Most importantly, both structural domains exhibiting significantly enhanced stability and reduced flexibility must act differently in NpSRII complexed with the transducer. The enhanced stability and reduced flexibility of helix G leads to the assumption that this structure will remain unchanged upon light-induced activation of the NpSRII + $NpHtrII_{114}$ complex. In contrast, the transducer binding "pins" α helix F only at its extracellular end. It may be that this pinning of the structure guides the cytoplasmic end of the helix to enable efficient signal transduction. Such a model is supposed by EPR measurements (Bordignon et al., 2007; Wegener et al., 2001) in which light activation of the receptor induces an outward motion of α helix F along G to activate the transducer. However, in our SMFS measurements we can only detect and locate interactions in NpSRII. Thus, interpretations of how such interactions may guide conformational changes of a receptor remain speculative until further insights are obtained. Our findings show how transducer binding changes the interactions and coupling within the receptor in a way that proton pumping is inhibited (Spudich, 1998) and signal transduction enabled.

Conclusion

Using SMFS, we detected interactions within NpSRII without and with its transducer bound. To reveal the differences between transducer bound and unbound states we introduced a simple way to analyze the F-D spectra. The analysis revealed the strength and structural location of intramolecular interactions within the average receptor. Binding of the transducer to NpSRII enhanced intramolecular interactions that already existed at transmembrane α helices G and F. We suggest that the specific binding of the transducer and its ability to strengthen key interactions at α helices F and G of NpSRII "prime" the receptor for signaling rather than ion pumping. This binding, with its specific interactions, may reflect a mechanism by which the receptor-transducer interaction could have evolved without compromising the photocycle of microbial rhodopsins.

EXPERIMENTAL PROCEDURES

Sample Preparation

NpSRII and NpHtrII$_{114}$ from *N. pharaonis* were overexpressed as His-tagged proteins in *Escherichia coli* and purified by affinity chromatography using a Ni-NTA agarose column (QIAGEN, Hilden, Germany). NpSRII was then reconstituted into purple membrane lipids with a 1:35 (w/w) protein-to-lipid ratio (Hohenfeld et al., 1999). NpSRII + NpHtrII$_{114}$ complexes were prepared by mixing NpSRII and NpHtrII$_{114}$ at a ratio of 1:1 followed by reconstitution into lipids (Wegener et al., 2001).

SMFS

SMFS on NpSRII and NpSRII + NpHtrII$_{114}$ complexes was performed as described (Muller et al., 2002; Oesterhelt et al., 2000). Membrane patches containing the reconstituted NpSRII were adsorbed to the mica support and visualized by AFM. After imaging, the AFM was switched to the SMFS mode. The AFM tip was then pushed onto the protein membrane until a terminal end of the protein adsorbed to the tip by unspecific interactions (Janovjak et al., 2003; Oesterhelt et al., 2000). The AFM tip was then retracted from the membrane surface at a velocity of ~300 nm/s. Force-versus-distance (F-D) curves were obtained by recording the cantilever deflection over the separation distance. Si_3N_4 cantilevers (model NP-S, nominal spring constant ~0.06 N/m and resonance frequency ~18 kHz; Veeco Instruments, Santa Barbara, CA) were used for imaging and force spectroscopy. All cantilevers showed a spring constant of ~0.07 ± 0.01 N/m, which was determined using the equipartition theorem (Butt et al., 1995).

As in previous studies, the length of F-D spectra was used to discard F-D curves that resulted from the attachment of the AFM tip with regions of the polypeptide other than the terminal ends (Cisneros et al., 2005; Muller et al., 2002). The N-terminal end of NpSRII forms a 1 or 2 aa-long end of α helix A, which is mainly embedded in the membrane (Luecke et al., 2001). Because of this limited exposure, the probability of the N-terminal end attaching to the AFM tip was assumed to be very low. The C-terminal end is longer (~23 aa) and, thus, has a much higher probability of attaching to the AFM tip. We assume that upon mechanically pulling from a terminal end all transmembrane α helices unfold sequentially from this end while the tip is separated from the membrane. The maximum length of the stretched polypeptide, indicated by the last force peak, measures the stability of the last α helix embedded in the membrane. Thus the maximum length of the stretched polypeptide can be estimated by the polypeptide stretch from the terminal end pulled to this last α helix (Kedrov et al., 2004; Kessler and Gaub, 2006). This simple model predicts different maximum lengths of F-D curves obtained for pulling at the N-terminal or C-terminal ends of NpSRII. Mechanical unfolding of the first six transmembrane α helices results in a stretched polypeptide segment of ~60 nm (~200 aa) length when pulling from the N-terminal end, and lengths ranging between 60 and 65 nm (202–219 aa) when pulled from the C-terminal end. Therefore, F-D curves obtained from pulling at either terminal end could be separated from each other. Thus, to analyze only F-D curves obtained pulling single NpSRII molecules from the C-terminal end, we selected curves exhibiting lengths ≥60 nm.

In contrast to this unambiguous criterion, the classification and analysis of shorter F-D curves was not attempted. For example, F-D curves of lengths between 50 and 60 nm represent NpSRII pulled from either the C- or the N-terminal end. Even shorter F-D curves may have resulted from picking the NpSRII molecule from one of its polypeptide loops. These F-D curves cannot be used because pulling at different loops results in F-D curves of similar lengths. In addition, protein and AFM tip frequently unbind during mechanically pulling, resulting in abortive short F-D curves. These considerations are further complicated by the presence of the transducer, which may be unfolded from either terminal end, resulting in F-D curves of similar lengths as expected when unfolding NpSRII from either its CD or EF loops. Therefore, we focused our data analysis on F-D curves that resulted from full unfolding and stretching of NpSRII by pulling at the C-terminal end.

After selecting a sufficiently long F-D curve (≥60 nm), each force peak was fitted using the wormlike chain (WLC) model (Bustamante et al., 1994). The contour length (L) of the stretched polypeptide was obtained from the WLC fit assuming a persistence length (l_p) of 0.4 nm (Oesterhelt et al., 2000). Equally, for each peak the rupture force was measured. To locate the interactions corresponding to force peaks onto the NpSRII structure (1H2S; Gordeliy et al., 2002), the contour length at which this peak occurred was subtracted from the C-terminal end.

When pulling the protein from the C-terminal end, the interaction anchoring the stretched polypeptide segment was sometimes not located at the cytoplasmic end of an α helix, but at the opposite N-terminal surface. In this case, the effective length of the stretched polypeptide was longer and the lipid membrane thickness (~4 nm) had to be considered. In this case, we added 11 aa (11 × 0.36 nm ≈ 4 nm) to the number of amino acids determined by the WLC model (Muller et al., 2002). If a segment was shorter than the width of the membrane, a fraction of the membrane thickness (11 aa) proportional to the length of the apparent stretched polypeptide was added. To visualize the interactions within NpSRII that have changed upon NpHtrII binding, the histograms of the normalized interaction forces measured for NpSRII with and without the transducer NpHtrII$_{114}$ (Figure 4A) were subtracted from each other. To avoid artifacts, the resulting histogram was smoothed by an algorithm that distributed 25% of the counts of each bin to the previous and following bin. The differences of the normalized forces were then mapped onto the NpSRII structure.

ACKNOWLEDGMENTS

This work was supported by the Deutsche Forschungsgemeinschaft (DFG), the European Union (FP6), and the Free State of Saxony. We thank Annika Göppner for excellent technical help, and Georg Büldt, Tanuj Sapra, and Daniel Silva for helpful discussions.

Received: February 17, 2008
Revised: April 11, 2008
Accepted: April 11, 2008
Published: August 5, 2008

REFERENCES

Bergo, V., Spudich, E.N., Spudich, J.L., and Rothschild, K.J. (2003). Conformational changes detected in a sensory rhodopsin II-transducer complex. J. Biol. Chem. *278*, 36556–36562.

Bordignon, E., Klare, J.P., Holterhues, J., Martell, S., Krasnaberski, A., Engelhard, M., and Steinhoff, H.J. (2007). Analysis of light-induced conformational changes of *Natronomonas pharaonis* sensory rhodopsin II by time resolved electron paramagnetic resonance spectroscopy. Photochem. Photobiol. *83*, 263–272.

Bustamante, C., Marko, J.F., Siggia, E.D., and Smith, S. (1994). Entropic elasticity of lambda-phage DNA. Science *265*, 1599–1600.

Butt, H.J., Jaschke, M., and Ducker, W. (1995). Measuring surface forces in aqueous electrolyte solution with the atomic force microscope. Bioelectrochem. Bioenerg. *38*, 191–201.

Chizhov, I., Schmies, G., Seidel, R., Sydor, J.R., Luttenberg, B., and Engelhard, M. (1998). The photophobic receptor from *Natronobacterium pharaonis*: temperature and pH dependencies of the photocycle of sensory rhodopsin II. Biophys. J. *75*, 999–1009.

Cieplak, M., Filipek, S., Janovjak, H., and Krzysko, K.A. (2006). Pulling single bacteriorhodopsin out of a membrane: comparison of simulation and experiment. Biochim. Biophys. Acta *1758*, 537–544.

Cisneros, D.A., Oesterhelt, D., and Muller, D.J. (2005). Probing origins of molecular interactions stabilizing the membrane proteins halorhodopsin and bacteriorhodopsin. Structure *13*, 235–242.

Gordeliy, V.I., Labahn, J., Moukhametzianov, R., Efremov, R., Granzin, J., Schlesinger, R., Buldt, G., Savopol, T., Scheidig, A.J., Klare, J.P., et al. (2002). Molecular basis of transmembrane signalling by sensory rhodopsin II-transducer complex. Nature *419*, 484–487.

Haupts, U., Tittor, J., and Oesterhelt, D. (1999). Closing in on bacteriorhodopsin: progress in understanding the molecule. Annu. Rev. Biophys. Biomol. Struct. *28*, 367–399.

Hohenfeld, I.P., Wegener, A.A., and Engelhard, M. (1999). Purification of histidine tagged bacteriorhodopsin, pharaonis halorhodopsin and pharaonis

sensory rhodopsin II functionally expressed in *Escherichia coli*. FEBS Lett. *442*, 198–202.

Janovjak, H., Kessler, M., Oesterhelt, D., Gaub, H., and Muller, D.J. (2003). Unfolding pathways of native bacteriorhodopsin depend on temperature. EMBO J. *22*, 5220–5229.

Janovjak, H., Kedrov, A., Cisneros, D.A., Sapra, K.T., Struckmeier, J., and Muller, D.J. (2006). Imaging and detecting molecular interactions of single transmembrane proteins. Neurobiol. Aging *27*, 546–561.

Kamada, K., Furutani, Y., Sudo, Y., Kamo, N., and Kandori, H. (2006). Temperature-dependent interactions between photoactivated pharaonis phoborhodopsin and its transducer. Biochemistry *45*, 4859–4866.

Kedrov, A., Ziegler, C., Janovjak, H., Kuhlbrandt, W., and Muller, D.J. (2004). Controlled unfolding and refolding of a single sodium-proton antiporter using atomic force microscopy. J. Mol. Biol. *340*, 1143–1152.

Kedrov, A., Krieg, M., Ziegler, C., Kuhlbrandt, W., and Muller, D.J. (2005). Locating ligand binding and activation of a single antiporter. EMBO Rep. *6*, 668–674.

Kedrov, A., Ziegler, C., and Muller, D.J. (2006). Differentiating ligand and inhibitor interactions of a single antiporter. J. Mol. Biol. *362*, 925–932.

Kedrov, A., Janovjak, H., Sapra, K.T., and Muller, D.J. (2007). Deciphering molecular interactions of native membrane proteins by single-molecule force spectroscopy. Annu. Rev. Biophys. Biomol. Struct. *36*, 233–260.

Kedrov, A., Appel, M., Baumann, H., Ziegler, C., and Muller, D.J. (2008). Examining the dynamic energy landscape of an antiporter upon inhibitor binding. J. Mol. Biol. *375*, 1258–1266.

Kessler, M., and Gaub, H.E. (2006). Unfolding barriers in bacteriorhodopsin probed from the cytoplasmic and the extracellular side by AFM. Structure *14*, 521–527.

Klare, J.P., Gordeliy, V.I., Labahn, J., Buldt, G., Steinhoff, H.J., and Engelhard, M. (2004). The archaeal sensory rhodopsin II/transducer complex: a model for transmembrane signal transfer. FEBS Lett. *564*, 219–224.

Klare, J.P., Chizhov, I., and Engelhard, M. (2008). Microbial rhodopsins: scaffolds for ion pumps, channels, and sensors. Results Probl. Cell Differ. *45*, 73–122.

Klyszejko, A.L., Shastri, S., Mari, S.A., Grubmuller, H., Muller, D.J., and Glaubitz, C. (2008). Folding and assembly of proteorhodopsin. J. Mol. Biol. *376*, 35–41.

Koch, M.H.J., Dencher, N.A., Oesterhelt, D., Plöhn, H.-J., Rapp, G., and Büldt, G. (1991). Time-resolved X-ray diffraction study of structural changes associated with the photocycle of bacteriorhodopsin. EMBO J. *10*, 521–526.

Luecke, H., Schobert, B., Lanyi, J.K., Spudich, E.N., and Spudich, J.L. (2001). Crystal structure of sensory rhodopsin II at 2.4 Angstroms: insights into color tuning and transducer interaction. Science *293*, 1499–1503.

Moukhametzianov, R., Klare, J.P., Efremov, R., Baeken, C., Goppner, A., Labahn, J., Engelhard, M., Buldt, G., and Gordeliy, V.I. (2006). Development of the signal in sensory rhodopsin and its transfer to the cognate transducer. Nature *440*, 115–119.

Muller, D.J., Amrein, M., and Engel, A. (1997). Adsorption of biological molecules to a solid support for scanning probe microscopy. J. Struct. Biol. *119*, 172–188.

Muller, D.J., Kessler, M., Oesterhelt, F., Moller, C., Oesterhelt, D., and Gaub, H. (2002). Stability of bacteriorhodopsin α-helices and loops analyzed by single-molecule force spectroscopy. Biophys. J. *83*, 3578–3588.

Oesterhelt, D., and Stoeckenius, W. (1973). Functions of a new photoreceptor membrane. Proc. Natl. Acad. Sci. U.S.A. *70*, 2853–2857.

Oesterhelt, F., Oesterhelt, D., Pfeiffer, M., Engel, A., Gaub, H.E., and Muller, D.J. (2000). Unfolding pathways of individual bacteriorhodopsins. Science *288*, 143–146.

Park, P.S., Sapra, K.T., Kolinski, M., Filipek, S., Palczewski, K., and Muller, D.J. (2007). Stabilizing effect of Zn^{2+} in native bovine rhodopsin. J. Biol. Chem. *282*, 11377–11385.

Sapra, K.T., Besir, H., Oesterhelt, D., and Muller, D.J. (2006a). Characterizing molecular interactions in different bacteriorhodopsin assemblies by single-molecule force spectroscopy. J. Mol. Biol. *355*, 640–650.

Sapra, K.T., Park, P.S., Filipek, S., Engel, A., Muller, D.J., and Palczewski, K. (2006b). Detecting molecular interactions that stabilize native bovine rhodopsin. J. Mol. Biol. *358*, 255–269.

Sapra, K.T., Balasubramanian, G.P., Labudde, D., Bowie, J.U., and Muller, D.J. (2008). Point mutations in membrane proteins reshape energy landscape and populate different unfolding pathways. J. Mol. Biol. *376*, 1076–1090.

Schmies, G., Luttenberg, B., Chizhov, I., Engelhard, M., Becker, A., and Bamberg, E. (2000). Sensory rhodopsin II from the haloalkaliphilic *Natronobacterium pharaonis*: light-activated proton transfer reactions. Biophys. J. *78*, 967–976.

Schmies, G., Engelhard, M., Wood, P.G., Nagel, G., and Bamberg, E. (2001). Electrophysiological characterization of specific interactions between bacterial sensory rhodopsins and their transducers. Proc. Natl. Acad. Sci. U.S.A. *98*, 1555–1559.

Seeber, M., Fanelli, F., Paci, E., and Caflisch, A. (2006). Sequential unfolding of individual helices of bacterioopsin observed in molecular dynamics simulations of extraction from the purple membrane. Biophys. J. *91*, 3276–3284.

Sharma, A.K., Spudich, J.L., and Doolittle, W.F. (2006). Microbial rhodopsins: functional versatility and genetic mobility. Trends Microbiol. *14*, 463–469.

Spudich, J.L. (1998). Variations on a molecular switch: transport and sensory signalling by archaeal rhodopsins. Mol. Microbiol. *28*, 1051–1058.

Spudich, J.L. (2006). The multitalented microbial sensory rhodopsins. Trends Microbiol. *14*, 480–487.

Spudich, J.L., and Bogomolni, R.A. (1984). Mechanism of colour discrimination by a bacterial sensory rhodopsin. Nature *312*, 509–513.

Subramaniam, S., and Henderson, R. (2000). Molecular mechanism of vectorial proton translocation by bacteriorhodopsin. Nature *406*, 653–657.

Sudo, Y., and Spudich, J.L. (2006). Three strategically placed hydrogen-bonding residues convert a proton pump into a sensory receptor. Proc. Natl. Acad. Sci. U.S.A. *103*, 16129–16134.

Sudo, Y., Furutani, Y., Kandori, H., and Spudich, J.L. (2006). Functional importance of the interhelical hydrogen bond between Thr204 and Tyr174 of sensory rhodopsin II and its alteration during the signaling process. J. Biol. Chem. *281*, 34239–34245.

Wegener, A.A., Chizhov, I., Engelhard, M., and Steinhoff, H.J. (2000). Time-resolved detection of transient movement of helix F in spin-labelled *pharaonis* sensory rhodopsin II. J. Mol. Biol. *301*, 881–891.

Wegener, A.A., Klare, J.P., Engelhard, M., and Steinhoff, H.J. (2001). Structural insights into the early steps of receptor-transducer signal transfer in archaeal phototaxis. EMBO J. *20*, 5312–5319.

Yan, B., Takahashi, T., Johnson, R., and Spudich, J.L. (1991). Identification of signaling states of a sensory receptor by modulation of lifetimes of stimulus-induced conformations: the case of sensory rhodopsin II. Biochemistry *30*, 10686–10692.

Yoshida, H., Sudo, Y., Shimono, K., Iwamoto, M., and Kamo, N. (2004). Transient movement of helix F revealed by photo-induced inactivation by reaction of a bulky SH-reagent to cysteine-introduced pharaonis phoborhodopsin (sensory rhodopsin II). Photochem. Photobiol. Sci. *3*, 537–542.